In situ cosmogenic ^{10}Be in pyroxene with an application to surface exposure dating

Julia Anne Collins

A thesis submitted to Victoria University of Wellington

in partial fulfilment of requirements for the degree of

Master of Science in Geology

School of Geography, Environment, and Earth Sciences

Victoria University of Wellington

July 2015

Abstract

Cosmogenic nuclides are an important tool in quantifying many Earth-surface processes. Beryllium-10 (^{10}Be) is commonly extracted out of the mineral quartz; however many landscapes lack quartz bearing rocks. In order to establish a new chronometer based on ^{10}Be in pyroxene for use in New Zealand and Antarctica, it is necessary to verify cleaning protocols and determine a local production rate. In this study, I have tested and modified an existing pyroxene decontamination procedure in order to further develop the use of ^{10}Be in pyroxene as a chronometer. This method successfully removes the meteoric component of ^{10}Be in pyroxene, allowing only the concentration of *in situ* produced ^{10}Be to be measured. Additionally, production rates for ^{10}Be in pyroxene have been determined empirically for New Zealand using cross-calibration with measured ^{3}He concentrations and an independent radiocarbon age of the Murimotu debris avalanche in the central North Island, New Zealand of 10.6 ± 1.1 ka. Theoretical ^{10}Be pyroxene production rates were also determined, based on the composition of the Murimotu pyroxene. The best estimate for the ^{10}Be pyroxene production rate is 3.4 ± 0.8 atoms g^{-1} yr^{-1} at sea-level high latitude, which was determined via cross-calibration with the radiocarbon age for the deposit. This work shows that production rates for ^{10}Be in pyroxene are both empirically and theoretically 8-27% lower than in quartz. The ^{3}He/^{10}Be ratio in the Murimotu pyroxene is 34.5 ± 9.9; this is indistinguishable from global ^{3}He-pyroxene/^{10}Be-quartz production ratios.

In a case study surface exposure ages were determined for bedrock samples and cobble erratics collected in a vertical transect on Mount Gran, Antarctica, by applying

the aforementioned ^{10}Be pyroxene decontamination procedure and radiocarbon derived production rates. A chronology for ice surface lowering was obtained for the adjacent Mackay Glacier, indicating the ice surface lowered approximately 60 m during a relatively rapid episode of thinning which occurred between ~13.5 ka and 11 ka.

This thesis presents a successful test of decontamination procedures, new production rates, and an example application, showing the promise of ^{10}Be in pyroxene as a chronometer. The development of ^{10}Be in pyroxene allows environments without quartz-bearing rocks to be dated using this widely used nuclide. The pairing of ^{10}Be with ^{3}He in pyroxene would allow complex exposure histories to be determined, expanding the application.

Acknowledgements

Firstly, I would like to say a huge thank you to my main supervisor Kevin Norton. For your countless hours spent guiding me in the cosmo lab, helping me solve (the many) problems, and reading over my thesis (so many times!), I am extremely grateful. Your enthusiasm and passion always kept me motivated and excited about the project. Secondly, thank you to my secondary supervisor Andrew Mackintosh. Your valuable insight and constructive feedback has been greatly appreciated. Also, a huge thanks to Richard Jones and Shaun Eaves for your unique knowledge on the topics and willingness to help. A number of people around the building were also important in helping with lab work and analysis; so thank you to Jane, Sabrina, and the Geochem Girls for your help in learning the ropes of the ultra-clean lab. Additionally, thanks to Steve Tims at ANU, for measuring my samples.

Thank you to everyone around the Cotton building that has either helped me, or just been around for a chat. I couldn't have asked for better colleagues and friends. I have thoroughly enjoyed my time at Vic, and it's all thanks to you guys. Special mention to the many occupants and frequent visitors of CO422; your distractions, yoga breaks, chocolate, and occasional beverages were always welcome, particularly during write up. Lastly to my family and friends, thank you for putting up with my love of rocks, and for your constant support. You always kept me motivated.

Table of contents

Abstract i

Acknowledgements iii

Table of contents v

List of Figures ix

List of Tables xi

Chapter One: Introduction 1

1.1 Principals of Cosmogenic Nuclides 2

1.1.1 Cosmic rays 2

1.1.2 Cosmogenic Nuclides 8

1.1.3 Beryllium-10 10

1.1.4 ^{10}Be in pyroxene as a chronometer 13

1.1.5 Production rates 15

1.1.6 Production rate calibration sites in New Zealand 17

1.1.7 Application of ^{10}Be to Earth surface processes 19

1.1.8 Application to glacial environments 20

1.1.9 Application of surface exposure dating in Antarctica 24

1.1.10 Thinning rates of Mackay Glacier, Antarctica 26

1.2 Antarctic ice sheet thinning since the LGM 27

1.2.1 Volume of Antarctic ice during the LGM and subsequent ice loss 28

1.2.2 Timing of advance and retreat 29

1.2.3 Glacial thinning 30

1.3 Research Question 31

Chapter Two: Methods 31

2.1 Sample localities 31
2.1.1 Mount Ruapehu 31
2.1.1.1 Location 31
2.1.1.2 Lithology 32
2.1.1.3 Reason for site selections 33
2.1.2 Mount Gran 37
2.1.2.1 Location 37
2.1.2.2 Lithology 41
2.1.2.3 Reason for site selection 47
2.2 Sample Collection 47
2.3 Sample preparation 48
2.4 Chemistry 50
2.4.1 Method development and leach verification 50
2.4.1.1 Hydroxylammonium-chloride leach 50
2.4.1.2 Hydrochloric leach 51
2.4.1.3 Dissolution in hydrofluoric acid 51
2.4.1.4 Decontamination method verification 52
2.4.2 Column calibration and precipitation 55
2.4.2.1 BeF_2 leach 55
2.4.2.2 Cation chemistry – Fe columns 55
2.4.2.3 Precipitation test 56
2.4.2.4 Column calibration experiments 59
2.4.2.5 Cation chemistry – Be columns 61
2.4.2.6 Be precipitation 62
2.4.2.7 Accelerator Mass Spectrometer 62
Chapter Three: Results 63

3.1 ^{10}Be measurement and concentrations 63

3.2 Production rate calibration 66

3.2.1 ^{10}Be production rate in pyroxene - ^{3}He cross-calibration 67

3.2.2 ^{3}He/^{10}Be ratios 71

3.2.3 ^{10}Be production rate in pyroxene - radiocarbon cross-calibration 74

3.2.4 Theoretical ^{10}Be production rate 76

3.2.5 P10px-radiocarbon internal consistancy test 81

3.3 Exposure ages 82

3.3.1 Mount Gran exposure ages 83

3.3.1.1 Bedrock samples 87

3.3.1.2 Cobble erratics 87

3.3.2 Mackay Glacier ice surface lowering 88

3.4 Chapter summary 92

Chapter Four: Discussion 93

4.1 Chemistry and ^{10}Be measurement 93

4.2 Production rate calibration 95

4.2.1 ^{10}Be production rate from cross-calibrations at Murimotu site 95

4.2.2 Magmatic component of ^{10}Be in island arc settings 96

4.2.3 ^{10}Be production rate from ^{3}He cross-calibration 97

4.2.4 ^{3}He/^{10}Be ratios 97

4.2.5 ^{10}Be production rate from radiocarbon cross-calibration 98

4.2.6 Theoretical ^{10}Be production rates in pyroxene 99

4.2.7 Comparison of ^{10}Be production rates in pyroxene and quartz 99

4.2.8 ^{10}Be production rate in pyroxene comparison 101

4.3 Mount Gran exposure ages 106

4.3.1 Bedrock samples 106

4.3.2 Cobble erratics 109

4.3.3 Mackay Glacier ice surface lowering 109

4.3.4 Mackay Glacier modelling scenarios 112

4.3.5 OxCal age-elevation modelling 113

4.3.6 Summary of possible scenarios for thinning record at Mount Gran 116

4.4 Chapter summary 117

Chapter Five: Conclusion 119

5.1 Decontamination procedure and separation chemistry 119

5.2 Production rate calibration 121

5.3 Mount Gran exposure ages 122

References 126

Appendix A 144

Pyroxene preparation and beryllium separation chemistry 144

List of Figures

1.1: The nuclear cascade of secondary ray particles. 3

1.2: Effect of Earth's magnetic field on incoming primary cosmic rays. 5

1.3: The variation in production rates with latitude and elevation..... 6

1.4: The attenuation length as a function of cut-off rigidity 7

1.5: ^{10}Be production rates in quartz as a function of depth below the surface..... 10

1.6: Schematic diagram showing meteoric and *in situ* ^{10}Be production 12

2.1: Mt Ruapehu sample locations 34

2.2: JC2 sample photos 34

2.3: Murimotu sample locations..... 35

2.4: Murimotu sample photos 36

2.5: Mt Gran location 37

2.6: Mt Gran sample locations 38

2.7: Mt Gran cobble erratic sample photos 40

2.8: Mt Gran bedrock sample photos 41

2.9: Mt Gran sample thin sections..... 42

2.10: Evolution of ^{10}Be concentration in leaching and dissolution steps..... 53

2.11: Precipitation of elements at pH 9 56

2.12: ^{10}Be concentration of precipitate and supernate after initial precipiation..... 58

2.13: Settling out of precipitate after initial precipitation step..... 58

2.14: Elution of elements during cation column experiments..... 60

3.1: Sample MM-12-03 sampled sections..... 70

3.2: Cross-calibrated and theoretical P10px comparison 80

3.3: JC2 leach post HF sample exposure ages 82

3.4: Mt Gran exposure age-elevation plot 86

3.5: Mackay Glacier ice surface lowering 91

4.1: Empirical and theoretical P10px comparison 103

4.2: MGW pyroxene viewed down binocular microscope 108

4.3: Modelled scenarios for ice surface lowering on Mackay Glacier 113

4.3: OxCal age-elevation modelled exposure ages for Mt Gran 115

List of Tables

Table 1.1: Summary of commonly used scaling schemes 16

Table 2.1: JC2 sample data and ^{10}Be concentrations 54

Table 3.1: ^{10}Be/^{9}Be ratios and ^{10}Be concentrations for JC2 and Murimotu samples .. 65

Table 3.2: ^{10}Be/^{9}Be ratios and ^{10}Be concentrations for Mt Gran samples 66

Table 3.3: Measured and normalised ^{10}Be and ^{3}He concentrations 72

Table 3.4: P10px from ^{3}He cross-calibration 73

Table 3.5: P10px from radiocarbon cross-calibration 75

Table 3.6: Theoretical ^{10}Be elemental production rates and Murimotu composition . 77

Table 3.7: Theoretical P10px and P10qtz from Murimotu samples 79

Table 3.8: Sample JC2 leach test exposure ages 81

Table 3.9: Mt Gran sample data and ^{10}Be concentration 84

Table 3.10: Exposure ages at Mt Gran 85

Table 3.11: Age offset between bedrock and cobbles 87

Table 3.12: Mackay Glacier ice surface lowering 90

Table 4.1: Percent reduction between P10qtz and P10qtz 100

Table 4.2: Determined P10px and commonly accepted P10qtz values 104

Table 4.3: OxCal modelled age output for Mt Gran 115

Chapter One: Introduction

Cosmogenic nuclide surface exposure dating has proven to be a useful way to date glacial deposits in order to investigate former ice extent and subsequent retreat in glaciated regions (Balco, 2011). The ability to measure cosmogenic nuclides at concentrations present in terrestrial rocks has advanced this technique in recent years (Fitfield, 2000; Tuniz & Norton, 2008). Surface exposure dating with cosmogenic nuclides is based on measuring the accumulated cosmogenic nuclide concentration in a rock or land-surface that can provide information on how long the rock has been exposed at the Earth's surface (Schaefer & Lifton, 2007). Cosmogenic nuclides are produced *in situ* in rocks by the interaction of secondary cosmic rays with specific atoms in the minerals of the rock (Gosse & Phillips, 2001). The nuclide concentration at the surface is proportional to the age of the rock and is inversely proportional to the erosion rate. These cosmogenic nuclides accumulate in the rock over time at a predictable rate, which then allows us to calculate the length of time that the rock has been exposed at the surface (Ivy-Ochs & Kober, 2007; Schaefer & Lifton, 2007).

This chapter is organised in the following manner; the principals of cosmogenic nuclides are discussed in section 1.1. Cosmogenic surface exposure dating can be used for a range of applications. One such application is dating glacial deposits and glacially eroded surfaces in order to constrain the timing and rate of glacial thinning and retreat in Antarctica, where other direct dating methods are limited. The

importance of understanding Antarctic ice sheet thinning is reviewed in section 1.2. These sections lead into my research questions, which are outlined in section 1.3.

1.1 Principals of Cosmogenic Nuclides

1.1.1 Cosmic rays

In situ terrestrial cosmogenic nuclides are produced by the interaction of secondary cosmic rays with target elements in the minerals of rocks and soils on the Earth's surface. These secondary cosmic rays are produced when primary cosmic rays hit the Earth's atmosphere, producing a cascade of secondary cosmic rays. Primary cosmic rays are highly charged particles that are constantly bombarding the Earth from all directions (Gosse & Phillips, 2001). These can be either galactic or solar cosmic rays. Solar cosmic rays are produced by the Sun and have energies from 1 to 100 MeV (Cerling & Craig, 1994). The production of cosmogenic nuclides from solar cosmic rays is minimal compared to the higher energy galactic cosmic rays, and therefore, are not considered further in this thesis. Galactic cosmic rays are produced in supernova explosions predominantly within the Milky Way Galaxy (Gosse & Phillips, 2001). They have much higher energies than solar cosmic rays, ranging from a few MeV to 10^{20} eV (Dunai, 2010). At the top of the atmosphere the cosmic rays are composed mainly of protons (~87%), alpha particles (~12%), and heavier nuclei (~1%) (Masarik & Reedy, 1995). These high energy particles interact with nuclei in the atmosphere, initiating predominantly spallation reactions. During spallation reactions, a high energy nucleon (proton or neutron) collides with a target nucleus, breaking it up and producing several lighter isotopes which continue the same

trajectory as the incoming ray, spalling with other nuclei (Gosse & Phillips, 2001). This produces a cascade of secondary cosmic rays (predominantly neutrons, muons, and other secondary particles) in the Earth's atmosphere (*figure 1.1)* (Dunai, 2010). The cosmic ray flux is greatly diminished when it reaches the Earth's surface (Cerling & Craig, 1994). Cosmogenic isotopes can be produced both in the atmosphere (meteoric) and in the lithosphere (*in situ*).

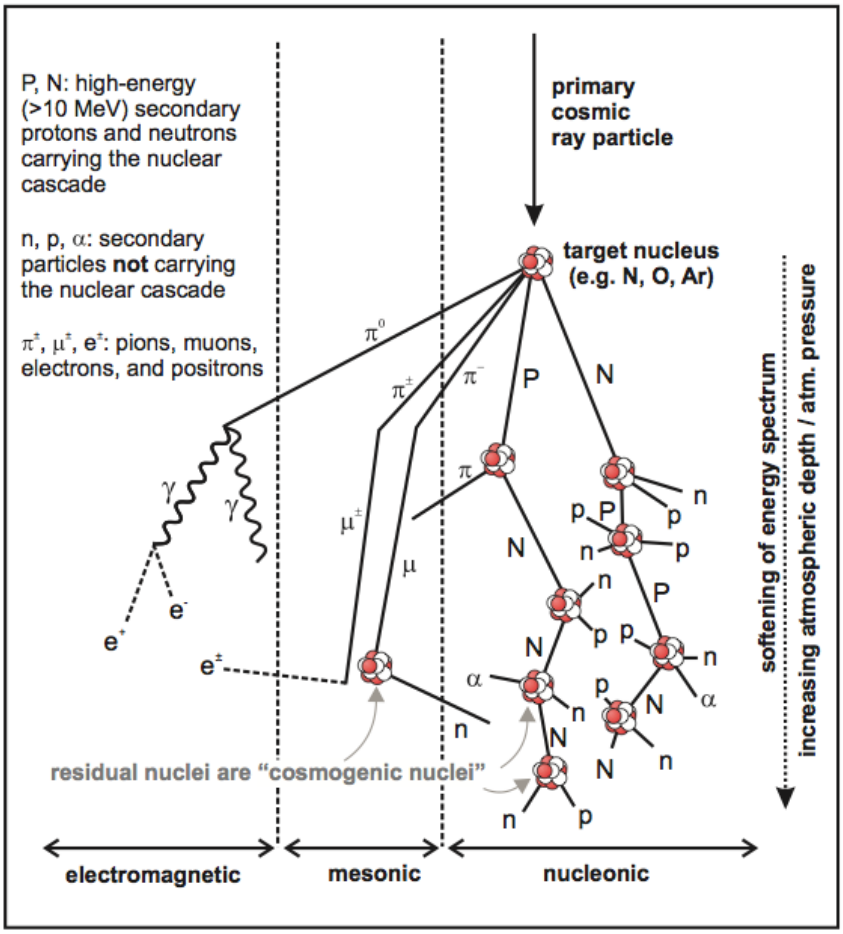

Figure 1.1: The nuclear cascade of secondary ray particles produced from an incoming primary cosmic ray in the atmosphere. The nucleonic component is responsible for most cosmogenic nuclide production. (Dunai & Lifton, 2014).

The flux of secondary cosmic rays (and consequently isotope production at the surface) depends on modulation of the primary galactic cosmic rays by the geomagnetic field, and the modulation of secondary cosmic rays by the Earth's atmosphere (Bierman, 1994). The Earth's geomagnetic field deflects incoming cosmic rays, and hence affects the flux of secondary cosmic rays at the surface. The deflection is related to the incident angle and the rigidity of the incoming cosmic ray, *r*, which is defined as:

$$r = pc/q \tag{1.1}$$

Where p is momentum, c is the velocity of light, and q is the charge of the particle (Cerling & Craig, 1994). The lowest rigidity with which a particle can penetrate the magnetic field is called the 'cut-off rigidity'. The cut-off rigidities are lower at the magnetic poles and higher at the equator. This is a result of the magnetic field lines being perpendicular to the incident angle of incoming cosmic rays at the equator, causing the greatest deflection (*figure 1.2*). Whereas, at the magnetic poles, the angle between the incoming cosmic ray and the magnetic field lines is smaller, meaning that cosmic rays with smaller cut-off rigidities are able to penetrate through to the atmosphere (Gosse & Phillips, 2001). Therefore, the lower latitudes only receive cosmic rays with higher energies, whereas the higher latitudes receive rays a wider spectrum of energies (Gosse & Phillips, 2001). Thus, the production rate of cosmogenic nuclides is higher towards the poles (*figure 1.3*).

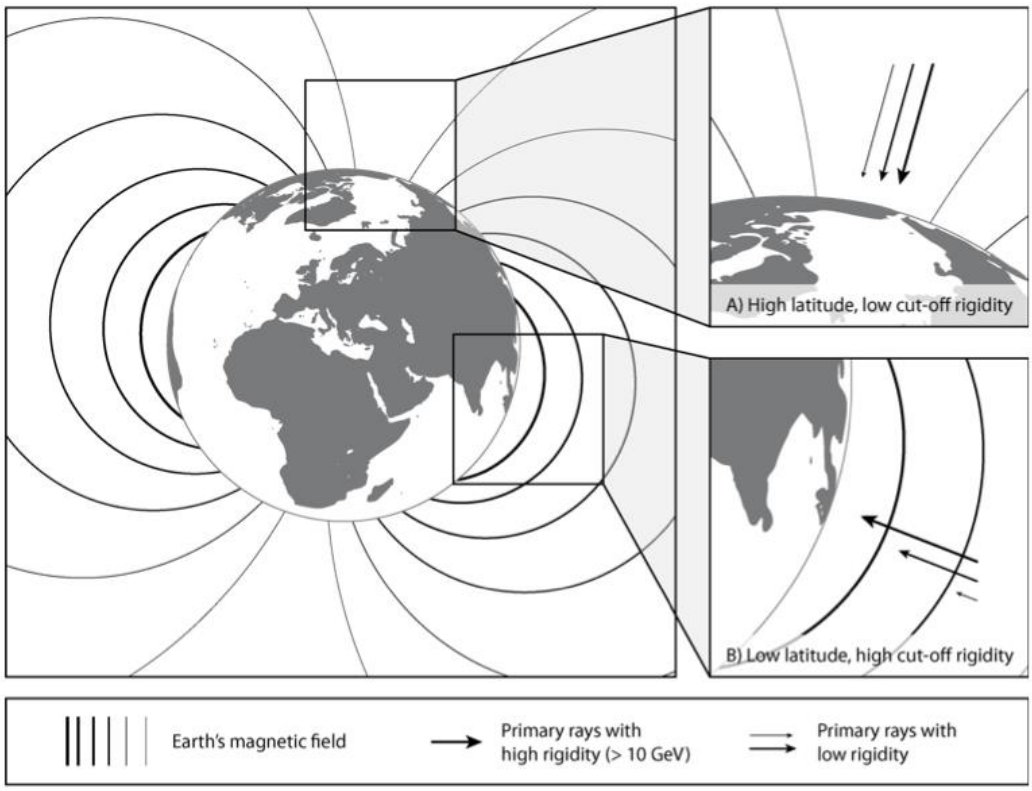

Figure 1.2: An illustration of the Earth's magnetic field and its effect on incoming primary cosmic rays. To penetrate the atmosphere the cosmic rays must exceed the cut-off rigidity which is lower towards the poles (A) and higher towards the equator (B). As primary cosmic rays with lower energies are unable to penetrate the magnetic field near the equator, the production rates of cosmogenic nuclides are lower. (Darvill, 2013).

Air pressure and shielding effects from the atmosphere cause variations in *in situ* cosmogenic production rates with altitude (Stone, 2000). As secondary cosmic rays pass though the atmosphere they are attenuated and lose energy before they reach the surface (Cerling & Craig, 1994). Therefore, the highest cosmic ray flux occurs higher in the atmosphere, resulting in larger cosmogenic nuclide production rates at higher elevations (*figure 1.3)* (Balco, *et al.*, 2008).

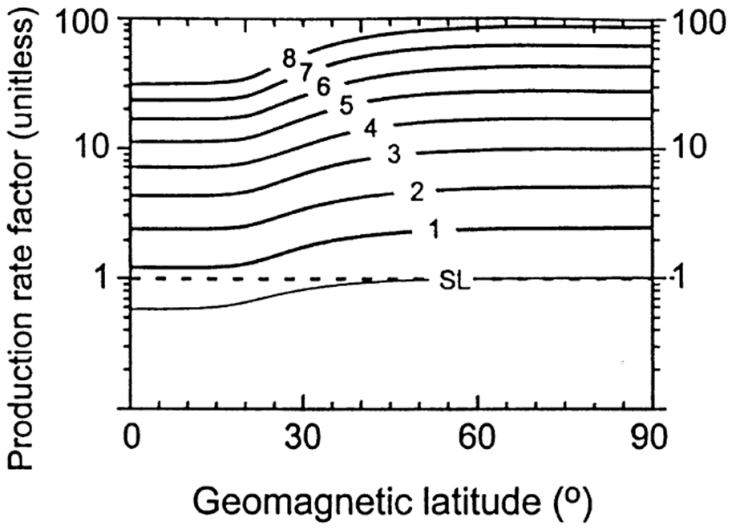

Figure 1.3: The variation in production rates with latitude and elevation. The elevation contours are 1 km. (Gosse & Phillips, 2001).

As cosmic rays are attenuated as they travel through the atmosphere, their abundance decreases exponentially with increasing atmospheric depth. The production rate can be represented by a polynomial (equation 1, Lal, 1991).

The attenuation path length is the thickness of air or rock required to attenuate the cosmic ray flux by 1/e. It varies depending on the energy of the incoming cosmic rays, thus it varies with latitude (*figure 1.4*) (Gosse & Phillips, 2001). As the cut-off rigidities are higher at the equator, the cosmic rays must have high energies to pass though, meaning that the cosmic ray flux needs to travel though more atmosphere to slow down. Therefore the attenuation path length is longer at lower latitudes (150 g/cm^2) than higher latitudes (130 g/cm^2) (Darvill, 2013).

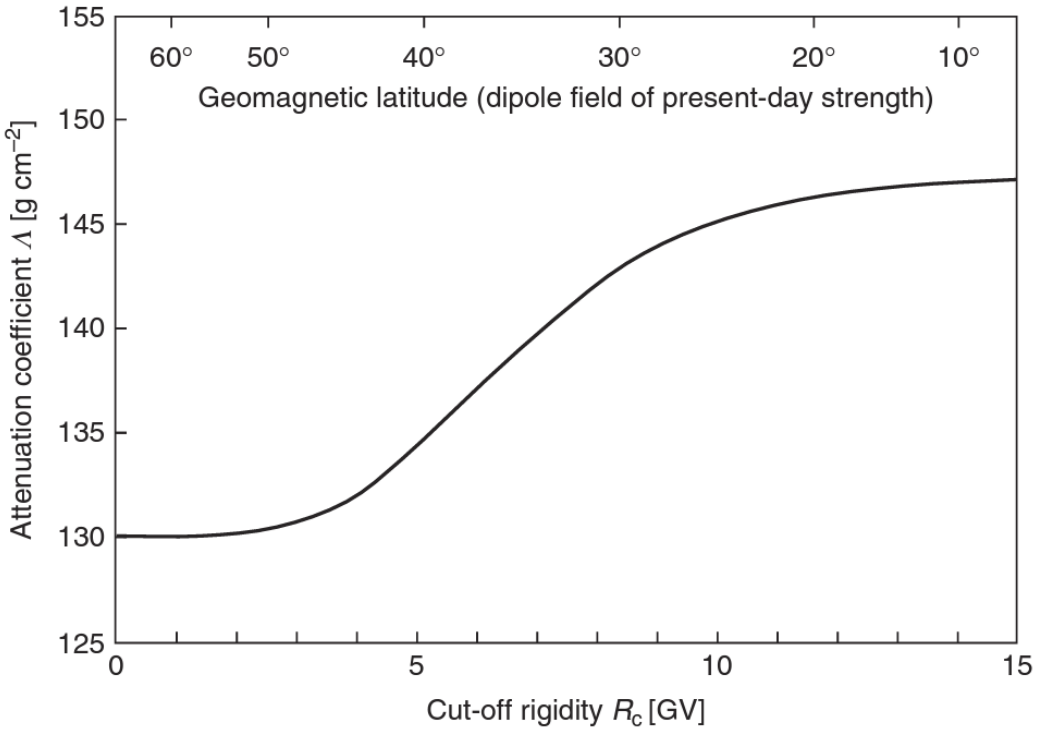

Figure 1.4: The attenuation length as a function of cut-off rigidity. Geomagnetic latitude is also shown to relate cut-off rigidities to locations on Earth. (Dunai, 2010).

Although the galactic cosmic ray flux to the Earth is constant over time, temporal variations in cosmic ray flux occur as a result of solar modulation and changes in the Earth's dipolar field over time (Lal, 1988; Masarik & Beer 1999; Masarik & Beer, 2009). The galactic cosmic ray flux is affected by the solar cycle (Webber & Higbie, 2003). During periods of high solar activity solar plasma clouds can be produced which interact with the Earth's magnetosphere, and may also deflect primary cosmogenic rays from their path. This results in decreased galactic cosmic ray flux during periods of high solar activity (Cerling & Craig, 1994). However, over 10^3 – 10^4 timescales reported here, the solar effects are averaged out. Temporal changes resulting from variations in the geomagnetic field strength and orientation are also important to consider. A weaker magnetic field allows greater penetration of cosmic

rays with lower energies and lower cut-off rigidities into the atmosphere, increasing cosmogenic production rates (Cerling & Craig, 1994).

1.1.2 Cosmogenic Nuclides

Cosmogenic nuclides are produced both in the atmosphere (meteoric nuclides), and *in situ* in rocks at the surface (*in situ* nuclides). As primary cosmic rays collide with the nuclei of atmospheric gasses, such as oxygen and nitrogen, meteoric cosmogenic nuclides are created as well as secondary neutrons and muons that continue the cascade to the surface (see *figure 1.1*). As the secondary particles (predominantly neutrons at sea level) collide with the lithosphere, *in situ* cosmogenic nuclides are created (Dunai, 2010). As a result of the loss of energy within the nuclear cascade, the production rate of *in situ* cosmogenic nuclides is lower than production rates in the atmosphere (Blard. *et al.*, 2008).

Cosmogenic isotopes can be produced by different nuclear reactions depending on the energy of the incoming particle. There are three principal mechanisms by which *in situ* cosmogenic isotopes can be produced: (a) by high energy spallation reactions with nucleons, (b) thermal neutron capture reactions, and (c) by muon-induced nuclear disintegrations (Lal, 1988). Most cosmogenic isotopes are predominantly produced by spallation reactions (mechanism discussed in section 1.1.1). Thermal neutron capture occurs when the residual energy reduces to <0.5 eV, and the neutron temperatures match those of their surroundings (Gosse & Phillips, 2001). These "thermal" neutrons can then be captured by nuclei producing unstable configurations

(Cerling & Craig, 1994). The third reaction involves production of cosmogenic nuclides from high-energy (fast) muon reactions or negative muon capture. Muons are produced along with neutrons in the nuclear cascade. They interact weakly with matter meaning that they do not produce many cosmogenic nuclides. However, this also allows them to penetrate further than nucleons into the atmosphere and lithosphere. Because of their greater penetration, muon-induced reactions become increasingly important with depth into the lithosphere (*figure 1.5*) (Dunai & Lifton, 2014).

The production of *in situ* cosmogenic nuclides decreases exponentially with depth as the secondary cosmic rays are attenuated in the lithosphere (*figure 1.5*) (Lal, 1991). In average crustal rocks, where spallogenic reactions are the most dominant source of production, the spallogenic production rate decreases by a factor of two with every ~40 cm depth below the surface. Thus, the concentration of nuclides becomes negligible below 2-3 m depth (Balco, *et al.*, 2008). This makes cosmogenic nuclides important tools in quantifying rates of many Earth surface processes. One such application is surface exposure dating. Surface exposure dating is based on the principal that the longer a rock or land-surface is exposed at the surface, the more time it has to accumulate cosmogenic nuclides. We can then convert measured nuclide concentrations into exposure ages, to date how long a rock or land-surface has been exposed to the atmosphere (Gosse & Phillips, 2001). This will be discussed further in section 1.1.8.

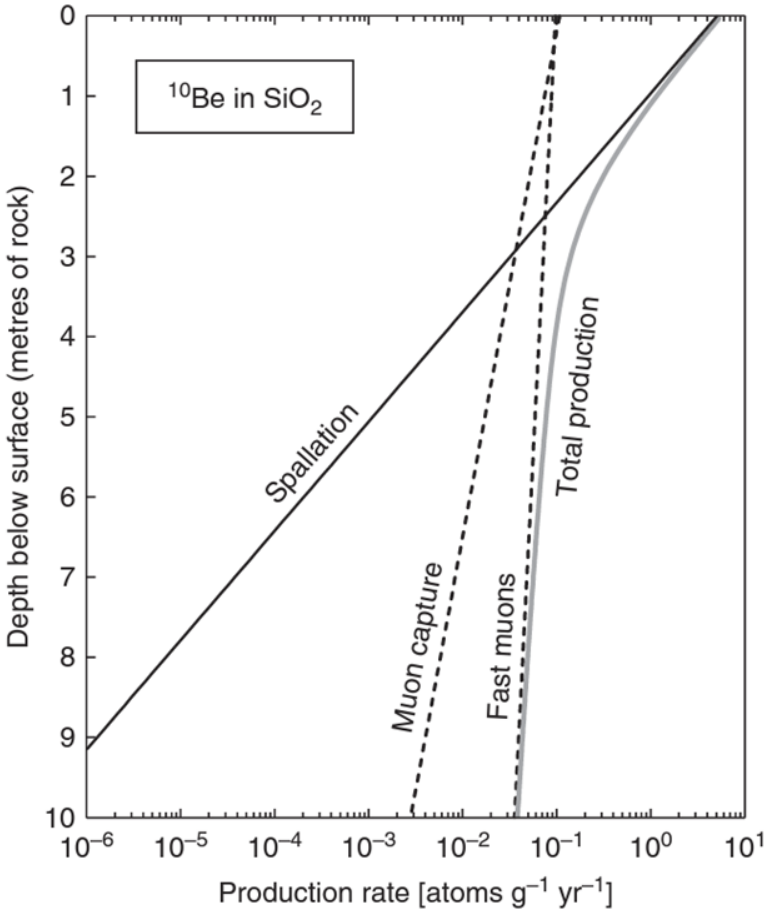

Figure 1.5: ^{10}Be production rates in quartz as a function of depth below the surface at sea level and high latitude, for a rock density of 2.7 g cm^{-3}. (Dunai, 2010).

1.1.3 Beryllium-10

A variety of cosmogenic nuclides are produced both in the atmosphere and lithosphere, with varying rates of production. The type of nuclide produced depends on the target element and the energy of the incoming cosmic ray (Gosse & Phillips, 2001). The nuclides most commonly applied to Earth surface studies are ^{3}He, ^{10}Be, ^{14}C, ^{21}Ne, ^{26}Al and ^{36}Cl (Gosse & Phillips, 2001). Beryllium-10 (^{10}Be) is the most widely used nuclide. It is radioactive, with a half-life of 1.39 Myr (Nishiizumi *et al.*,

2007; Chmeleff, *et al.*, 2010; Korschinek, *et al.*, 2010), and is only produced by interactions with cosmogenic rays (Dunai, 2010). *In situ* ^{10}Be is produced by predominantly spallation reactions, and to a lesser extent muon reactions (<1.5 %) with O and Si in rocks and land-surfaces (Gosse & Phillips, 2001; Braucher, *et al.* 2011). However, ^{10}Be is also produced in the atmosphere (meteoric ^{10}Be) from reactions with O and N, at a rate that is 10^3 times larger than the production rate in rocks (*figure 1.6*) (Blard, *et al.*, 2008). These meteoric ^{10}Be particles attach themselves to aerosols in the atmosphere and precipitate down where they are adsorbed by surface materials. For surface exposure dating, which is based on the concentration of *in situ* produced ^{10}Be, this meteoric contamination must be removed as it gives an older apparent age for the surface (Dunai, 2010).

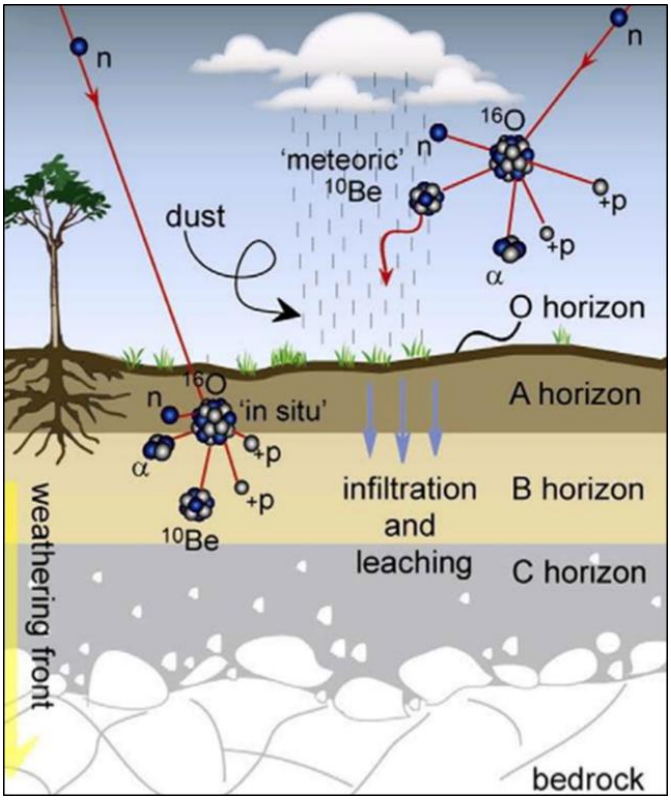

Figure 1.6: Schematic diagram showing ^{10}Be production *in situ* in the lithosphere and meteoric production in the atmosphere. Meteoric ^{10}Be is precipitated down and becomes incorporated in the rock or soil. (Willenbring & von Blanckenburg, 2010).

Quartz is the dominant mineral used in ^{10}Be studies as it is resistant and does not incorporate meteoric ^{10}Be into its structure as readily as other minerals. It also has a simple chemistry and is present in many geological settings. In the case of quartz, the chemical procedure to remove this meteoric contamination is relatively straight forward leaching in hydrofluoric acid (HF) (Kohl & Nishiizumi, 1992). This leaching removes the meteoric ^{10}Be from the outside of the grains, without completely dissolving the grain, therefore retaining the ^{10}Be produced *in situ* within the crystal lattice of the mineral (Willenbring & von Blanckenburg, 2010). ^{10}Be is produced in quartz at a rate of 3.9 - 5.4 atoms g^{-1} yr^{-1} at sea-level high-latitude (SLHL). The production rate is constantly being updated as new local production rates are calibrated, hence, a range of production rates are still commonly used (e.g. Balco, *et*

al., 2008; Heyman, 2014). The production rates also vary depending on the scaling scheme applied (Balco, *et al.*, 2008); this is further discussed in section 1.1.5.

However, quartz is not present in all environments, so we often have to resort to using other cosmogenic nuclides in other minerals. Currently mafic environments are restricted predominantly to the use of stable cosmogenic helium-3 (^{3}He), neon-21 (^{21}Ne), and radiogenic chlorine-36 (^{36}Cl). Both ^{3}He and ^{21}Ne are stable noble gasses, meaning they don't decay over time. These are both excellent for applications in mafic environments, however being stable nuclides, any inherited nuclides form previous exposure will not decay away over time as radioactive nuclides do. Additionally any isotopes present during crystallisation of the rock will remain in the minerals. Therefore, both ^{3}He and ^{21}Ne can contain an original amount of non-cosmogenically derived cosmogenic nuclides which can be released during crushing (Kurtz, 1986). Additionally, ^{21}Ne can be produced through nuclear reactions and also incorporated from the atmosphere. These complications make application difficult in some settings (Gosse & Phillips, 2001). Radiogenic nuclide ^{36}Cl can be effective for whole rock analyses; however, it has multiple production pathways on multiple elements, meaning production rates can be difficult to decipher in some settings (Phillips, *et al.*, 1996; Gosse & Phillips, 2001).

1.1.4 ^{10}Be in pyroxene as a chronometer

One of the aims of this masters project is to test and further develop a novel chronometer using ^{10}Be in pyroxenes (and olivines) to allow mafic environments to

be dated using the more commonly used and better constrained ^{10}Be cosmogenic nuclide. Pyroxenes have been widely used for cosmogenic ^{3}He studies. However, the development of ^{10}Be as a chronometer in pyroxenes allows a multi-nuclide approach with the ability to address complex exposure histories, which is not currently possible using a single stable nuclide in pyroxenes (Dunai, 2010). However, pyroxenes have dominant cleavage planes and are easily weathered in the surficial environment, meaning that it can be easily contaminated by meteoric ^{10}Be becoming incorporated into the structure of the mineral. Additionally, the complicated chemistry of pyroxene makes it difficult to separate the beryllium during chemistry, and also adds complexity into production rate calculations (Blard, *et al.*, 2008).

Using ^{10}Be in pyroxene and olivine as a chronometer has only been attempted a few times with varying results. Initially, Nishiizumi, *et al.* (1990) focused on ^{10}Be in olivine to exposure date lava flows with promising results. However, Ivy-Ochs, *et al.* (1998) discovered that ^{10}Be in pyroxene as a chronometer was unsuccessful due to contamination with meteoric ^{10}Be during weathering and clay formation, allowing the meteoric ^{10}Be to be locked within the interior of the grain. To address the contamination with meteoric ^{10}Be, Blard, *et al.* (2008) developed a decontamination procedure that effectively removed the meteoric ^{10}Be from pyroxene and olivine in basaltic lava flows. The Blard, *et al.* (2008) decontamination method uses a series of sequential leaches in weak acids followed by dissolution in hydrofluoric acid (HF) that aim to release the grain adsorbed meteoric ^{10}Be into an aqueous phase where it can be removed from the mineral, while leaving the *in situ* ^{10}Be remaining within the crystal lattice. Once the meteoric ^{10}Be is removed after leaching, the remaining pyroxene can then be dissolved and the *in situ* ^{10}Be concentration measured. Blard, *et*

al. (2008) proposes that a key step in the decontamination procedure is an initial crushing step, where the grains are powdered to <90 microns allowing the weathering pits and fractures containing meteoric ^{10}Be to be exposed, thereby allowing it to be leached out. Blard, *et al.* (2008) showed this decontamination method to be effective at removing meteoric ^{10}Be, allowing only the *in situ* ^{10}Be concentration to be measured. However, this method has not been tested since, and to become a viable method for common use, it must be tested using different rocks in a different laboratory. Testing this decontamination method is the first aim of this thesis.

1.1.5 Production rates

In addition to complete removal of meteoric ^{10}Be, the production rate of *in situ* ^{10}Be in pyroxene must be known before accurate exposure ages can be calculated. The concentration of cosmogenic nuclides in a rock is a function of the duration of exposure to cosmogenic rays, and the production rate of the nuclide in the target mineral (Cerling & Craig, 1994). *In situ* cosmogenic production rates due to spallation must be calibrated by measuring the nuclide concentration at an independently dated geological calibration site (Stone, 2000; Balco, *et al.* 2008). The calibration site must have a surface or land-form of a known age, which is stable and has been continuously exposed (Balco, *et al.*, 2008). Depending on the nature of the surface (e.g. lava flow, glacial feature, debris avalanche, etc.) different dating techniques can provide an independent age constraint, such as radiocarbon dating or luminescence (Bard, 1998; Gosse & Phillips, 2001). These local production rates are then normalised to sea-level and high latitude (SLHL). Many calibration sites have been established globally for different nuclides. As ^{10}Be in quartz is a commonly used

nuclide, the production rate for this isotope is relatively well constrained (Balco, *et al.*, 2008; Putnam, *et al.*, 2010; Heyman, 2014).

As production rates of cosmogenic nuclides also vary spatially and temporally (discussed in section 1.1.1), scaling schemes have been adopted to translate the local production rates derived from calibration sites to any location on the globe. The original scaling scheme was calculated by Lal (1991) based on the changes in production rate with elevation and latitude. However, as the use of cosmogenic nuclides has developed, more scaling schemes have been developed incorporating more parameters including time variations in the Earth's magnetic field, solar modulation, and cut-off rigidity. Five are currently in common use; these are summarised in *table 1.1* from Balco, *et al.* (2008). Each scaling scheme produces a different local production rate, so it is important to state which scaling scheme is being used when producing exposure ages and when scaling back to SLHL.

Table 1.1: Summary of most commonly used scaling schemes (Balco, *et al.*, 2008).

ID	References	Description
St	Lal (1991), Stone (2000)	Based on the latitude–altitude scaling factors of Lal (1991), as recast as functions of latitude and atmospheric pressure by Stone (2000). The scaling factor is a function of geographic latitude and atmospheric pressure. Does not take account of magnetic field variations—the nuclide production rate is constant over time
De	Desilets et al. (2006)	The scaling factor is a function of cutoff rigidity and atmospheric pressure. Production rates vary with time according to magnetic field changes
Du	Dunai (2001)	The scaling factor is a function of cutoff rigidity and atmospheric pressure. Production rates vary with time according to magnetic field changes
Li	Lifton et al. (2005)	The scaling factor is a function of cutoff rigidity, atmospheric pressure, and a solar modulation parameter. Production rates vary with time according to changes in solar output as well as changes in the Earth's magnetic field
Lm	Lal (1991), Stone (2000), Nishiizumi et al. (1989)	An adaptation of the Lal (1991) scaling scheme that accommodates paleomagnetic corrections. Production rates vary with time according to magnetic field changes. Based on the paleomagnetic correction described in Nishiizumi et al. (1989)

An online calculator is now available to calculate exposure ages and erosion rates. This CRONUS-Earth calculator is available online at http://hess.ess.washington.edu/math/. Balco, *et al.* (2008) created this calculator to combine all published production rate calibration measurements in an internally consistent fashion. A user can input sample information and measured ^{10}Be or ^{26}Al concentrations in a codified format, and the calculator will produce exposure ages based on the five main scaling schemes (Balco, *et al.*, 2008). As these methods are still developing, and there are still many uncertainties in nuclide production rates and scaling factors, continual improvements are being made to this calculator. Currently this calculator is only used for ^{10}Be and ^{26}Al measurements in quartz; however, ongoing updates to the calculator could soon include the use of additional nuclides in calculating exposure ages and erosion rates.

1.1.6 Production rate calibration sites in New Zealand

The production rate of ^{10}Be in quartz is relatively well known globally; however, most calibration sites are located in the mid-latitudes in the Northern Hemisphere. Until recently, ^{10}Be ages in the Southern Hemisphere were dependant on production rates that were extrapolated from the Northern Hemisphere using the above scaling schemes. To resolve this problem, Putnam, *et al.* (2010) derived a production rate for ^{10}Be in quartz in the Southern Alps of New Zealand using an independently dated debris-flow deposit at a calibration site. The age of the debris-flow was calculated

using ^{14}C in the soils and vegetation buried below the deposit. As a debris-flow is deposited in a single, rapid event, the exposure of the boulders on the surface of the deposit began immediately after deposition. A ^{10}Be production rate in atoms per gram per year (at. g^{-1} yr^{-1}) could then be calculated for the deposit, by dividing the concentration of *in situ* ^{10}Be measured in the boulders exposed at the top of the debris flow by the known age of the deposit (Putnam, *et al.*, 2010). The production rate at this site (scaled to SLHL) ranged between 3.74 atoms g^{-1} yr^{-1} and 4.15 atoms g^{-1} yr^{-1} depending on the scaling scheme applied. This is approximately 12-14% lower than the production rate previously used for exposure age calculations in New Zealand (Putnam, *et al.*, 2010). Therefore, exposure ages previously calculated for New Zealand sites using the global calibration dataset of Balco, *et al.* (2008), have been significantly underestimated. This production rate calculated for New Zealand can be applied to other locations in the Southern Hemisphere, but with decreasing confidence in locations such as Antarctica. The production rate for ^{10}Be in quartz in New Zealand is now relatively well known; however, production rates for nuclides in other minerals are still largely unknown.

To improve the dataset of nuclide production rates in New Zealand, Eaves, *et al.* (2015) established a production rate calibration site for ^{3}He in the central North Island of New Zealand. The deposit used for this calibration site was the Murimotu debris avalanche, on the ring-plain of Mount Ruapehu in the central North Island. Using radiocarbon dating of buried organic material, an independent age for the debris avalanche was calculated (Eaves, *et al.*, 2015). The concentration of ^{3}He was measured in pyroxenes from the boulders exposed at the surface of the deposit, allowing a production rate of ^{3}He in pyroxene to be established.

I have measured the ^{10}Be concentration in pyroxene remaining from the Eaves, *et al.* (2015) study, with the aim of establishing a production rate calibration site for ^{10}Be in pyroxene. As the production rate for ^{10}Be in pyroxene has only once been previously directly measured (Blard, *et al.* 2008), it provides an opportunity to test if it differs from the production rate in quartz. Establishing a production rate calibration site is the second aim of the thesis.

1.1.7 Application of ^{10}Be to Earth surface processes

As the cosmogenic nuclides only accumulate in the top few metres of the Earth's surface, they can be used to quantify many Earth surface processes. ^{10}Be is commonly used for erosion rate and burial studies (i.e. Nishiizumi, *et al.*, 1986; Bierman, 1994; Granger, *et al.*, 1996; Schaller, *et al.*, 2001), and exposure age studies (i.e.; Brown, *et al.*, 1991; Nishiizumi, *et al.*, 1991; Brook, *et al.*, 1995; Bentley, *et al.*, 2006; Putnam, *et al.*, 2010 Johnson, *et al.*, 2014). Only the application of ^{10}Be for surface exposure dating will be discussed in this thesis. As surface exposure dating is based on the principal that nuclides accumulate though time in rock exposed at Earth's surface, an exposure age can be calculated from a known nuclide concentration if the rate at which it is produced is known (Gosse & Phillips, 2001). Using exposure dating it is possible to constrain the ages of many land-forming processes, such as lava flows (e.g. Nishiizumi, *et al.*, 1990; Fenton, *et al.*, 2009), debris flows/landslides (e.g. Ivy-Ochs, *et al.*, 2009; Kubik & Ivy-Ochs, 2004) , fault scarps (e.g. Palumbo, *et al.*, 2004; van der Woerd, *et al.*, 2006; Benedetti, *et al.*, 2002; Schlagenhauf, *et al.*, 2011), fluvial deposits (e.g. Schaller, *et al.*, 2002; Norton, *et al.*, 2008) and both depositional

and erosional glacial features (e.g. Nishiizumi, *et al.*, 1991; Ackert, *et al.*, 1999; Stone, *et al.*, 2003; Douglass, *et al.*, 2006; Ivy-Ochs, *et al.*, 2007; Mackintosh, *et al.*, 2007; Bentley, *et al.*, 2010; Johnson, *et al.*, 2010; Todd, *et al.*, 2010). Surface exposure dating of glacial features are the focus of this thesis.

1.1.8 Application to glacial environments

Surface exposure dating can be used to calculate glacier retreat and advances. Glacial erosion can create fresh bedrock surfaces that only become exposed to cosmic rays once the glacier has retreated from the bed, as the ice above the bedrock provides a shield from cosmic rays (Balco, 2011). Thus, exposure ages of eroded bedrock can provide information on the timing of glacial retreat. Clasts, eroded from the glacier bed, are also shielded from cosmic rays whilst being transported within the glacier. Once these clasts are deposited as a moraine, or dropped out of the ice as an erratic during glacier retreat, they become exposed to cosmic rays and begin accumulating nuclides (Balco, 2011). Thus, cosmogenic nuclide exposure dating can be used to date both glacier retreat, and moraine emplacement (e.g. Ivy-Ochs, *et al.*, 1999; Mackintosh, *et al.*, 2007).

In order to calculate accurate exposure ages from ^{10}Be concentrations, there are three factors to consider for exposure dating in glacial environments: inheritance, erosion, and shielding. Radioactive cosmogenic nuclides decay over time, but for isotopes like ^{10}Be (half-life = ~1.39 Ma) complete decay can take many millions of years (Chmeleff, *et al.*, 2010; Korschinek, *et al.*, 2010). Thus, if a rock has previously been

exposed to cosmic rays, these nuclides may remain in the mineral as 'inherited' cosmogenic nuclides. In polar regions, with the growing and shrinking of ice sheets, the bedrock undergoes repeated periods of exposure. Unless significant erosion takes place, these inherited nuclides can remain in the rock. This can be the case for Quaternary glaciations with ~100 ka cycles in Antarctica, where little or no erosion has taken place (Staiger, *et al.*, 2006; Dunai, 2010).

The nuclide concentration in a rock is dependent on the amount of inherited nuclides and the erosion rate. The equation for this was introduced by Lal (1991) as:

$$N(t) = N(0)e^{-\lambda t} + \frac{P_0}{\lambda + \frac{\varepsilon}{\Lambda^*}} \times \left(1 - e^{-\left(\lambda + \frac{\varepsilon}{\Lambda^*}\right)t}\right) \tag{1.4}$$

Where: *N(t)* is the nuclide concentration at time t, *N(0)* is the inherited nuclide concentration, P_0 is the production rate, λ is the mean life time (ln(2)/halflife), ε is the erosion rate, and Λ^* is the attenuation path length. The first term is inheritance (ie. $N(t) = N(0)e^{-\lambda t}$), the second is exposure time on an eroding surface.

In glacial settings, erosion (and hence inheritance) is dependent on the basal thermal regime of the ice; the glacier can either be warm-based, or cold-based (Staiger, *et al.*, 2006). In warm-based 'temperate' glaciers, ice movement occurs along the ice-bedrock interface. These glaciers are extremely erosive as meltwater is present at the bed, helping to induce erosion of the bedrock via the process of regelation and plucking (Staiger, *et al.*, 2006). During a glacial advance, these warm-based glaciers

create a fresh rock surface, free from inheritance, provided that the glacier was erosive enough to remove the top ~2-3 m of bedrock, effectively removing the cosmogenic nuclides produced during any previous exposure (Fabel, *et al.*, 2002; Balco, 2011). Cold-based glaciers are less effective at erosion as the ice is frozen to the bed and glacier movement occurs via internal deformation within the ice (Cuffey, *et al.*, 2000; Jamieson, *et al.*, 2010). In regions with cold-based glaciers, inherited cosmogenic nuclides in the bedrock are common. Thus, striated or polished bedrock exposed after glacial retreat could provide an accurate exposure age only if sufficient erosion has occurred since prior exposure. If the inherited cosmogenic nuclides from pre-exposure have not been completely removed, the bedrock could provide an older exposure age.

Additionally, post-depositional erosion and weathering is important to consider, as it decreases the concentration of cosmogenic nuclides in the rock by removing the top surface containing the highest concentration of nuclides; thus, providing a younger apparent exposure age (Ivy-Ochs, *et al.*, 2007). When calculating exposure ages, erosion rates in the environment must be considered (Balco, 2010). In an actively eroding landscape, and if inheritance is assumed to be zero, equation 1.4 can be simplified to:

$$N(t) = \frac{P_0}{\lambda + \frac{\varepsilon}{\Lambda^*}} \times \left(1 - e^{-\left(\lambda + \frac{\varepsilon}{\Lambda^*}\right)t}\right) \tag{1.5}$$

The last major factor to consider when calculating exposure ages is shielding. Corrections must be made for topographic and self-shielding, and shielding by snow or sediment cover (Dunne, *et al.*, 1999; Schildgen, *et al.*, 2005). As cosmic rays come

from all directions, any object obscuring the horizon (i.e. mountains, trees) can lower the cosmic ray flux at a site by blocking the incoming cosmic rays; lowering the production rate of cosmogenic nuclides. This topographic shielding must be measured at the sample site in order to correct for it (Cerling & Craig, 1994). To assess the topographic shielding at a site, the inclination to the horizon is measured using a clinomer (Dunne, *et al.*, 1999). The topographic shielding factor at a site for a series of *n* obstructions can be calculated using the equation:

$$S_{topo} = 1 - \frac{1}{360°} \sum_{i=1}^{n} \Delta\emptyset i \ sin^{m+1} \theta i \qquad (1.6)$$

Where *n* is the obstruction, $\Delta\emptyset i$ is the inclination above the horizon, θi is the azimuthal width of the obstruction, and *m* is an exponent, usually reported as 2.3 (Dunne, *et al.*, 1999).

Self-shielding of the sample occurs if the sample is taken from a dipping surface; this can be accounted for similar to topographic shielding. Shielding can also occur from temporary burial of the sample site, for example, by snow, sediment, vegetation or volcanic ash cover (Dunai, 2010). This reduces the cosmic ray flux to the surface for an unknown period of time. The duration and thickness of cover is hard to estimate; however, most covers are calculated to only have minimal effects on the production rate. All of these factors (inheritance, erosion and shielding) can influence the cosmogenic nuclide concentration at any given site, providing a complex exposure history (Lilly, *et al.*, 2010).

In some settings, a multi-nuclide approach can provide information on complex exposure histories, such as bedrock with multiple episodes of exposure and burial. This multi-nuclide approach uses two cosmogenic nuclides that can be measured in the same mineral, for example, ^{10}Be and ^{26}Al in quartz. It works on the basis that these nuclides have different decay constants and production rates. The half-life of ^{10}Be is ~1.39 Ma, and for ^{26}Al is ~708 ka (Dunai, 2010), therefore ^{26}Al decays faster than ^{10}Be. If a rock has experienced a period of shielding, twice as much ^{26}Al would decay than ^{10}Be, leading to discordant age estimates. If the ^{10}Be concentration is plotted against the ^{26}Al/^{10}Be ratio in the sample, complex exposure histories can be determined (Granger & Muzikar, 2001; Lilly, *et al.*, 2010; Darvill, 2013). The development of ^{10}Be in other minerals, such as pyroxene, will allow a multi-nuclide approach of ^{10}Be with other cosmogenic nuclides, such as ^{3}He, to allow complex exposure histories to be determined in environments where this is currently not possible.

1.1.9 Application of surface exposure dating in Antarctica

Glaciers in Antarctica are predominantly cold-based, meaning that during glacial advances they may not erode enough of the bedrock to effectively remove all cosmogenic nuclides produced during previous exposure (Lloyd Davies, *et al.*, 2009; Atkins, 2013; Mackintosh, *et al.*, 2014). For a bedrock surface to be cosmogenically 'reset' to a zero age surface, ~2-3 m of rock must be removed (Fabel, *et al.*, 2002). This means that exposure ages calculated from exposed bedrock post-glacier retreat, will likely contain inherited cosmogenic nuclides and will not provide an accurate

exposure age for the timing of retreat. There is no obvious way to tell in the field whether a striated bedrock surface has been fully reset since the last glacial exposure, or if it will still contain inherited nuclides (Balco, 2011). In Antarctica, bedrock samples are not expected to provide accurate ages of glacial retreat, but they may provide information about bedrock erosion rates (Balco, *et al.*, 2013). Thus, for accurate glacial chronologies, depositional glacial deposits, such as moraines or glacial erratics, are more commonly used.

Depositional glacial features may contain a mixture of material sourced from rocks that have been shielded by cosmic rays, and rocks that have experienced prior exposure and will contain inherited cosmogenic nuclides (Atkins, 2013; Mackintosh, *et al.*, 2014). While there is again no obvious way to tell them apart in the field, if a large number of samples are collected it is easier to spot the outliers containing inherited nuclides once exposure ages are calculated (Dunai, 2010). Moraines begin as a steep-sided ridge of sediment, but become eroded over time. When sampling from moraines it is important to consider the effects of surface lowering of the moraine, exhuming boulders that were initially buried in the moraine and have not always been exposed to cosmic ray flux (Bierman, 1994). Samples should be collected from boulders on the crest of the moraine as boulders on the flanks may have been later exhumed, or gravitationally rotated to their current position, meaning that the current top surface of the boulder may not have always been exposed to cosmic ray flux (Putkonen & Swanson, 2003; Ivy-Ochs, *et al.*, 2007; Dunai, 2010).

Glacial erratics perched upon striated or polished bedrock are commonly used to obtain glacial chronologies and can be used to constrain thinning rates of glaciers.

Glacial erratics must show evidence of glacial transport, including striations, faceting or polishing, and exotic lithologies to the bedrock beneath (Balco, *et al.*, 2013). It is important that these clasts have not moved since deposition, and have not been sampled near slopes where they could have been delivered by rolling. Chronologies for ice surface lowering can be obtained using the 'dipstick' method. The dipstick method uses glacially transported cobbles collected from elevation transects on nunataks or mountains adjacent to the glacier, to reconstruct ice surface lowering using cosmogenic nuclides. As the glacier thins, cobbles exposed at higher elevations become exposed to cosmic ray flux first. Thus, the samples at higher elevations should have a higher ^{10}Be concentration, and therefore an older exposure age than the samples at lower elevations closer to the current glacier position (Stone, *et al.*, 2003; Mackintosh, *et al.*, 2007).

1.1.10 Thinning rates of Mackay Glacier, Antarctica

Using the 'dipstick' method, Jones, *et al.* (submitted) recorded surface lowering at two nunataks in the lower Mackay Glacier (Gondola Ridge/Mount Suess and Low Ridge, located 15-25 km and at the current glacier terminus, respectively) using ^{10}Be in quartz. Mackay Glacier is an East Antarctic Ice Sheet outlet glacier located in Southern Victoria Land, Antarctica. They found that the glacier was ~260m thicker here at the Last Glacial Maximum (LGM), and that an episode of rapid thinning occurred at ~8-7 ka. However, pyroxene- rather than quartz-bearing rocks at Mount Gran have so far prevented obtaining a record of glacier response further upstream (~35 km from the terminus). The third aim of this thesis is to exposure date cobble erratics, using ^{10}Be in pyroxene, that have been deposited on the flanks of Mount

Gran, adjacent to Mackay Glacier, with the aim of constraining past ice thickness and subsequent thinning of the upper Mackay Glacier since the LGM.

1.2 Antarctic ice sheet thinning since the LGM

Understanding the thinning history of the Antarctic ice sheets since the LGM is important in understanding and predicting its present and future behaviour (Anderson, *et al.*, 2002; Mackintosh, *et al.*, 2014). The volume of Antarctic ice during the LGM and subsequent ice loss are important to quantify in order to constrain the sources of meltwater contributing to eustatic sea-level rise since the LGM. The timing of these meltwater contributions are also important, however, field observations are sparse, particularly for East Antarctica (Anderson, *et al.*, 2002, Mackintosh, *et al.*, 2014). The LGM occurred 26.5 – 19 ka (Clark, *et al.*, 2009) and was characterised by a sea level 120 – 135 m lower than present (Clark & Mix, 2002; Milne, *et al.*, 2002; Peltier, 2002). Sea level began rising at ~20 ka as the Earth began the transition from glacial to interglacial conditions (Denton *et al.*, 2011).

At present, ~58 m of sea-level equivalent is contained within Antarctic ice sheets and glaciers (Fretwell, *et al.*, 2013). The continent is divided into West Antarctica and East Antarctica, which are covered by two major ice sheets; the West Antarctic Ice Sheet (WAIS) and the East Antarctic Ice Sheet (EAIS), respectively. The WAIS is largely grounded below sea level and contains ~5 m sea-level equivalent (Pollard & DeConto, 2009). As it is grounded below sea level, it is more vulnerable to collapse by unstable grounding line retreat as ocean temperatures rise (Mercer, 1978; Joughin

& Alley, 2011). The EAIS holds a sea-level equivalent of ~53 m, and is thought to be more stable as it is grounded predominantly above sea level (Fretwell, *et al.*, 2013).

1.2.1 Volume of Antarctic ice during the LGM and subsequent ice loss

The Antarctic ice sheets did not contribute equal amounts to post LGM sea-level rise, and did not retreat simultaneously (Bentley, *et al.*, 2014). Different models show varying contributions from the Antarctic ice sheets to eustatic sea-level rise since the LGM. Models of Nakada and Lambeck (1989) suggest up to 20-30 m of post-LGM sea-level rise originated from Antarctica. However, more recent studies claim this is an overestimate. For example, Golledge, *et al.* (2013) suggest that Antarctica contributed only ~8.3 m to post-LGM eustatic sea-level rise, which agrees well with values determined by Whitehouse, *et al.* (2012) of 9 ± 1.5 m, and Mackintosh, *et al.* (2011) of ~10 m.

The maximum extent of the Antarctic ice sheet during the LGM is recorded by glacial geomorphic features and sedimentary deposits on the continental shelf (Anderson, *et al.*, 2002; Denton & Hughes, 2002). During the LGM the WAIS extended to the mid-outer continental shelf (Anderson, *et al.*, 2002). The EAIS advanced to the outer continental shelf in some regions, while in others it did not advance at all from its current position (Bentley, *et al.*, 2014). Ice core evidence and ice sheet modelling suggest that the central domes of the EAIS were approximately 100 m lower than present in some locations (Bentley, *et al., 2014).* Since the LGM, the WAIS has contributed ~9 m to eustatic sea-level, while the EAIS is believed to have only

contributed ~1 m, as the ice mass thickened slightly at its margin, and thinned in the interior (Mackintosh, *et al*., 2011).

1.2.2 Timing of advance and retreat

Establishing the timing of ice sheet and glacial advance and retreat is a challenge. Dating glacial deposits on the continental shelf (such as grounding zone wedges, or glacial drifts) rely predominantly on dating of organic materials via radiocarbon (^{14}C). This is difficult in Antarctic waters because of ^{14}C recycling (Anderson, *et al.*, 2002). Onshore evidence for past glaciation is sparse as the continent remains predominantly ice covered (Mackintosh, *et al.*, 2014). However, ice core analysis, numerical modelling, and direct glacial geological and geomorphic evidence for past glacial expansion or retreat can be used to reconstruct former ice extents, and the timing of glacial retreat or thinning can be determined using cosmogenic nuclide surface exposure dating (Bentley, 1999).

Based on offshore marine sediments, and terrestrial cosmogenic exposure ages, the timing of the maximum ice extent and subsequent retreat of the WAIS and EAIS were not in phase. At ~20 ka, the ice sheet at some locations had not yet reached full LGM ice extent, while the grounding-line had already began retreating at other locations (Bentley, et al., 2014). Retreat of the ice sheets from the outer shelf was not synchronous. The WAIS began retreating from the outer shelf in the Ross Sea embayment by ~10 ka (Conway, *et al.*, 1999; Bentley, *et al.*, 2014). However, the EAIS began retreat from the Ross Sea embayment earlier, at ~13 ka, with the most

rapid retreat occurring during the Holocene (Anderson, et al., 2014). Elsewhere, the timing of retreat of the EAIS is less constrained. At the Lambert/Amery glacial system on the EAIS margin, retreat began as early as 18 ka, while the rest of the ice remained at its maximum extent during this time. However, rapid retreat and thinning were occurring for the entire EAIS by 10 ka (Mackintosh, *et al.*, 2014).

1.2.3 Glacial thinning

As retreat since the LGM was non-synchronous across the continent, understanding the mechanisms behind individual glacier retreat is important in determining the potential threat of ice sheet retreat in response to increased atmospheric and ocean temperatures. External forcing's such as ocean and atmospheric temperatures and sea-level rise, along with internal factors such as local bed topography, will influence glacial retreat. Determining the relative importance of each of these factors is important in predicting future glacier response (Mackintosh, *et al.*, 2011; Golledge, *et al.*, 2012; Jamieson, *et al.*, 2012).

Mackay Glacier, an EAIS outlet glacier, has experienced rapid thinning during the early-mid Holocene, in the absence of significant changes in atmospheric and oceanic temperatures, or eustatic sea-level (Jones, *et al.*, submitted). However, this phase of rapid thinning was coeval with retreat of the grounding line into an over-deepened trough, suggesting that local bed topography has a large influence on glacial thinning dynamics (Jones, *et al.*, submitted). Understanding the response of the upper Mackay

Glacier during this thinning episode is important to complete the thinning and retreat history of the glacier.

1.3 Research Question

In this thesis, I attempt to answer three research questions:

1. Can proposed leaching techniques completely remove meteoric ^{10}Be from pyroxene in New Zealand's igneous rocks?
2. What is the ^{10}Be production rate for pyroxene in New Zealand?
3. Can this decontamination method and production rate for ^{10}Be in pyroxene be applied to undated cobble erratics and bedrock samples from Mount Gran in Antarctica to allow better understanding of the thinning and glacial history of Mackay Glacier?

Chapter Two: Methods

This chapter is structured in the following manner; the sample locations and lithologies are outlined in section 2.1, sample collection techniques and sample preparation are discussed in section 2.2, and section 2.3, respectively. Lastly, the chemistry for removal of meteoric ^{10}Be and isolation of the *in situ* ^{10}Be is discussed in section 2.4. This section is further subdivided into method development and the Blard *et al.* (2008) leach verification in section 2.4.1, and column calibration experiments and beryllium precipitation in section 2.4.2.

2.1 Sample localities

The samples were collected from two localities in order to test and apply the method using two different rock types; Mount Ruapehu andesites in New Zealand, and Mount Gran diorites in Antarctica.

2.1.1 Mount Ruapehu

2.1.1.1 Location

Samples were collected from two locations on and around Mount Ruapehu. Mount Ruapehu (2797 m) is an active andesite-dacite volcano located in the Taupo Volcano Zone in the central North Island of New Zealand (39°28'S, 175°56'E). During the

LGM a small ice cap covered the summit and fed valley glaciers that descended to ~1200 m a.s.l (McArthur & Shepherd, 1990). A sample (originally named WH-12-04 but renamed JC2 during chemistry) was collected by S. Eaves from a boulder exposed at the crest of the Wahianoa Valley moraine on the south-eastern side of the mountain at an elevation of 1483 m a.s.l (location in *figure 2.1* and sample photos in *figure 2.2*). The Wahianoa moraines are ~5 km long lateral moraines formed by the Wahianoa Glacier during the LGM (McArthur & Shepherd, 1990). This sample was used to test the Blard, *et al.* (2008) decontamination procedure of complete removal of the meteoric ^{10}Be from the sample, as cosmogenic ^{3}He has already been measured in this sample and can be used as an independent constraint.

Additionally, four samples (MM-12-01 to MM-12-04) were collected from boulders exposed in a debris avalanche in the north-west volcanic ring-plain (sample locations in *figure 2.3* and sample photos in *figure 2.4*). The Murimotu debris avalanche has been dated using the radiocarbon age of organic material buried within the deposit by Eaves, *et al.* (2015), to have occurred 10597 ± 110 years B.P. from a gravitational sector collapse on Mount Ruapehu.

2.1.1.2 Lithology

Mount Ruapehu has been constructed over the last ~250 kyr by a series of eruptive events separated by periods of erosion and sector collapse (Hackett, 1985; Hackett & Houghton, 1989). There are four major formations recognised, with a chronology dating back to ~250 kyr (Gamble, *et al.*, 2003). The lavas are predominantly andesitic with phenocryst assemblages dominated by plagioclase, with lesser amounts of clinopyroxene, orthopyroxene, Fe-Ti oxides, and rare olivine and amphibole.

Ortho- and clinopyroxenes generally make up 10-20% of the phenocryst assemblages in the andesites found on Mount Ruapehu (Price, *et al.* 2012), making them ideal to test the Blard, *et al.* (2008) decontamination procedure of removal of meteoritic ^{10}Be in pyroxene. The sample collected from the Wahianoa moraine likely originated from the Wahianoa Formation as the Wahianoa glacier eroded into this formation. This formation is aged between 115 and 160 ka (Gamble, *et al.*, 2003). The four samples collected from the Murimotu debris avalanche are from an unknown source on the upper mountain.

2.1.1.3 Reason for site selections

Sample JC2, collected on the Wahianoa moraine, has been previously exposure dated using cosmogenic ^{3}He in pyroxene by S. Eaves (pers. comm.) providing an age for the sample against which we can test ^{10}Be as a chronometer. These rocks are relatively young and unweathered providing a good analogue to allow us to assess whether the decontamination method is reliable and accurate. The Murimotu samples have been used to establish a production rate site for ^{3}He in pyroxene in New Zealand by Eaves, *et al.* (2015). Using the same pyroxene we aim to establish a production rate calibration site for ^{10}Be in pyroxene using direct cross-calibration with the cosmogenic ^{3}He concentration and the radiocarbon age of the deposit.

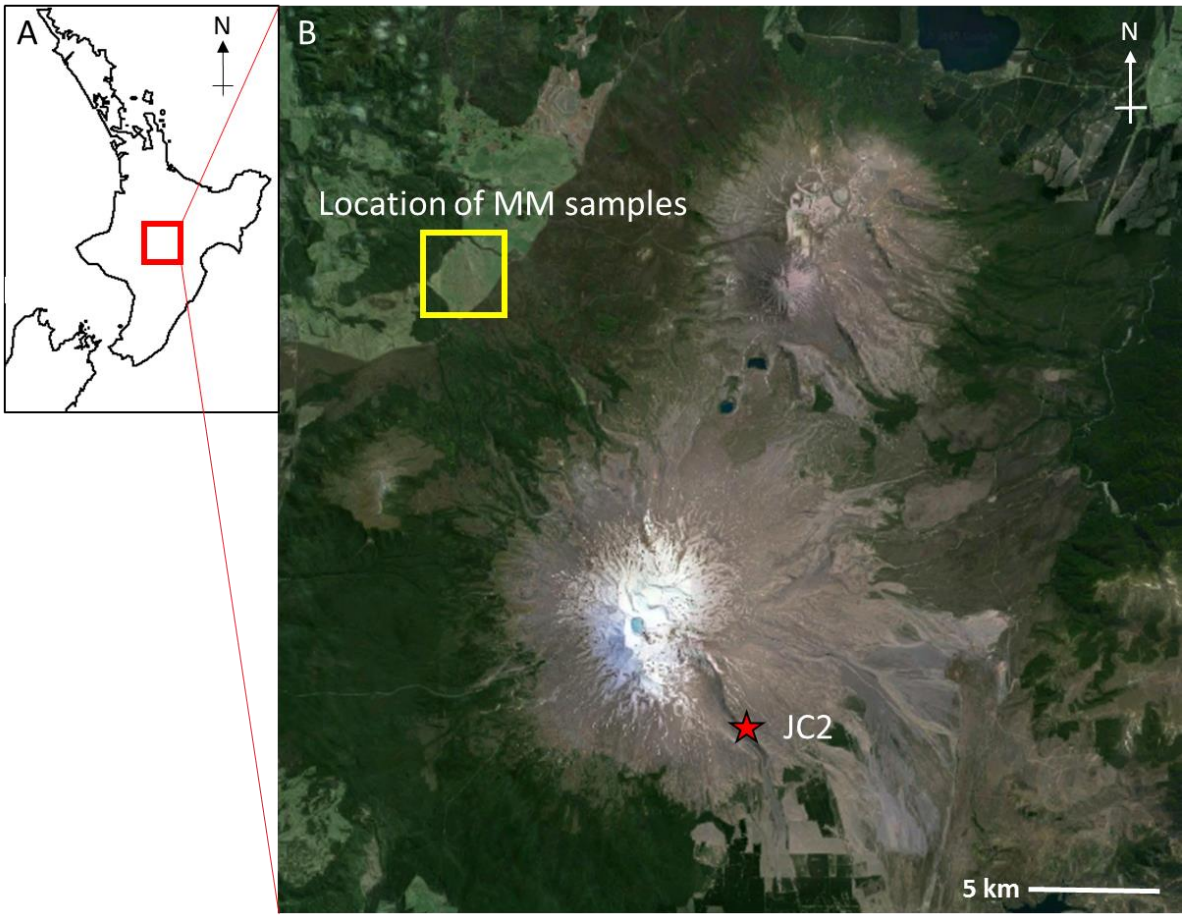

Figure 2.1: (A) Outline of the North Island of New Zealand. Red box denotes enlarged area in B. (B) Satellite image of Mt Ruapehu. Red star denotes sample location JC2 and yellow box shows location of the Murimotu samples (enlarged in *figure 2.3*). (Modified from Google Maps)

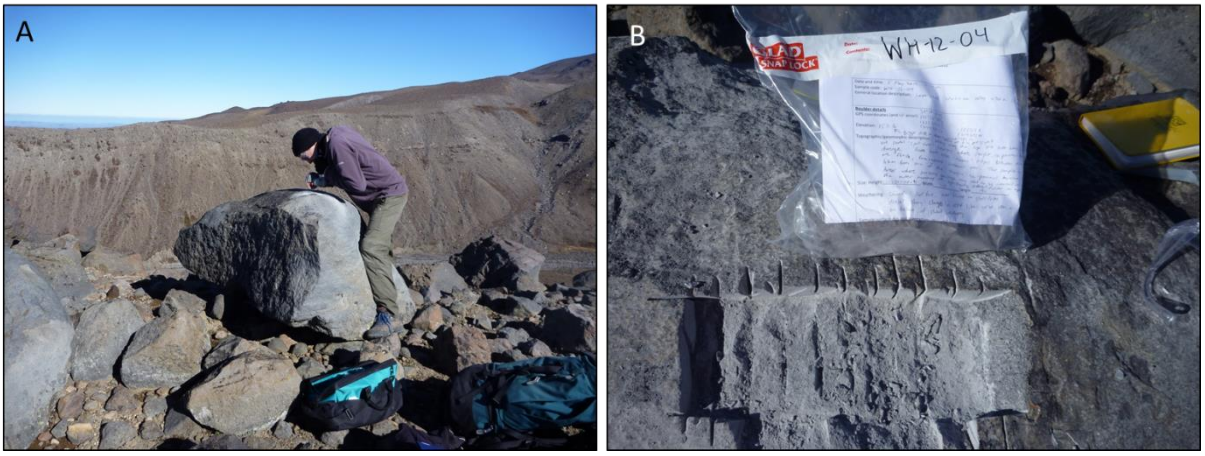

Figure 2.2: (A) Parent boulder for sample JC2 (originally named WH-12-04) collected on the Wahianoa Moraine. (B) sampled surface for JC2. (Photos supplied by S. Eaves).

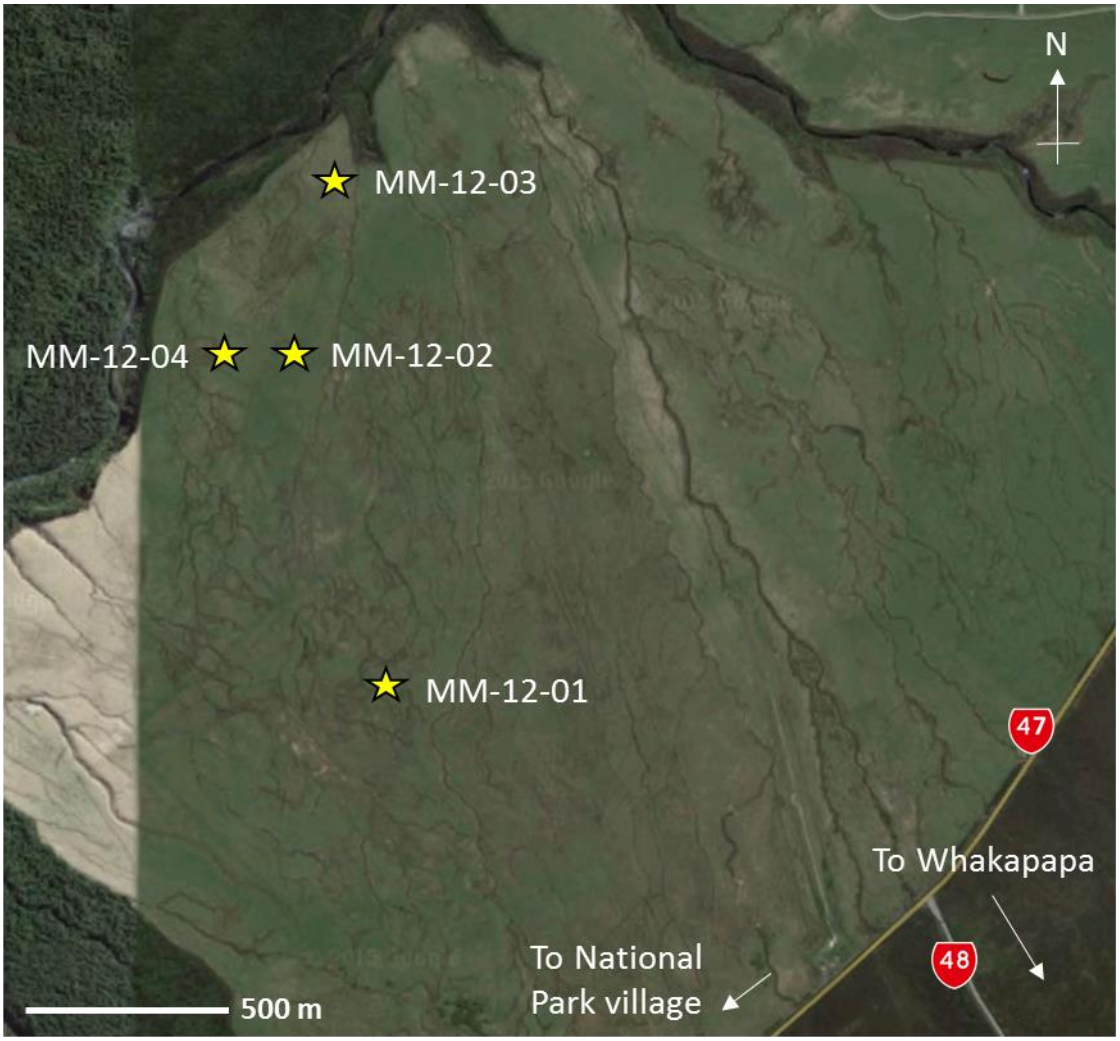

Figure 2.3: Location of Murimotu samples (enlarged from yellow box in *figure 2.1*). (Modified from Google Earth).

Figure 2.4: (A, C, E, G) Parent boulders for samples MM-12-01, MM-12-02, MM-12-03, MM-12-04, respectively. (B) The smaller boulder on top of the parent boulder for MM-12-01 sampled. (D, F, H) sampled surfaces of each boulder, respectively. (Photos supplied by S. Eaves).

2.1.2 Mount Gran

2.1.2.1 Location

Mount Gran (approximately 77°S, 161°E) is located in Southern Victoria Land on the edge of the EAIS (*figure 2.5*). Mount Gran is adjacent to the upper Mackay Glacier, an outlet glacier of the EAIS that flows through the Transantarctic Mountains into the Ross Sea. Eight cobble erratics (sample named MG01 – MG32 – sample photos in *figure 2.6)* and four basement rock dolerites (sample named MG02-B – MG22-B – sample photos in *figure 2.7*) were collected along an elevation transect from 970.381 m a.s.l to 1043.359 m a.s.l in order to attain surface lowering rates on the adjacent upper Mackay Glacier (*figure 2.8*). Additionally, five weathered bedrock samples (named MGW 01-05) were collected from Mount Gran with the purpose to assess any potential age gradient between minimally and extremely weathered bedrock.

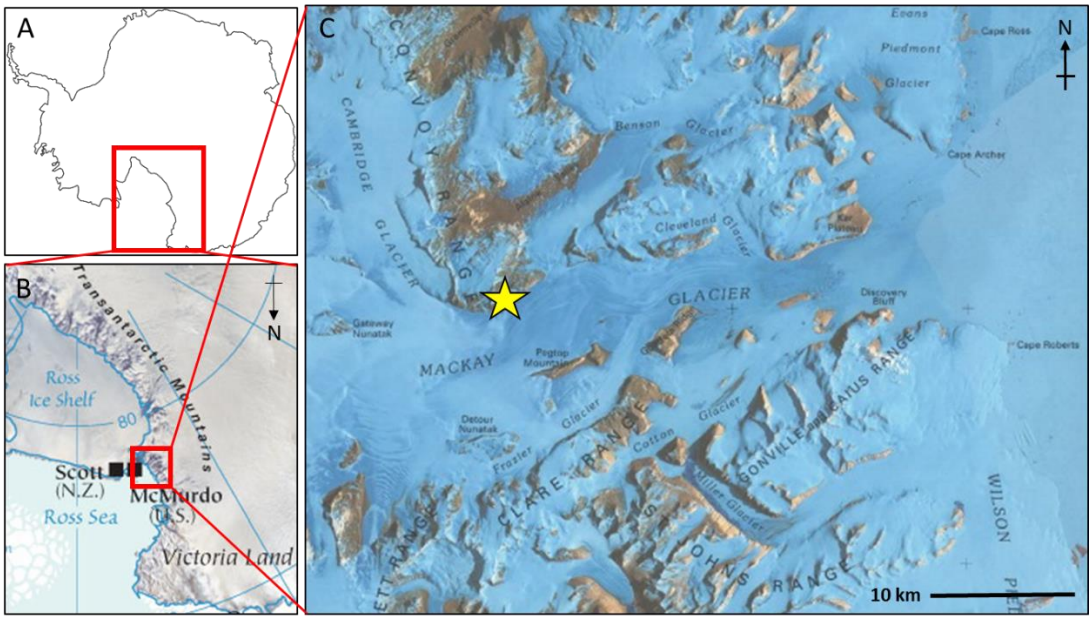

Figure 2.5: (A) Outline of Antarctica, red box enlarged in B. (B) Ross Sea region, red box enlarged in C (modified from nationsonline.org). (C) Map of Mackay Glacier, located in the Transantarctic Mountains in Southern Victoria Land (modified from Polar Geospatial Centre). Note the north arrow directional change between B and C. Yellow star denotes location of samples taken on Mount Gran.

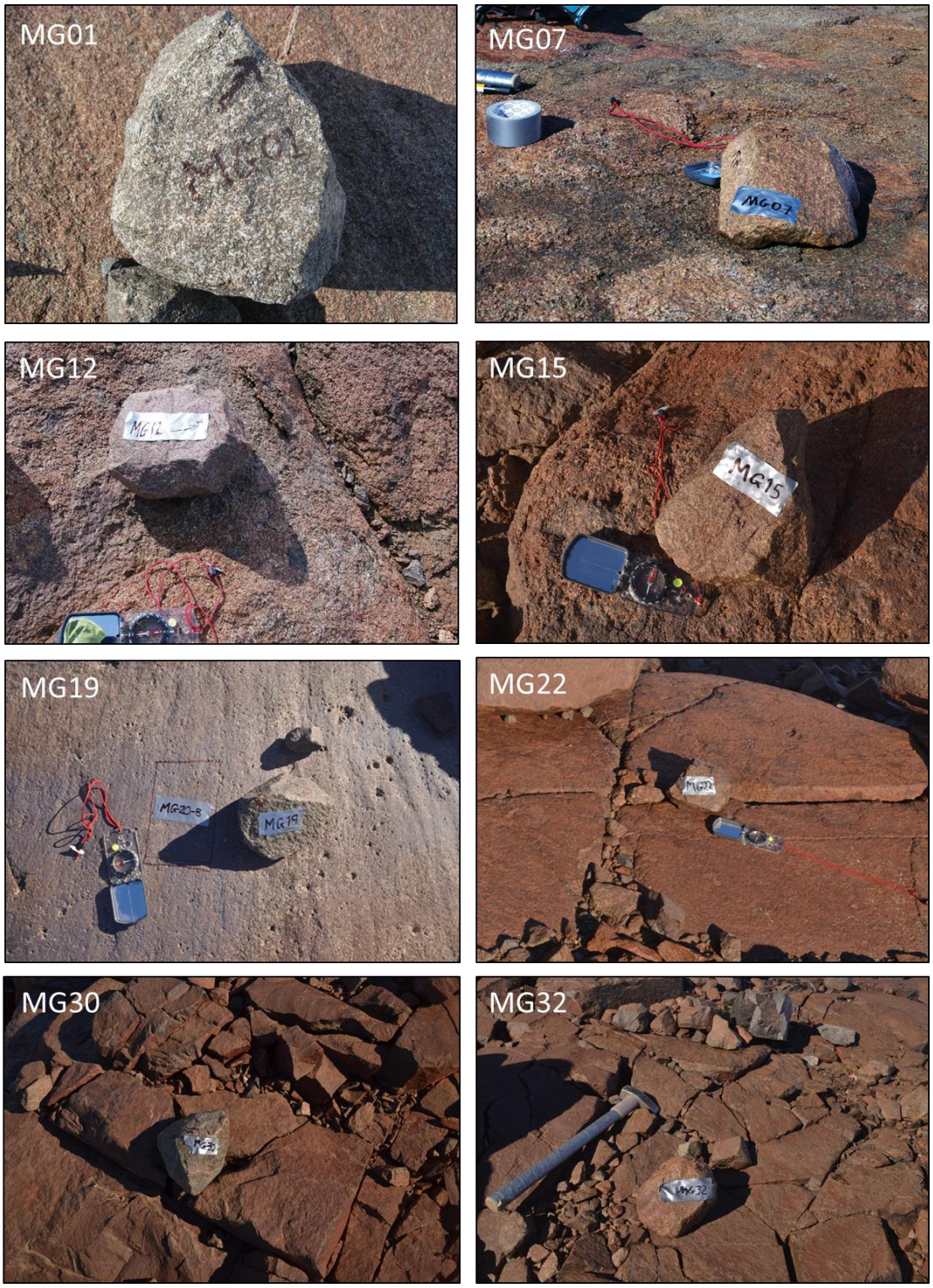

Figure 2.6: Sampled cobbles on Mount Gran. Note sample MG19 is the cobble; the bedrock MG20-B was also sampled, however the ^{10}Be concentration could not be obtained. (Photos supplied by R. Jones).

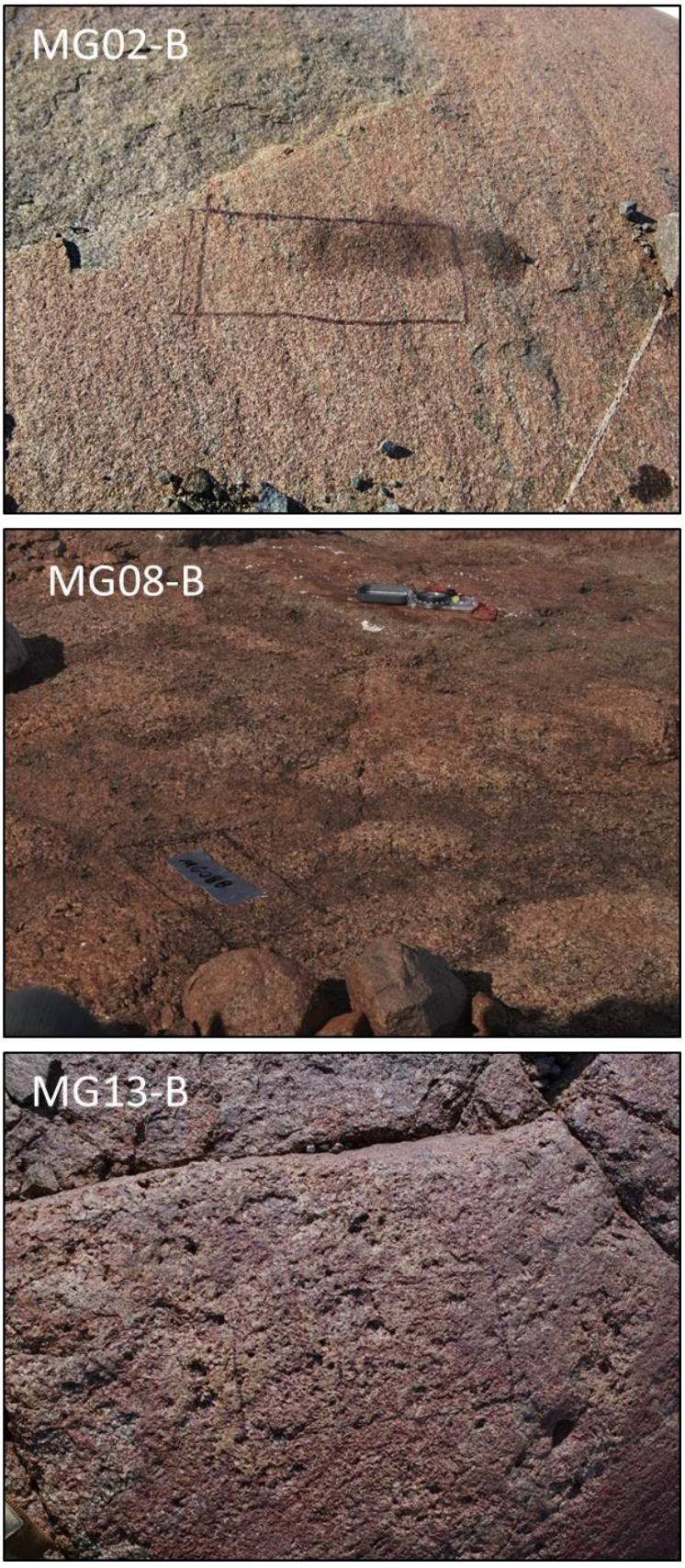

Figure 2.7: Sampled bedrock on Mount Gran. (Photos supplied by R. Jones).

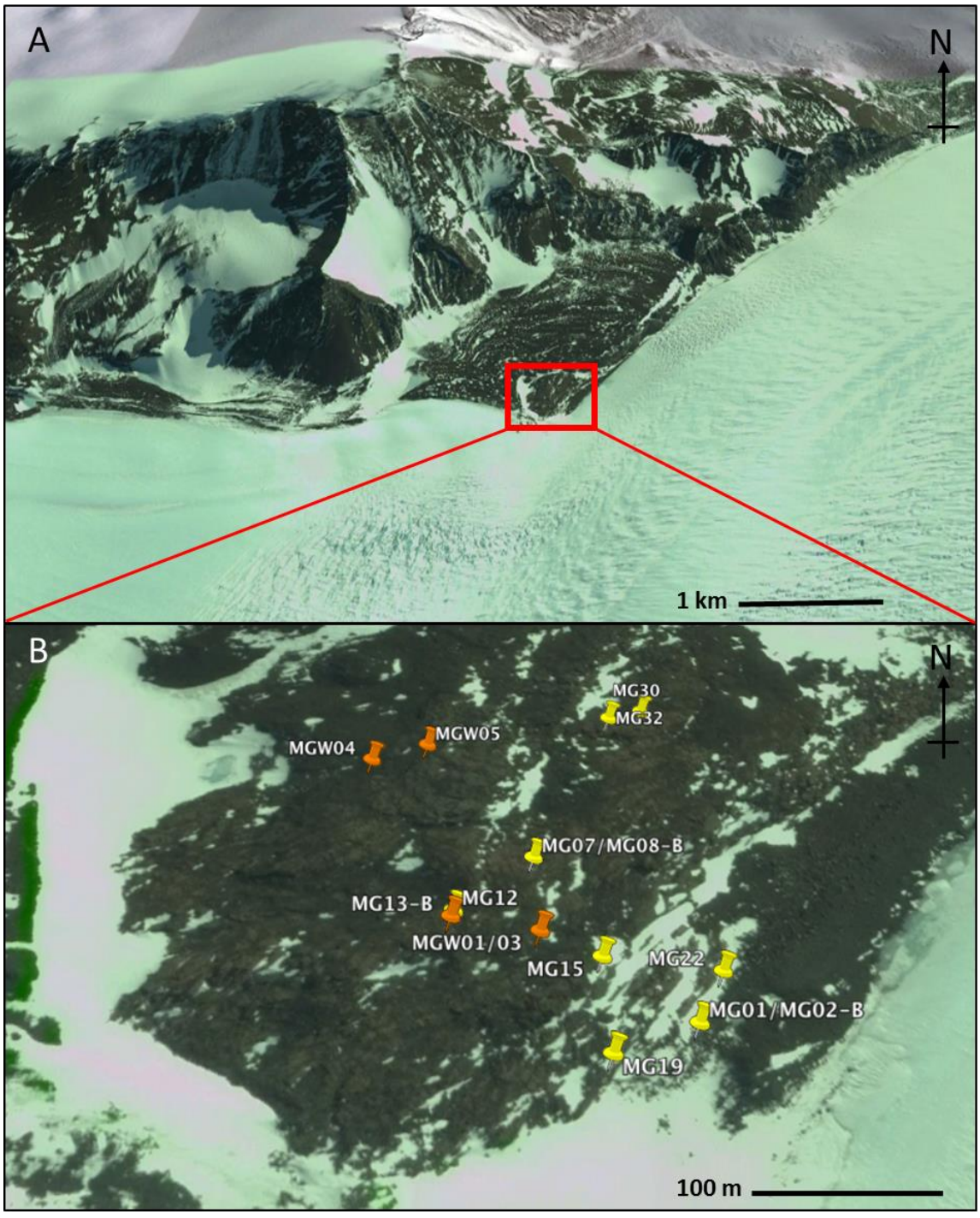

Figure 2.8: Sample locations on Mt Gran. (A) Location of yellow star in *figure 2.5(C)*. Red box expanded in B. (B) location of samples. Yellow pins denote locations where cobbles collected, orange pins where bedrock samples taken. Note at sample sites MG01/MG02-B and MG07/MG08-B both a cobble and bedrock sample were taken. (Modified from Google Earth Pro).

2.1.2.2 Lithology

There are three major rock formations that make up Mount Gran: the basement rock sequence of granites and gneisses of Precambrian age, the Beacon Sandstone of Silurian to Jurassic age, and the Ferrar Dolerites of probable Jurassic or Cretaceous age, which occur as three major sills that are indistinguishable at Mount Gran (Mirksy, *et al.*, 1965). The Ferrar Dolerites occupy the largest part of the Mount Gran area and outcrop on southern Mount Gran where the samples were collected. The sills are tholeiitic and consist of plagioclase, the pyroxenes pigeonite, augite and hypersthene in varying proportions, and smaller amounts of opaques and accessory minerals (Mirksy, *et al.*, 1965).

Five thin sections were analysed (MG 02-B, 07, 13-B, 19 and 32 – photos in *figure 2.9a-e*) to determine modal proportions and degrees of weathering affecting the pyroxenes. In the five samples analysed the abundance of pyroxene varied between 10-20%. Plagioclase is the most abundant mineral in all samples with a proportion of ~80%, with ~10% opaques and other accessory minerals. The pyroxenes were up to 2 mm in length (up to 4 mm in MG 32) and were mainly clinopyroxene, with only small amounts of orthopyroxene. The degree of alteration of pyroxenes varied between samples, and many were intergrown with plagioclase. Many of the pyroxenes showed evidence for dissolution around the grain boundaries.

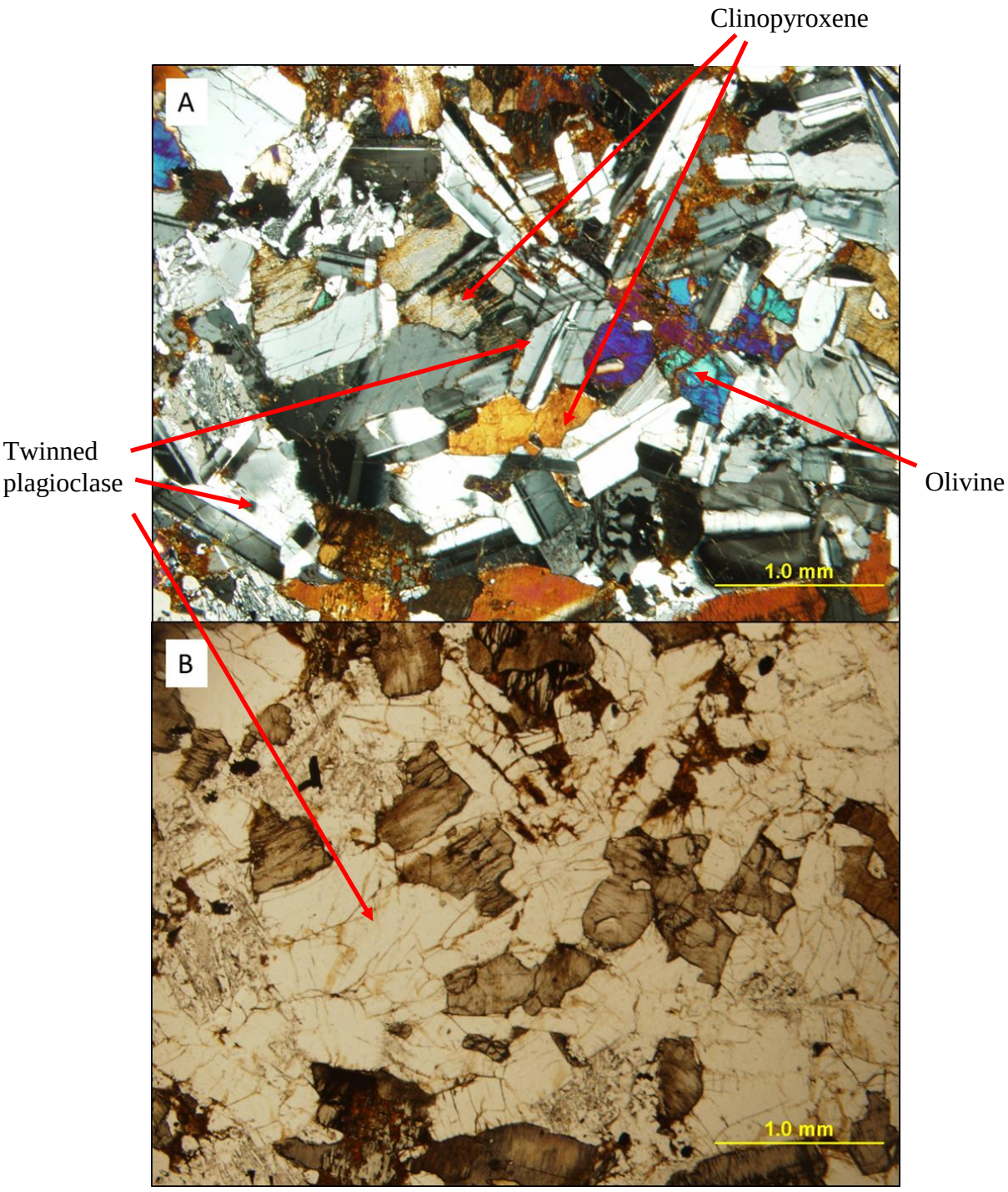

Figure 2.9a: Bedrock sample MG02-B in cross polarised light (A), and plane polarised light (B).

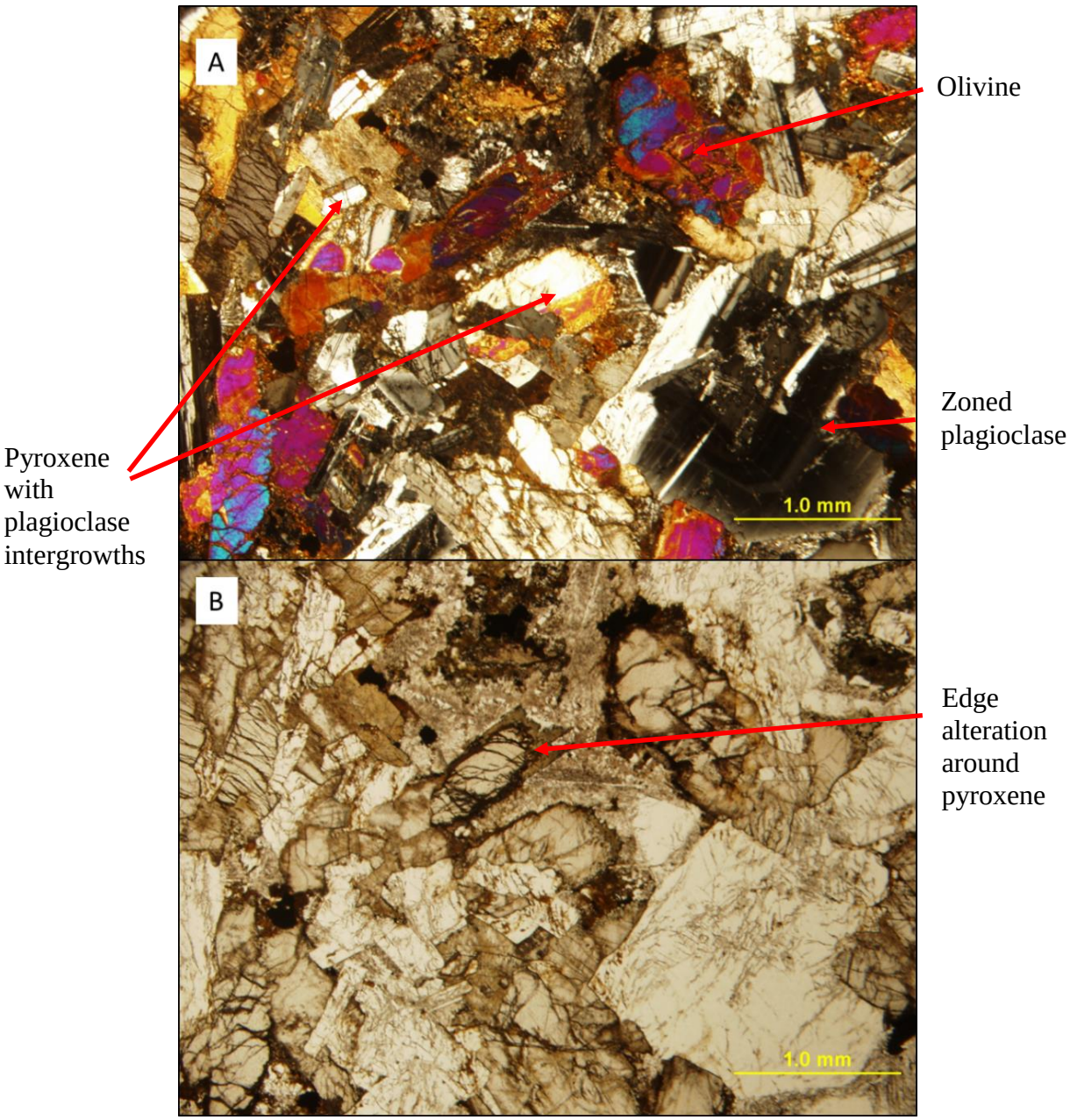

Figure 2.9b: Cobble erratic MG07 in cross polarised light (A), and plane polarised light (B).

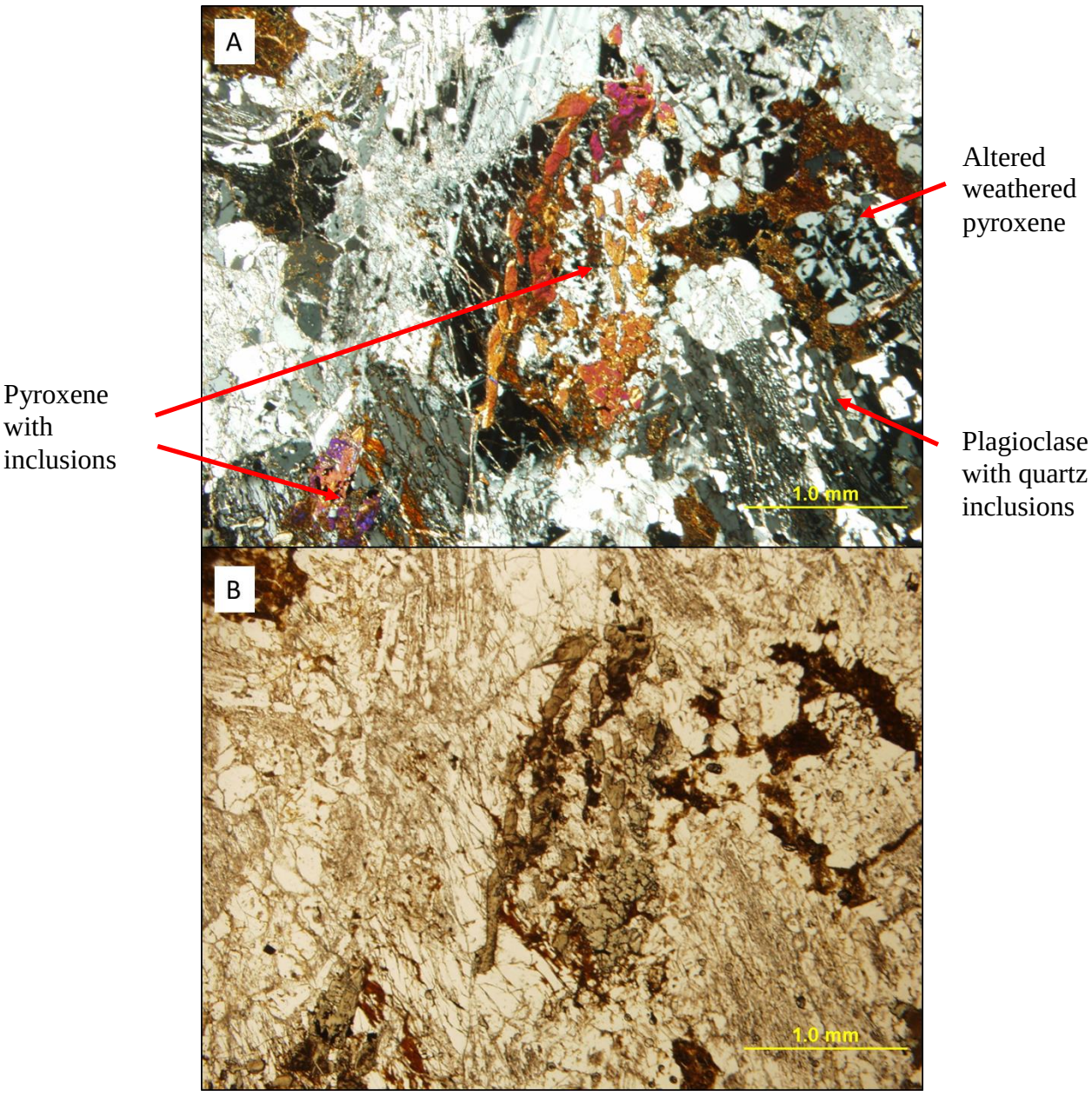

*Figure 2.*9c: Bedrock sample MG13-B in cross polarised light (A), and plane polarised light (B).

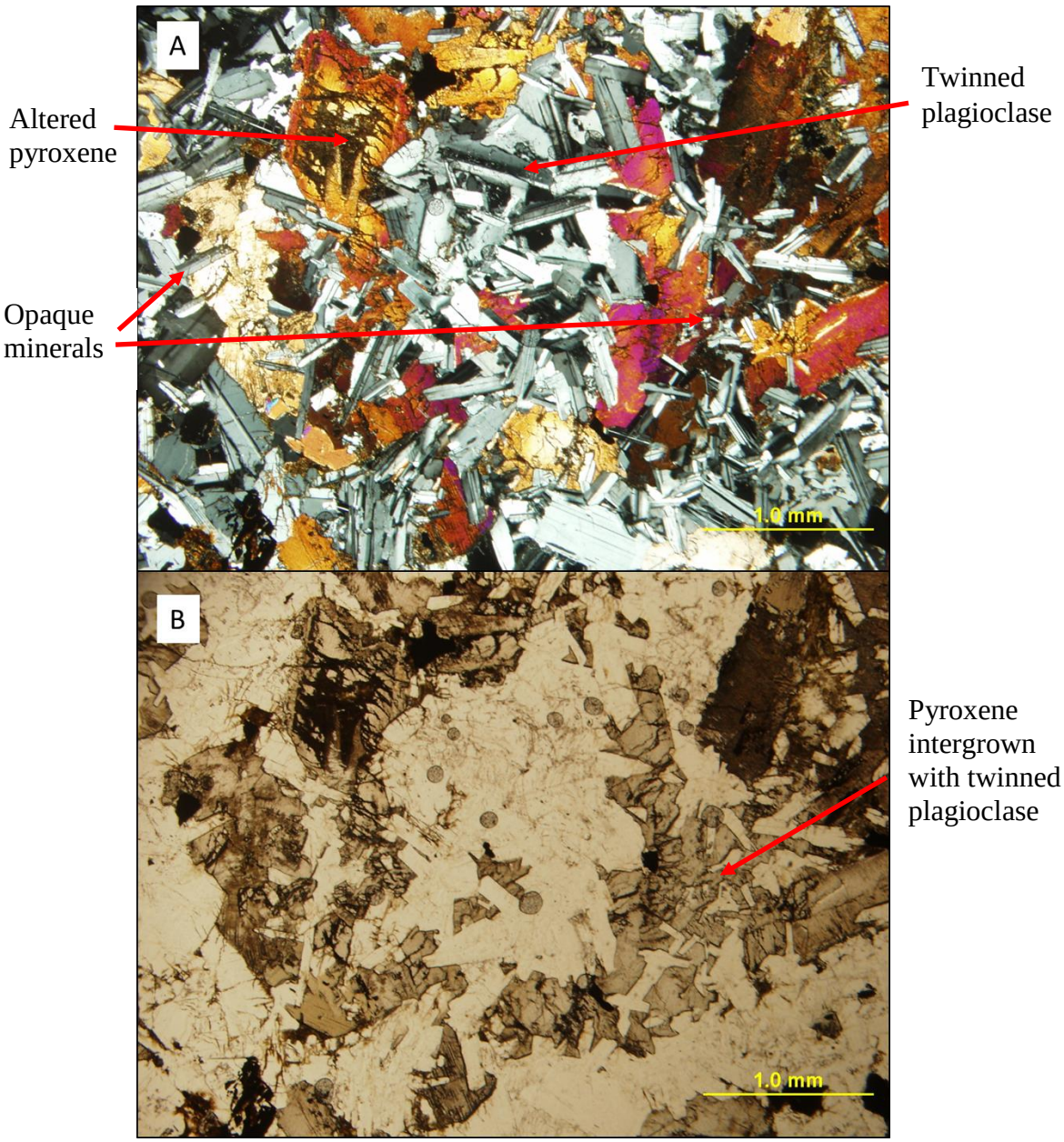

Figure 2.9d: Cobble erratic MG19 in cross polarised light (A), and plane polarised light (B).

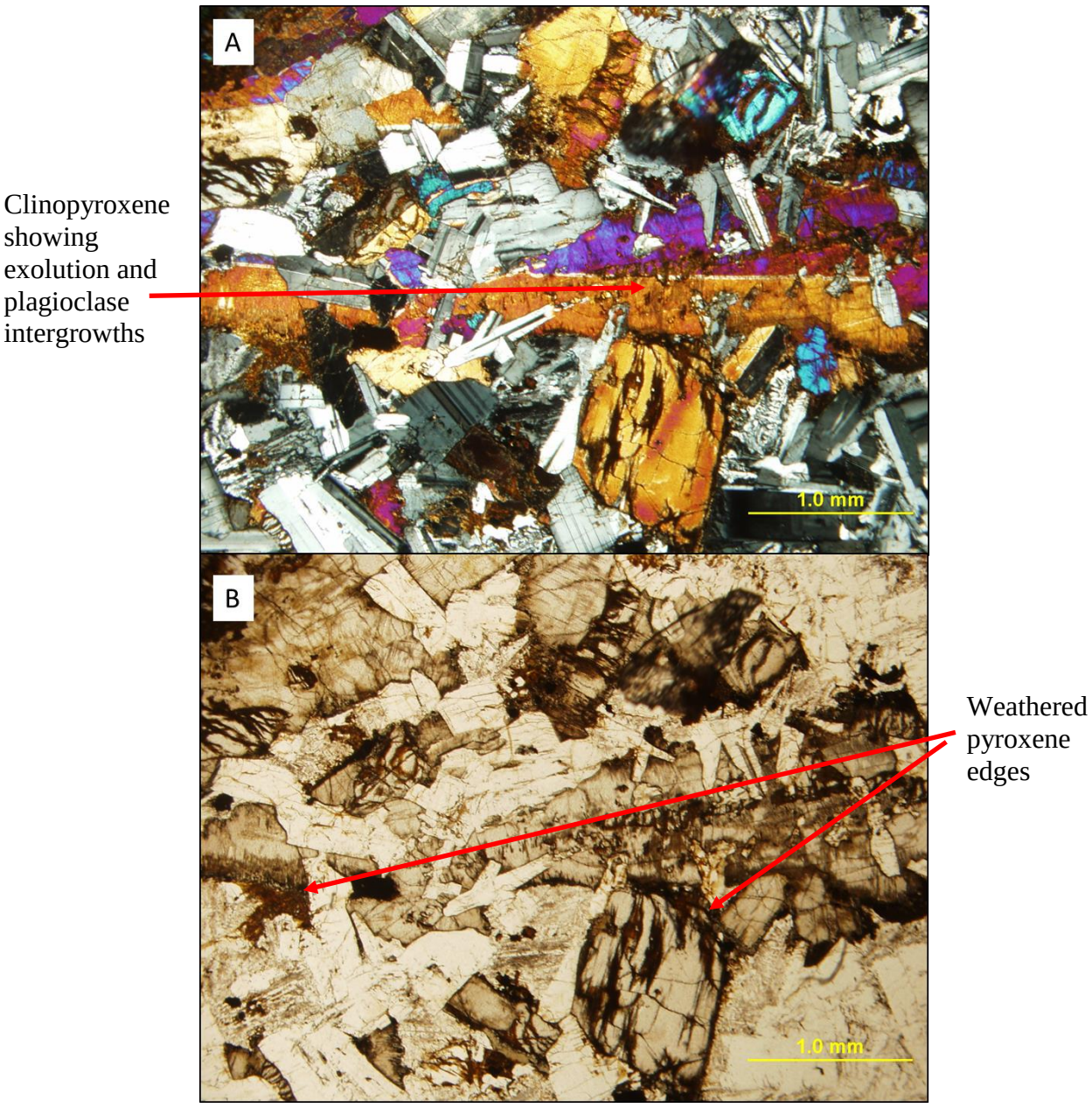

Figure 2.9e: Cobble erratic MG32 in cross polarised light (A), and plane polarised light (B).

2.1.2.3 Reason for site selection

Jones, *et al.* (submitted) have established a chronology of ice surface lowering since the LGM for the lower Mackay Glacier using the 'dipstick' method of exposure dating glacial deposits exposed at different elevations on the flank of a glacier. However, as mentioned in section 1.1.10, the absence of quartz-bearing rocks at Mount Gran has so far prevented obtaining a record of glacier response further upstream. Therefore, it provided a great opportunity to apply the decontamination method to extract *in situ* cosmogenic ^{10}Be from pyroxene, in order to further our understanding of Mackay Glacier thinning since the LGM.

2.2 Sample Collection

Samples were collected using a portable rock saw, a hammer and chisel. The Mount Ruapehu JC2 sample was collected from the flattest, highest point on a large boulder along the crest of the moraine to minimise the effects of shielding and weathering. The Murimotu samples were also collected from the top of boulders exposed at the top of the deposit, to minimise the chance of post-depositional re-orientation. The basement rock samples from Mount Gran were collected from striated bedrock surfaces that have been exposed to cosmogenic rays since ice retreat. As the concentration of cosmogenic nuclides decreases exponentially with depth into the rock, the top surface of the rock has the highest concentration. The samples collected with the handheld circular saw are approximately 2 cm thick as that is the maximum depth the saw blade can penetrate into the rock. The cobble erratics collected from

Mount Gran were taken as whole rocks, and the relevant top surface of the rock was later isolated in the laboratory at Victoria University of Wellington (VUW).

The location and elevation of each sample was recorded on a hand held GPS. Measurements of the surrounding topography were made using a geological compass and clinometer for topographic shielding corrections to be calculated. The samples were carefully selected to avoid boulders and cobbles that have undergone post-depositional reorientation, post-glacial weathering or burial by sediment or snow cover. These post depositional processes result in younger apparent exposure ages (Mackintosh, et al., 2007). Whereas, boulders that have previously been exposed would have inheritance and give a false older apparent age (Fabel, *et al.*, 2002; Putkonen & Swanson, 2003; Rinterknecht, *et al.*, 2006; Mackintosh, *et al.*, 2007).

2.3 Sample preparation

The cobble erratics collected on Mount Gran were cut at VUW using the Bianco diamond blade circular saw to allow only the top ~7 cm of the centre of the cobble to be used as the sample. The edges of the cobbles were avoided as they are more likely to be weathered. For this same reason, cracks in the cobbles were also avoided to lessen the contamination of meteoric ^{10}Be. Three of the eight cobbles used from Mount Gran were too large to cut under the Bianco Saw so the top 4 cm of the cobble was cut out using the hand held circular saw and chisel. All of the samples were then crushed in a Boyd jaw-crusher and sieved into the size fractions 125-250 µm and

250-500 µm. The samples were rinsed in distilled water to remove the fine particulate matter coating the grains and oven dried at 40 ºC.

Heavy liquid separation in Methylene Iodide of density 3.1 was carried out on both the 125-250 µm and 250-500 µm size fractions in order to separate the heavier pyroxenes from the lighter minerals in the sample. Once dried in the fumehood, the samples were examined under a binocular microscope to determine which size fraction yielded the purest pyroxenes. The 125-250 µm fraction had less foreign material attached to the individual pyroxene grains and displayed the cleanest separation and a yield of >95 % pyroxenes. Thus, this was the size fraction used for the remainder of the work. To achieve a cleaner separation the samples were then run through the Frantz magnetic separator to remove the non-magnetic minerals. Finally, a hand held magnet was run over the samples in order to remove the strongly magnetic minerals, i.e. magnetite.

The samples were crushed using an agate ringmill and an agate mortar and pestle to <90 µm in order to expose the weathering pits in the pyroxene. Blard, *et al.* (2008) proposes that this is a key step in the cleaning procedure as meteoric ^{10}Be is stored in weathering pits within the pyroxene grains, therefore by powdering the grains to <90 µm the weathering pits are exposed and the meteoric ^{10}Be can be easily leached out for accurate measurement of *in situ*. However the method has not been verified by other laboratories and requires testing before implementation.

2.4 Chemistry

2.4.1 Method development and leach verification

The basic leaching and dissolution steps, follow in sections 2.4.1.1 - 2.4.1.3. Section 2.4.1.4 discusses the outcome of the Blard, *et al.* (2008) decontamination procedure. Note that a simplified step-by-step version of the pyroxene preparation and leach and beryllium separation chemistry is supplied in appendix A.

2.4.1.1 Hydroxylammonium-chloride leach

Each sample was placed into a 190 ml Teflon beaker and precisely weighed. For each sample ~4 g material was processed, with the exception of the Mount Ruapehu sample (JC2). For JC2, ~16.4 g of material was processed as this was the original sample to test the Blard, *et al.*, (2008) decontamination method on. The samples were leached for 10 hours at 95 °C in 25 ml of a 0.04M solution of hydroxylammonium-chloride ($NH_2OH{\cdot}HCl$) in 25% acetic acid. This leach releases the grain absorbed meteoric ^{10}Be into an aqueous phase, without removing the *in situ* ^{10}Be, while also dissolving metallic oxides (Blard, *et al.*, 2008). The samples were then transferred into a centrifuge tube and centrifuged for 5 minutes at 3500 rpm. The supernate was decanted into a new centrifuge tube and the solids were rinsed three times with the same leaching solution. The supernatant for the test sample JC2 was collected with the purpose to measure its ^{10}Be concentration, but for the other samples this was discarded. The solid samples were transferred into their original Teflon beakers using Milli-Q deionised water (MQ) and dried down on a hotplate at 120 °C. The samples

were precisely weighed between steps to determine the mass of material dissolved during each leaching step.

2.4.1.2 Hydrochloric leach

The solid samples were transferred into 50 ml centrifuge tubes and 25 ml 1M hydrochloric (HCl) acid was added to each and placed on 'hot dog' rollers for 24 hours at 20 °C. Samples were centrifuged for 5 minutes at 3500 rpm and the supernate was decanted into a clean centrifuge tube. Each sample was rinsed three times using MQ with the supernate being collected in the same tube. Again, this supernate was collected for JC2 but for the other samples it was discarded. The solid samples were transferred back into the Teflon beakers using MQ and dried down on the hotplate before being precisely weighed.

2.4.1.3 Dissolution in hydrofluoric acid

The remaining solid sample was transferred into 50 ml centrifuge tubes and 35 ml of 4M hydrofluoric (HF) acid was added to each and placed on rollers for 24 hours at 20 °C. In order to dissolve the precipitated fluorides (Blard, *et al.*, 2008), 10 ml of concentrated 15M nitric (HNO_3) was added to each sample after the 24 hour dissolution and left for 20 minutes before being centrifuged and the leachate decanted. The samples were rinsed three times using MQ and then transferred back into the Teflon beakers and dried down on the hotplate. On the original Mount Ruapehu sample JC2, this dissolution step was repeated six times, and each leachate was collected in order to check the efficiency of the decontamination method. After the successive dissolution steps each sample was spiked with 750-1000 µL of a 375ppm ^{9}Be solution from GFZ Potsdam. For JC2, the ^{9}Be spike was added to each step. The remaining solid sample was bulk dissolved in concentrated HF.

2.4.1.4 Decontamination method verification

To test the Blard, *et al.* (2008) method we collected the supernate decanted after each leaching and dissolution step in order to measure the ^{10}Be concentration in each fraction. The mass dissolved in each step is summarised below in *table 2.1*. JC2-post HF1 was discarded due to contamination. JC2-post HF5 & 6 were combined to be measured together, however as a result of this the sample also had to be discarded as processing it would have been too time consuming because of the large number of cations. These samples were then run though the separation chemistry (outlined in section 2.4.2), the Be was precipitated, and the concentrations measured on the Accelerator Mass Spectrometer (AMS) at the Australian National University (ANU).

The concentrations demonstrate that ^{10}Be decreases with sequential leaching and dissolutions, indicating the removal of meteoric ^{10}Be from the pyroxenes until a plateau *in situ* concentration is reached (*figure 2.10*). The initial leaching in 0.04M $NH_2OH{\cdot}HCl$ yields a concentration of 202 ± 8 x 10^6 at. g^{-1}. This is much higher than the *in situ* concentration, corresponding to a high component of meteoric ^{10}Be that was released in this leach. Thus, this first leach was effective at removing meteoric ^{10}Be. The solution from the second leach in 1M HCl yielded a concentration of 19 ± 2 x 10^6 at. g^{-1}. This is not as high as the first leach, but nonetheless is higher than the *in situ* value. Blard, *et al.* (2008) suggest that this may reflect the release of meteoric ^{10}Be from the dissolution of secondary minerals in HCl, which is likely for metal oxide inclusions. The four HF dissolution steps that were measured have concentrations that are indistinguishable within error, with a mean of 10.9 ± 3 x 10^4 at. g^{-1}.

The levelling off of these concentrations during the HF dissolution steps suggests complete removal of meteoric ^{10}Be after the two leaches and 20% sample dissolution in HF. Based on this, the Murimotu and Mount Gran samples underwent the two initial leaches, and only one dissolution in HF to remove at least 20% of the mass, thereby removing the meteoric ^{10}Be, leaving only the *in situ* concentrations to be measured.

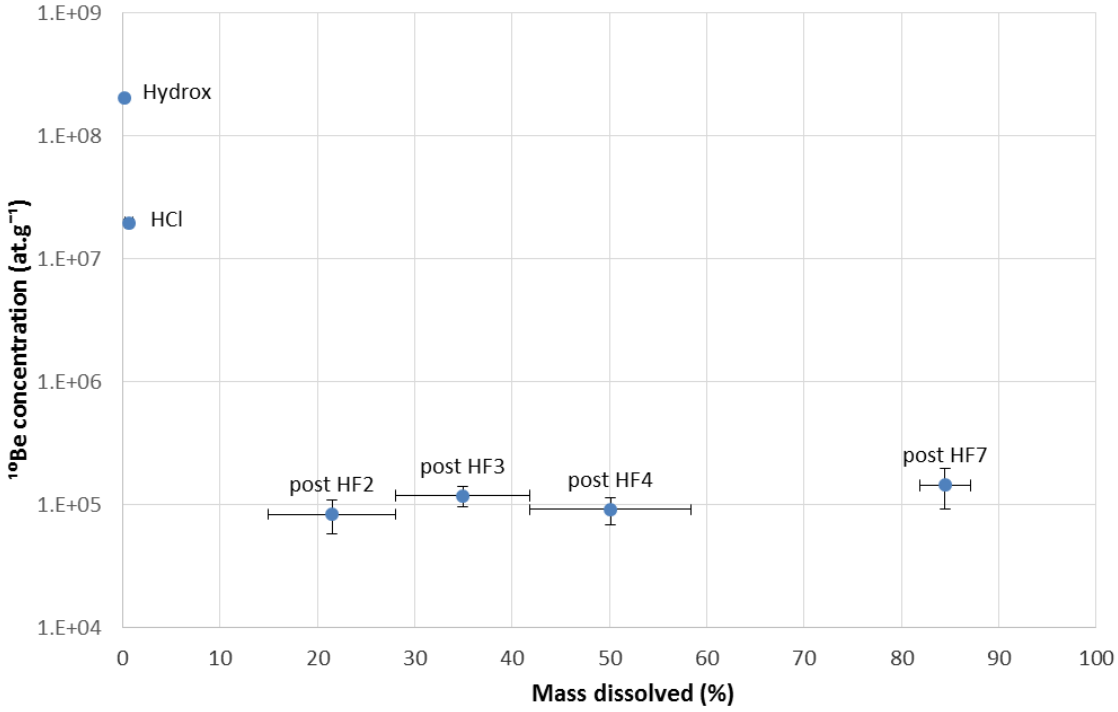

Figure 2.10: Evolution of the ^{10}Be concentration during the sequential leaching and dissolution steps applied to the JC2 pyroxenes. The ^{10}Be concentration decreases with mass dissolved, reaching a constant plateau value that implies a theoretical *in situ* ^{10}Be value. Note: the ^{10}Be concentration axis is logarithmically scaled.

Table 2.1: Sample data and ^{10}Be concentrations

Sample	Chemical treatment	Mass dissolved (g)	Mass dissolved (%)	^{10}Be concentration (10^4 at. g^{-1})	± (10^4 at. g^{-1})
JC2-hydrox	Leaching in 0.04M $NH_2OH \cdot HCl$	0.0445	0.27	20286.08	850.92
JC2-HCl	Leaching in 1M HCl	0.1317	1.07	1967.24	119.35
JC2-post HF1	Dissolution in 4M HF	2.2821	14.9	not measured	-
JC2-post HF2	Dissolution in 4M HF	2.1602	28.1	8.36	2.58
JC2-post HF3	Dissolution in 4M HF	2.2591	41.8	11.89	2.25
JC2-post HF4	Dissolution in 8M HF	2.7181	58.4	9.14	2.28
JC2-post HF5	Dissolution in 8M HF	2.511	73.6	not measured	-
JC2-post HF6	Dissolution in 8M HF	1.3565	81.9	not measured	-
JC2-post HF7	Dissolution in 8M HF	0.8499	87.0	14.43	5.18

2.4.2 Column calibration and precipitation

2.4.2.1 BeF_2 leach

One final leaching step was required before the samples could be run though the cation columns. In order to remove many unwanted cations, a BeF_2 leach (or water leach) was done. Once the samples are dried down after the dissolutions in HF, only a fluoride cake remains. The Be in the sample binds with F, forming a water soluble BeF_2. Therefore, by adding water to the fluoride cake, the BeF_2 is taken up in the water, leaving the insoluble elements remaining in the solids (Stone, 1998). Typically more than 90% of Na, Al, Mg, Ca, and Fe are retained as solids, while Be and Ti are completely soluble. For each sample, 10 ml of MQ was added to the fluoride cake, heated at 60 ^{0}C for 20 minutes, left to cool, and the supernate pipetted out into a 50 ml centrifuge tube. This was repeated three times to maximise BeF_2 yield. The remaining solids were discarded and the leachate was transferred back into the cleaned Teflon beakers and evaporated.

2.4.2.2 Cation chemistry – Fe columns

The samples were dissolved in 4-24 ml 6M HCl based on the amount of iron in the sample. Cation exchange chemistry was used to remove the Fe from the samples. The Fe was eluted using 15 ml Eichrom columns with 2 ml of Biorad AG1-X8 100-200 mesh anion resin. The Fe in the samples is retained in the resin in 6M HCl, while the remaining elements (including Be) are eluted and can be collected. The Fe is then eluted using 0.3M HCl and can be discarded. The Fe-removed samples were then evaporated on the hotplate.

2.4.2.3 Precipitation test

A precipitation step was trialled after this step. As Be precipitates out of solution at pH ~9, I firstly tested which other elements would also precipitate at pH ~9 that may also be found in pyroxene. 1 ml of ICP standard solutions of K, Ca, Na, Mg, Ti, Fe and Al were individually added to 10 ml centrifuge tubes containing 5 ml 1M HNO_3. To get the samples to pH ~9, 0.5 ml of concentrated (25%) ammonia was added to each and then shaken to precipitate elements, and then centrifuged. It was found that Ti, Fe, and Al precipitated at pH ~9, while K, Ca, Na and Mg did not (*see figure 2.11*). Therefore, by precipitating the sample at this stage the unwanted elements K, Ca, Na and Mg should be removed, reducing the amount of cations in the sample allowing a 'cleaner' sample to be run through the Be columns.

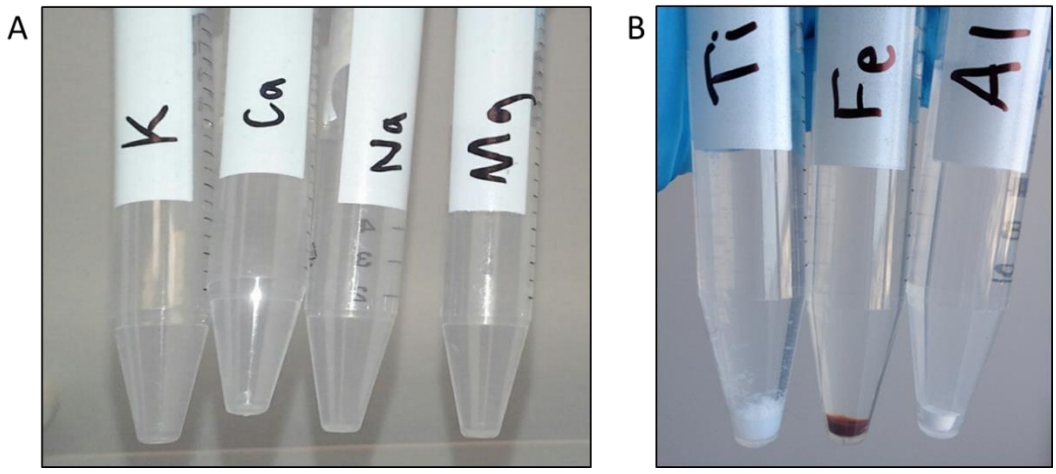

Figure 2.11: Precipitation of the elements at pH ~9. (A) No precipitation. (B) Precipitation at pH 9.

However, further testing discovered that this step decreased the Be yield in the remaining sample meaning that some of the Be in the sample did not precipitate and was discarded in the supernate along with K, Ca, Na and Mg. This was tested by taking aliquots of the supernates at this precipitation step and measuring their Be

concentration on an Agilent inductively coupled plasma – mass spectrometer (ICP-MS). During this precipitation step, the supernates of MG 02-B, 07, 15, and 32 were decanted into a clean centrifuge tube and an aliquot was taken (*figure 2.12*). It was noted at the time of precipitation that in some samples the precipitate did not completely settle during centrifugion after 15 minutes at 3500 rpm (see *figure 2.13A*), while in others it did (*figure 2.13B*). Additionally, ~1 g of crushed pyroxene from MG01, MG13-B and MG32 was dissolved in HF and spiked with ^{9}Be purely with the purpose to measure the change in Be concentration after this initial precipitation step. Aliquots were taken from both the supernate and precipitate (*figure 2.12).*

Measurements of these aliquots showed that Be was present in the supernate after this precipitation step in what appear to be higher concentrations than what remained in the precipitation. This suggests that not all of the Be was bound and precipitated as BeOH during the precipitation, potentially as a result of there being too many cations to bind and precipitate. Therefore, this initial precipitation step was abandoned in subsequent samples.

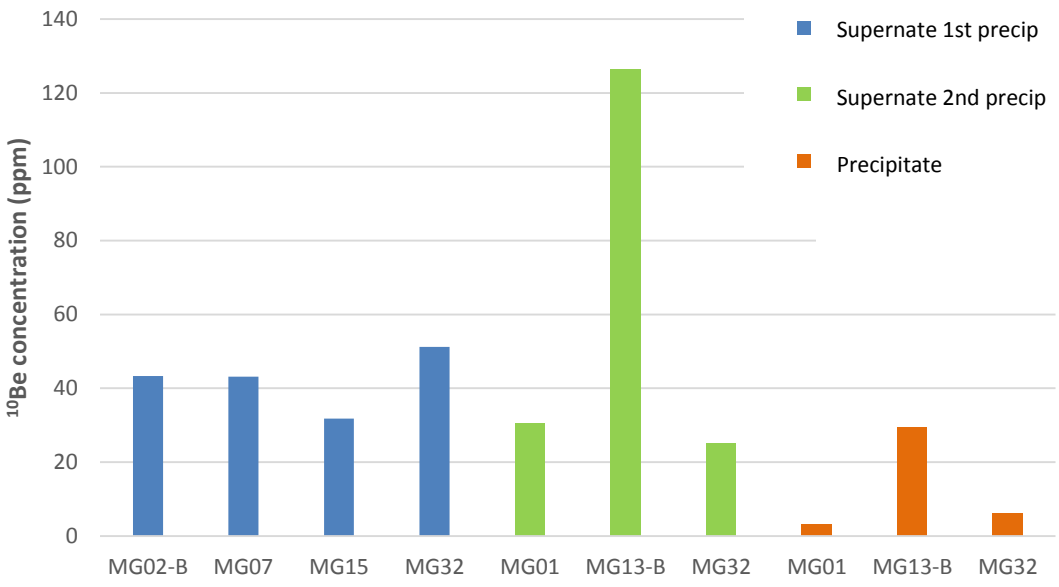

Figure 2.12: ^{10}Be concentration of the precipitates and their supernates measured on the ICP-MS after the initial precipitation step. Supernate 1st precip refers to the supernate of the samples that was collected during the initial precipitation test. Supernate 2nd precip refers to the additional ~1 g of Mt Gran pyroxenes that were dissolved with the purpose of measuring the Be concentration after this precipitation step. Precipitate refers to the precipitate formed during this precipitation step in the additional Mt Gran samples.

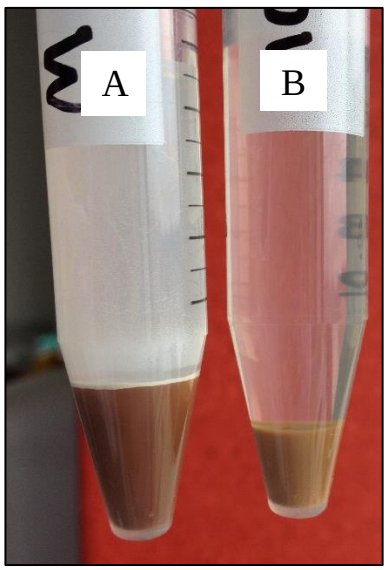

Figure 2.13: Examples of the initial precipitation step after centrifugion for 15 minutes at 3500 rpm. (A) MG01 shows that the precipitate did not completely settle during centrifugion. (B) MG13-B is an example that shows that the precipitate did settle out during centrifugion.

2.4.2.4 Column calibration experiments

As pyroxenes have more major cations than quartz, separation techniques used for cleaner quartz samples (Kohl & Nishiizumi, 1992) could not be applied. Column calibration experiments were performed in order to optimise the cation column chemistry for pyroxenes to achieve the best separation of Be. Three columns were tested with varying volumes of AG50-X8 resin and varying mesh sizes. Column 1 had 20 ml of 100-200 mesh resin; Column 2 had 5 ml of the finer 200-400 mesh resin; and column 3 had 5 ml of 100-200 mesh resin – this is the column normally used for Be separation in quartz. Every 5 ml (20 ml for the larger column 1, as quantities were multiplied by four) of acid that that was eluted from each column was collected and an aliquot measured on the Agilent ICP-MS to see when each element was eluted from the resin in order to see which column achieved the best separation of Be (*see figure 2.14*).

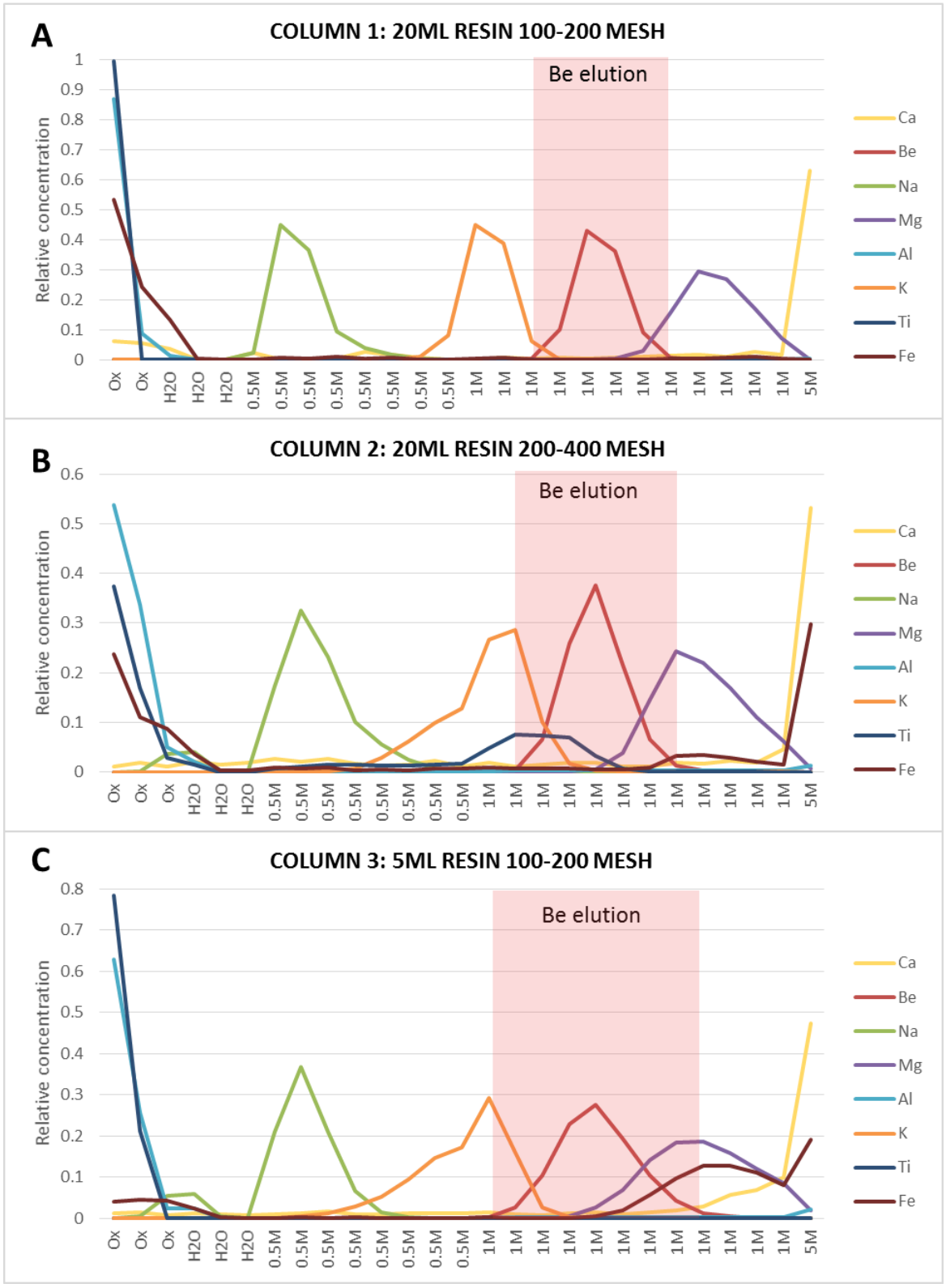

Figure 2.14: The elution of elements with HNO_3 in cation exchange resin. Ox = 0.4M oxalic acid; H2O = MQ deionised water; 0.5M, 1M and 5M = HNO_3. Be is retained in the resin in oxalic, H_2O and 0.5M HNO_3, but is eluted in 1M HNO_3 (shaded red area). Note that the volumes represented in each sample collected for column 1 are 20 ml, and are 5 ml for columns 2 and 3.

The Be was separated in each case, however column 1 that contained the larger volume of resin, achieved the best separation (*figure 2.14A*). There is significant overlap (contamination) with Mg for the coarser resin column 3 (*figure 2.14C*), and a slight overlap in the finer resin column 2 (*figure 2.14B*). Anomalous Fe appeared in the 1M fraction in both columns 2 and 3. Furthermore, Ti was eluted late in column 2, overlapping with the Be elution, which suggests incomplete conversion to oxalic. The oxalic acid was used to bind trivalent ions which would then allow less resin to be needed in the columns. The overlaps in columns 2 and 3 with Ti and Fe are problematic, as both of these elements precipitate at pH 9, as tested previously. Thus, column 1 (20 ml of 100-200 mesh resin) was used for Be separation in pyroxenes. As column 1 contains four times the volume of resin than the standard columns for quartz, the acid quantities were also scaled up by a factor of four to effectively elute Be.

2.4.2.5 Cation chemistry – Be columns

Once dried after the Fe columns, 40 ml of 0.4M oxalic acid was added to each sample and heated on the hotplate at 60 ºC until dissolved. They were then cooled and transferred to 50 ml centrifuge tubes and centrifuged for 5 minutes at 3500 rpm in preparation for the Be columns. The Be was eluted using 20 ml Biorad AG50-X8 100-200 mesh resin in 25 ml Eichrom columns, as tested to be the most effective column for Be isolation. The resin was cleaned using 5M HNO_3 and then conditioned using 0.4M oxalic in preparation for the sample to be loaded. The sample was added and Ti, Al and any remaining Fe were eluted with the oxalic. The oxalic was removed from the resin using MQ. Na and K were eluted using 0.5M HNO_3, then the Be was eluted using 1M HNO_3 and collected in a Teflon beaker. Some Mg is also eluted in the 1M HNO_3 however it does not precipitate at pH 9 so will not precipitate with the

Be (see *figure 2.11A)*. Finally Ca was eluted and the resin was cleaned using 5M HNO_3. The 1M HNO_3 collected in the Teflon beaker was then evaporated on a hotplate and transferred to a 15 ml centrifuge tube using 10 ml 1M HNO_3.

2.4.2.6 Be precipitation

~1 ml of concentrated ammonia was added to each sample to take it to pH ~9, then the sample was shaken well until BeOH formed. The BeOH appeared as oily white flecks in the liquid. Once centrifuged for 5 minutes at 3500 rpm, it segregated as a clear white gel in the bottom of the centrifuge tube. The supernate was decanted and the precipitate was rinsed three times in MQ. The precipitate was then re-dissolved in 0.3 ml of 5M HNO_3 and transferred into quartz crucibles where they were dried down on a hotplate before being oxidised over a Bunsen burner flame, leaving BeO remaining.

2.4.2.7 Accelerator Mass Spectrometer

The BeO was sent to the Australian National University (ANU) where it was mixed with niobium powder (ratio of ~1 mg BeO: ~4 mg Nb), and compressed into a drill hole in a copper holder (Stephen Tims, pers. comm.). The $^{10}Be/^{9}Be$ ratios were measured on a 14UD tandem accelerator mass spectrometer (AMS) (http://physics.anu.edu.au/nuclear/research/ams/). Measured ratios were calibrated against NIST (National Institute of Standards and Technologies) standard, with a $^{10}Be/^{9}Be$ ratio assumed to be 3.00×10^{-11}. Samples were also corrected for laboratory blanks. Three batches of samples were measured with an average blank $^{10}Be/^{9}Be$ ratio of 2.0×10^{-15}. The blank corrected $^{10}Be/^{9}Be$ ratios were then corrected against an internal standard, and converted into a ^{10}Be concentration (in atoms g^{-1}).

Chapter Three: Results

This chapter is organised as follows; discussion of the ^{10}Be concentration dataset and associated errors in section 3.1. The production rates determined for ^{10}Be in pyroxene at the Murimotu calibration site, and theoretically calculated production rates are reviewed in section 3.2. This is followed by the application of ^{10}Be in pyroxene as a chronometer for surface exposure dating of the Mount Gran samples in section 3.3. Lastly, the chapter is summarised in section 3.4.

3.1 ^{10}Be measurement and concentrations

The measured ^{10}Be/^{9}Be ratios, the weight of ^{9}Be carrier added, and the blank-corrected ^{10}Be concentrations are shown in *tables 3.1 and 3.2*. For sample JC2 ~16.4, grams of pyroxene was initially dissolved. Each leaching fraction was collected, and the remaining solid sample was precisely weighed between each step. The mass dissolved ranged between 0.04 g and 2.7 g for each leach. For the remaining Murimotu and Mount Gran samples, ~4 grams of pyroxene was initially dissolved. Based on the leaching experiment, the material dissolved during the initial leaching and HF dissolution step was discarded as it contained meteoric ^{10}Be. The remaining sample was completely dissolved and its ^{10}Be concentration measured. The mass dissolved for these samples ranged between 0.7 g and 2.8 g (see *tables 3.1 and 3.2*). As a result of the small amount of sample dissolved, the measured ^{10}Be/^{9}Be ratios are

low and therefore have errors up to 33%. Once the sample had been blank-corrected, the total error on the ^{10}Be concentration ranged between 4% (in JC2 hyrdox sample) up to 53% (in MG01).

Table 3.1: $^{10}Be/^{9}Be$ ratios and blank corrected ^{10}Be concentrations for JC2 and the Murimotu samples.

Sample	$^{10}Be/^{9}Be$ ratios	Error on $^{10}Be/^{9}Be$ ratio (%)	Pyroxene weight dissolved (g)	Weight ^{9}Be added by Carrier (g)	^{9}Be added by Carrier (atoms)	^{10}Be Sample conc (atoms g^{-1})	^{10}Be Sample conc Error (atoms g^{-1})	Total error (%)
JC2- leach								
hydrox	3.27E-13	4.18	0.04	4.14E-04	2.77E+19	2.03E+08	8.51E+06	4.19
HCl	9.45E-14	5.98	0.13	4.14E-04	2.77E+19	1.97E+07	1.19E+06	6.07
post HF2	7.46E-15	26.05	2.16	4.14E-04	2.77E+19	8.36E+04	2.58E+04	30.90
post HF3	1.07E-14	16.50	2.26	4.14E-04	2.76E+19	1.19E+05	2.25E+04	18.92
post HF4	9.93E-15	22.03	2.72	4.13E-04	2.76E+19	9.14E+04	2.29E+04	25.05
post HF7	5.38E-15	27.90	0.85	4.13E-04	2.76E+19	1.44E+05	5.18E+04	35.89
Murimotu								
MM01	7.67E-15	14.63	2.76	3.72E-04	2.49E+19	5.12E+04	1.66E+04	32.42
MM02	1.18E-14	15.89	2.83	3.71E-04	2.48E+19	8.60E+04	2.08E+04	24.23
MM03	1.43E-14	11.13	2.35	3.71E-04	2.48E+19	1.30E+05	2.28E+04	17.57
MM04	7.61E-15	14.81	2.24	3.71E-04	2.48E+19	6.21E+04	2.04E+04	32.85

Table 3.2: $^{10}Be/^{9}Be$ ratios and blank corrected ^{10}Be concentrations for the Mount Gran samples.

Sample	$^{10}Be/^{9}Be$ ratios	Error on $^{10}Be/^{9}Be$ ratio (%)	Pyroxene weight dissolved (g)	Weight ^{9}Be added by Carrier (g)	^{9}Be added by Carrier (atoms)	^{10}Be Sample conc (atoms g^{-1})	^{10}Be Sample conc Error (atoms g^{-1})	Total error (%)
Mount Gran								
MG01	7.43E-15	33.47	1.29	3.10E-04	2.07E+19	8.72E+04	4.63E+04	53.08
MG02-B	1.88E-14	18.81	1.20	3.11E-04	2.08E+19	2.91E+05	6.62E+04	22.77
MG07	2.51E-14	21.53	1.23	3.11E-04	2.08E+19	3.91E+05	9.48E+04	24.23
MG08-B	3.49E-14	17.66	1.28	3.24E-04	2.17E+19	5.55E+05	1.07E+05	19.25
MG12	7.17E-15	21.07	1.09	3.73E-04	2.49E+19	1.18E+05	4.79E+04	40.57
MG13-B	6.22E-14	30.30	1.61	3.11E-04	2.08E+19	7.79E+05	2.44E+05	31.40
MG15	1.55E-14	19.13	1.26	3.10E-04	2.07E+19	2.24E+05	5.47E+04	24.45
MG19	1.01E-14	33.47	1.26	3.10E-04	2.07E+19	1.33E+05	6.05E+04	45.44
MG22	1.08E-14	23.76	1.46	3.09E-04	2.07E+19	1.25E+05	4.18E+04	33.56
MG30	1.23E-14	16.93	1.49	3.72E-04	2.49E+19	1.73E+05	4.26E+04	24.64
MG32	1.53E-14	27.90	1.66	3.10E-04	2.07E+19	1.67E+05	5.65E+04	33.90
MGW01	1.80E-14	13.47	0.73	3.71E-04	2.48E+19	5.41E+05	9.56E+04	17.68
MGW03	1.59E-14	19.13	1.00	3.71E-04	2.48E+19	3.45E+05	8.39E+04	24.28
MGW04	1.78E-14	14.60	1.20	3.72E-04	2.48E+19	3.28E+05	6.18E+04	18.86
MGW05	2.47E-14	12.58	1.45	3.72E-04	2.48E+19	3.89E+05	5.88E+04	15.12

3.2 Production rate calibration

In order to calculate accurate exposure ages, the production rate of the cosmogenic nuclide in the mineral of interest must be known (Cerling & Craig, 1994). As extracting *in situ* cosmogenic ^{10}Be from pyroxene is a relatively novel approach, the production rates are not well known. Production rates vary depending on the composition of the mineral as cosmogenic nuclides are produced at different rates in various target elements. Thus, we expect the production rate of ^{10}Be in pyroxene (P10px) to differ from the production rate of ^{10}Be in quartz (P10qtz). I have calculated P10px from cross-calibrations against cosmogenic ^{3}He and radiocarbon from the Murimotu debris avalanche in the central North Island. I have also calculated the theoretical P10px based on the composition of the Murimotu pyroxenes. These calculated P10px values are reported below.

3.2.1 ^{10}Be production rate in pyroxene - ^{3}He cross-calibration

The ^{3}He concentration in pyroxene from samples within the Murimotu debris avalanche was independently determined by Eaves, *et al.* (2015). This allows a production rate to be calculated, via direct cross-calibration, for ^{10}Be in pyroxene. As the Murimotu debris avalanche has a well-constrained radiocarbon age, it is able to be used as an independently dated production rate calibration site for cosmogenic nuclides. Eaves, *et al.* (2015) have measured the cosmogenic ^{3}He concentration in the Murimotu pyroxenes in order to establish a production rate calibration site for this nuclide in New Zealand. I have measured the *in situ* ^{10}Be concentration in the same

pyroxene (using the new decontamination procedure), which allows determination of the P10px from direct cross-calibration with ^{3}He. Provided the ^{3}He concentration (*N3px*), and the production rate of ^{3}He at sea-level and high-latitude (P_3SLHL) are known, the production rate of ^{10}Be at SLHL ($P_{10}SLHL$) can be calculated by Taylor series expansion of equations 1 and 2, respectively, in Blard, *et al.* (2008):

$$N_{10}SLHL = \frac{f\ P_{10}\ t}{1 + t\left(\frac{\rho\varepsilon}{\Lambda} + \lambda_{10}\right)} \tag{3.1 A}$$

$$N_3SLHL = \frac{f\ P_3\ t}{1 + t\left(\frac{\rho\varepsilon}{\Lambda}\right)} \tag{3.1 B}$$

Where f is a scaling factor, t is exposure time, ρ is density, ε is erosion, Λ is attenuation path length, and λ_{10} is the decay constant of ^{10}Be, 5.17 x 10^{-7} a^{-1} (Chmeleff, *et al.*, 2010; Korschinek, *et al.*, 2010). The above equations can be solved for N_3/N_{10} if ε = 0:

$$\frac{N_3px}{N_{10}px} = \frac{P_3SLHL}{P_{10}SLHL}\ (1 + \lambda_{10}\ t) \tag{3.1 C}$$

Solve for $P_{10}SLHL$ if ε = 0:

$$P_{10}SLHL = P_3SLHL\left(\frac{N_{10}px}{N_3px}\right)\ (1 + \lambda_{10}\ t) \tag{3.1 D}$$

The propagated error in the ^{3}He cross-calibrated P10px is calculated using the simple error propagation equation for standard deviation, where A, B, and C are the variables with standard deviation σ:

$$\sigma f \approx f \sqrt{\left(\frac{\sigma_A}{A}\right)^2 + \left(\frac{\sigma_B}{B}\right)^2 + \left(\frac{\sigma_C}{C}\right)^2} \quad (3.2)$$

The measured and normalised nuclide concentrations of ^{10}Be and ^{3}He are shown in *table 3.3*, where the ^{3}He concentrations are provided by Eaves, *et al.* (2015). Sample MM-12-03 was collected in three segments off the top of the boulder. For the ^{10}Be analysis section MM-12-03-c (~2 cm thick on average) was used, and for the ^{3}He nuclide analysis section MM-12-03-b (~10 cm thick) was used (*figure 3.1*). As these sections had different thicknesses, both nuclides had to be normalised to remove this factor. The *in situ* ^{10}Be concentration in the four Murimotu samples range between 5.24 ± 1.66 and 13.20 ± 2.28 x 10^{4} at. g^{-1}. The concentration in MM-12-03 is higher, but just within error of the next highest concentration. Contrastingly, the ^{3}He concentration in this sample is lower than the ^{3}He concentrations measured in the remaining three samples. Eaves, *et al.* (2015) considered this sample a potential outlier, and thus determined production rates for ^{3}He for both N=4, and N=3 when excluding MM-12-03. The production rates determined for ^{10}Be in pyroxene from cross-calibration with ^{3}He and radiocarbon at the Murimotu calibration site are also calculated for both N=4, and N=3.

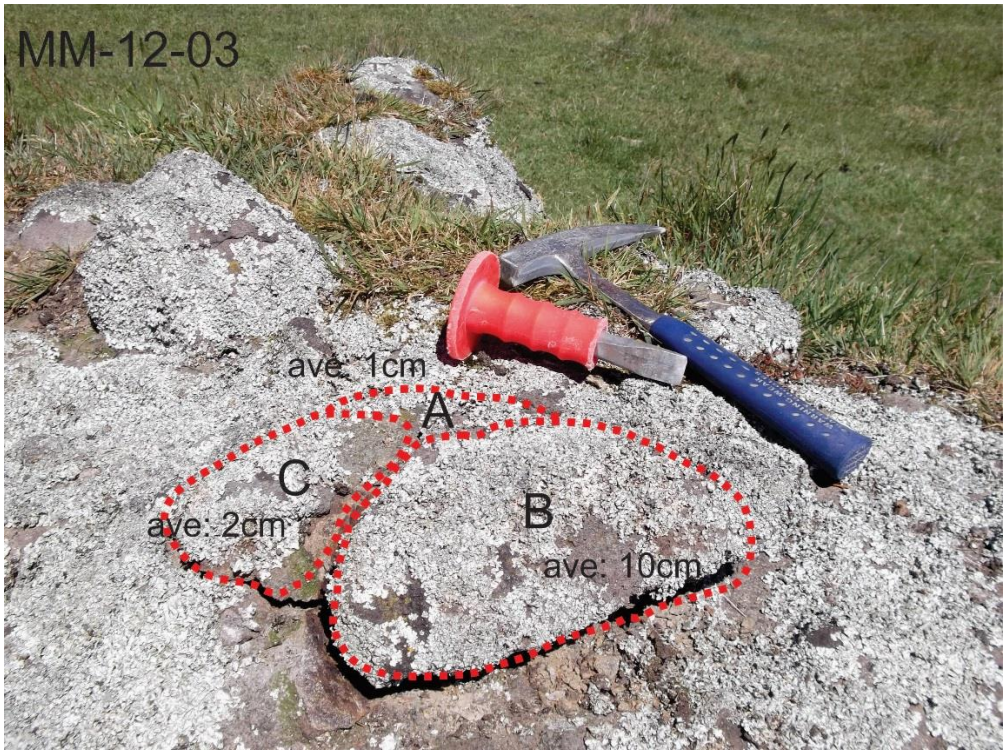

Figure 3.1: Sampled surface of MM-12-03. Section B was used for ^{3}He analysis, and section C was used for ^{10}Be analysis. Section A was not analysed. Photo supplied and modified by S. Eaves.

The ^{3}He cross-calibrated production rates calculated using equation 3.1 are presented in *table 3.4.* The production rate of ^{3}He in pyroxene is provided by Goehring, *et al.* (2010). The Goehring, *et al.* (2010) production rate was used as it is better constrained than the Eaves, *et al.* (2015) production rate, however the production rates are indistinguishable. P10px for the Murimotu samples were calculated using each of the five commonly applied scaling schemes (see table 1.1). The individual average production rates (for all scaling schemes averaged) for samples MM-12-01, -02 and -04 range between 2.6 ± 0.8 and 4.9 ± 1.2 atoms g^{-1} yr^{-1}. While the average production rate for sample MM-12-03 is 8.0 ± 1.5 atoms g^{-1} yr^{-1}, which is much higher than the average for the other three samples. The average of all four samples (N=4) provides a production rate of 4.6 ± 2.5 atoms g^{-1} yr^{-1}. If sample MM-12-03 is removed from the dataset (N=3) the production rates decrease to an average of 3.5 ±

1.2 atoms g^{-1} yr^{-1}. However, both of these production rates are indistinguishable within 1σ error. Note that all references to production rates in this thesis are scaled to sea-level, high latitude (SLHL).

3.2.2 $^{3}He/^{10}Be$ ratios

In addition to the ^{3}He cross-calibration of P10px, the ^{3}He concentration can also be used to test the ratio of ^{3}He to ^{10}Be in the samples. $^{3}He/^{10}Be$ ratios are important as they should stay a constant value even if absolute production rate values change. The ratio of ^{3}He in pyroxene (from Eaves, *et al.*, 2015) to ^{10}Be in quartz (from Putnam, *et al.* 2010) in New Zealand ranges from 32.1 ± 3.2 to 33.0 ± 3.4 dependant on the scaling scheme applied (Eaves, *et al.* 2015). The ratio of the ^{3}He concentration in the Murimotu pyroxene to the ^{10}Be concentration measured in the same pyroxene ranges between 16.3 ± 2.9 and 51.0 ± 16.3. The ratio of 16.3 ± 2.9 is from sample MM-12-03 which has a high ^{10}Be concentration but a low ^{3}He concentration (*table 3.3*). The average $^{3}He/^{10}Be$ ratio from the Murimotu samples is 34.5 ± 9.9 (N=4). If sample MM-12-03 is excluded (N=3) the ratio increases to 40.6 ± 12.3. For comparison, Eaves, *et al.* (2015) compared the ratio of ^{3}He measured in the Murimotu pyroxenes to the ^{10}Be concentration measured in quartz by Putnam, *et al.* (2009) in the Southern Alps of New Zealand, determining a $^{3}He/^{10}Be$ average ratio of 32.5 ± 3.3. This will be further discussed in section 4.2.4.

Table 3.3: Measured and normalised ^{10}Be concentration and ^{3}He concentrations.

Sample	Shielding scaling factor	Thickness scaling factor	Measured ^{10}Be concentration (10^4 at. g^{-1})	Normalised ^{10}Be concentration[a] (10^4 at. g^{-1}) ± 1σ	^{10}Be conc. error %	Measured ^{3}He concentration[b] (10^6 at. g^{-1})	Normalised ^{3}He concentration[a] (10^4 at. g^{-1}) ± 1σ	^{3}He/^{10}Be ratio	^{3}He/^{10}Be std error
MM-12-01	0.999	0.979	5.12	5.24 ± 1.66	31.7	2.56	261.25 ± 8.61	51.0	16.3
MM-12-02	0.999	0.971	8.60	8.86 ± 2.08	23.5	2.29	236.33 ± 8.02	27.5	6.5
MM-12-03-c	0.999	0.983	12.96	13.20 ± 2.28	17.3	-	-	-	-
MM-12-03-b	0.999	0.920	-	-	-	1.94	211.55 ± 7.65	16.3	2.9
MM-12-04	0.999	0.983	6.21	6.33 ± 2.04	32.3	2.64	268.96 ± 7.57	43.3	14.0

[a] The samples have been normalised to account for the difference in thickness of two different sections of sample used for MM-12-03.

[b] He-3 concentrations provided by Eaves, *et al.* (2015).

Table 3.4: Production rates for ^{10}Be in pyroxene (atoms g^{-1} yr^{-1}) ± 1σ calculated from cross-calibration with ^{3}He in pyroxene from samples within the Murimotu debris avalanche. P10px (SLHL) calculated using equation 3.1. Errors on P10px calculated using equation 3.2.

Samples	**Scaling scheme**					
	St	De	Du	Li	Lm	Average[b]
MM-12-01	2.5 ± 0.8	2.6 ± 0.8	2.6 ± 0.8	2.8 ± 0.9	2.4 ± 0.8	2.6 ± 0.8
MM-12-02	4.5 ± 1.2	4.8 ± 1.2	5.2 ± 1.3	5.2 ± 1.2	4.5 ± 1.1	4.9 ± 1.2
MM-12-03	7.5 ± 1.5	8.1 + 1.5	8.1 ± 1.5	8.6 ± 1.6	7.5 ± 1.5	8.0 ± 1.5
MM-12-04	2.8 ± 1.1	3.0 ± 1.0	3.1 ± 1.0	3.3 ± 1.1	2.8 ± 0.9	3.1 ± 1.0
Arithmetic mean (N=4)	4.6 ± 2.3	4.6 ± 2.3	4.7 ± 2.5	5.0 ± 2.7	4.3 ± 2.3	4.6 ± 2.5
Arithmetic mean MM-12-03 removed (N=3)	3.5 ± 1.1	3.5 ± 1.2	3.5 ± 1.4	3.7± 1.3	3.3 ± 1.1	3.5 ± 1.2
Goehring, *et al.* (2010) reference P3px (SLHL)[a]	124 ± 9.2	128 ± 6.4	129 ± 7.8	137 ± 5.7	119 ± 9.9	127 ± 7.8

[a] He-3 production rate in pyroxene provided by Goehring, *et al*. (2010).

[b] Averaged productions rates for each sample and for scaling scheme also shown.

N.B. Scaling schemes defined in table 1.1 (pg. 16) (Balco, *et al*., 2008).

3.2.3 ^{10}Be production rate in pyroxene - radiocarbon cross-calibration

Production rates for ^{10}Be in pyroxene were also calculated using direct cross-calibration with an independent radiocarbon age for the Murimotu debris avalanche (P10px-radiocarbon). The radiocarbon age used for the cross-calibration is 10597 ± 110 yrs (Eaves, *et al.*, 2015). A P10px-radiocarbon was generated using the CRONUS-Earth online production rate calculator, version 2.2. (http://hess.ess.washington.edu/math/al_be_v22/al_be_calibrate_v22.php). The production rates were determined independently for each sample, for all samples (N=4), and with MM-12-03 excluded (N=3) (*table 3.5).* The production rate for MM-12-03 could not be calculated independently and is left blank in the table. The P10px-radiocarbon (N=4) ranged between 3.4 ± 0.8 and 3.9 ± 0.9 atoms g^{-1} yr^{-1}, with an average of 3.6 ± 0.9 atoms g^{-1} yr^{-1}. However, if sample MM-12-03 is excluded (N=3), the production rates decreased to range between 2.8 ± 0.7 and 3.2 ± 0.8 atoms g^{-1} yr^{-1} with an average of 3.0 ± 0.8 atoms g^{-1} yr^{-1}. As with the ^{3}He cross-calibrated ^{10}Be production rate, these values are the same within uncertainties.

Table 3.5: Production rates for ^{10}Be in pyroxene (atoms g^{-1} yr^{-1}) ± 1σ calculated from cross-calibration with the radiocarbon age of the Murimotu debris avalanche.

Samples	**Scaling scheme**					
	St	De	Du	Li	Lm	Average
MM-12-01	2.3 ± 0.8	2.3 ± 0.8	2.3 ± 0.8	2.4 ± 0.9	2.2 ± 0.9	2.3 ± 0.8
MM-12-02	4.1 ± 1.0	4.2 ± 1.0	4.1 ± 1.0	4.5 ± 1.1	4.0 ± 1.0	4.2 ± 1.0
MM-12-03	-	-	-	-	-	-
MM-12-04	2.9 ± 1.0	2.9 ± 1.0	2.9 ± 1.0	3.1 ± 1.0	2.8 ± 1.0	2.9 ± 1.0
All 4 samples (N=4)	3.5 ± 0.8	3.6 ± 0.9	3.5 ± 0.8	3.9 ± 0.9	3.4 ± 0.8	3.6 ± 0.9
Sample MM-12-03 excluded (N=3)	2.9 ± 0.7	3.0 ± 0.8	2.9 ± 0.7	3.2± 0.8	2.8 ± 0.7	3.0 ± 0.8

Production rates calculated using the CRONUS-Earth online production rate calculator. Radiocarbon age used for calculation is 10597 ± 110 yr (Eaves, *et al.*, 2015).

3.2.4 Theoretical ^{10}Be production rate

In addition to the ^{3}He and radiocarbon cross-calibrated P10px, theoretical production rates for ^{10}Be in pyroxene were determined based on the composition of the pyroxene. The production rate in a target element is proportional to the cosmic ray flux, the cross-section of the target element, and the abundance of the target element in the target mineral (Gosse & Phillips, 2001). The major element composition of the Murimotu pyroxenes were measured by Eaves, *et al.* (2015) by solution ICP-MS to determine the abundance of each target element. These major element concentrations (in weight percent, wt.%) are shown in *table 3.6.* The production rates of ^{10}Be in target elements have been derived using model calculations by Masarik (2002) and have been experimentally adjusted by Kober, *et al.* (2005). The elemental production rates are based on the cosmic ray flux from Masarik & Beer (1999), and the cross section of the target element, which have been obtained using irradiation experiments by Leya, *et al.* (2000). The elemental ^{10}Be production rates for both Masarik (2002) and Kober, *et al.* (2005) are included in *table 3.6*. The equation to calculate theoretical P10px, dependant on the composition of the mineral, is modified from Fenton, *et al.* (2009) as:

$$TP10m = \frac{(X_{Si} * P10_{Si}) + (X_O * P10_O) + (X_i * P10_i)}{100} \quad (3.3)$$

Where *TP10m* is the theoretical production rate of ^{10}Be in the mineral of interest; X_{Si} and X_O are the weight percent of Si and O, respectively, and X_i is the weight percent of element i (i.e. Al, Ca, Fe, Mg, etc.); $P10_{Si,}$ and $P10_O$ are the production rates of ^{10}Be in element Si and O respectively, while $P10_i$ is the production rate in element i.

Table 3.6: Theoretical simulated SLHL ^{10}Be elemental production rates from Kober, *et al.* (2005) and Masarik (2002) and major element compositions (wt.%) of the Murimotu pyroxene.

	Al	Ca	Fe	Mg	Mn	Na	Ti	Si[a]	O[a]
Elemental P10 px (at. g^{-1} yr^{-1})									
Kober (2005)	1.61	1.21	1.86	1.93	-	-	-	3.28	6.54
Masarik (2002)	1.03	-	0.35	1.74	-	-	-	0.89	9.82
Sample concentration wt.%									
MM-12-01	0.72	1.24	16.40	14.08	0.36	0.03	0.20	23.46	42.74
MM-12-02	1.02	1.28	14.37	15.88	0.19	0.03	0.08	22.93	43.15
MM-12-03	0.77	1.89	16.05	13.93	0.35	0.04	0.10	23.33	42.69
MM-12-04	0.72	1.47	16.93	14.56	0.36	0.04	0.22	22.58	42.33

Note '–' indicates the elemental ^{10}Be production rate is unknown.

[a] Si and O wt.% estimated by calculating all measured elements as oxides (wt.%) and subtracting this from the total 100 wt.%, leaving SiO_2 which can then be separated to determine the wt.% of Si and O in SiO_2.

Theoretical P10px were determined using both the Masarik (2002) elemental ^{10}Be production rates, and also the updated Kober, *et al.* (2005) values. These are shown in *table 3.7.* The theoretical production rates for ^{10}Be in pyroxene using the Kober, *et al.* (2005) elemental production rate values range between 4.13 and 4.18 atoms g^{-1} yr^{-1} with an average of 4.16 atoms g^{-1} yr^{-1}. Errors in these measurements are not shown as the elemental production rates have unknown uncertainties. The Masarik (2002) elemental production rate values yield higher production rates ranging between 4.58 and 4.67 atoms g^{-1} yr^{-1} with an average of 4.62 atoms g^{-1} yr^{-1}.

As the absolute precision of the elemental production rates are unknown, the theoretical production rates for ^{10}Be in quartz (P10qtz) were also calculated in order to calculate a percent reduction between the theoretical production rate in quartz and pyroxene. The Kober, *et al.* (2005) values produce an average theoretical P10qtz of 5.02 atoms g^{-1} yr^{-1}, whereas the Masarik (2002) values yield a production rate average of 5.64 atoms g^{-1} yr^{-1}. Using both the Kober, *et al.* (2005) and Masarik (2002) values, the P10px is systematically ~17-19% lower than P10qtz (*see table 3.7*).

Table 3.7: Theoretical ^{10}Be pyroxene production rates calculated using previously established simulated elemental ^{10}Be production rates from Kober, *et al.* (2005) and Masarik (2002), and the Murimotu pyroxene sample compositions. Theoretical production rates calculated for both pyroxene and quartz are shown for comparison.

	Theoretical production rates (at g^{-1} yr^{-1})		
	Pyroxene	Quartz	% reduction
Kober (2005)			
MM-12-01	4.17	5.02	16.9
MM-12-02	4.18	5.02	16.7
MM-12-03	4.16	5.02	17.1
MM-12-04	4.13	5.02	17.6
Arithmetic mean	4.16	5.02	17.1
Masarik (2002)			
MM-12-01	4.62	5.64	18.1
MM-12-02	4.67	5.64	17.2
MM-12-03	4.61	5.64	18.3
MM-12-04	4.58	5.64	18.9
Arithmetic mean	4.62	5.64	18.1

For comparison, the P10px values determined both theoretically and empirically at the Murimotu debris avalanche, using pyroxene composition, and direct cross-calibrations with the ^{3}He concentration and the radiocarbon age, are summarised in *figure 3.2.*

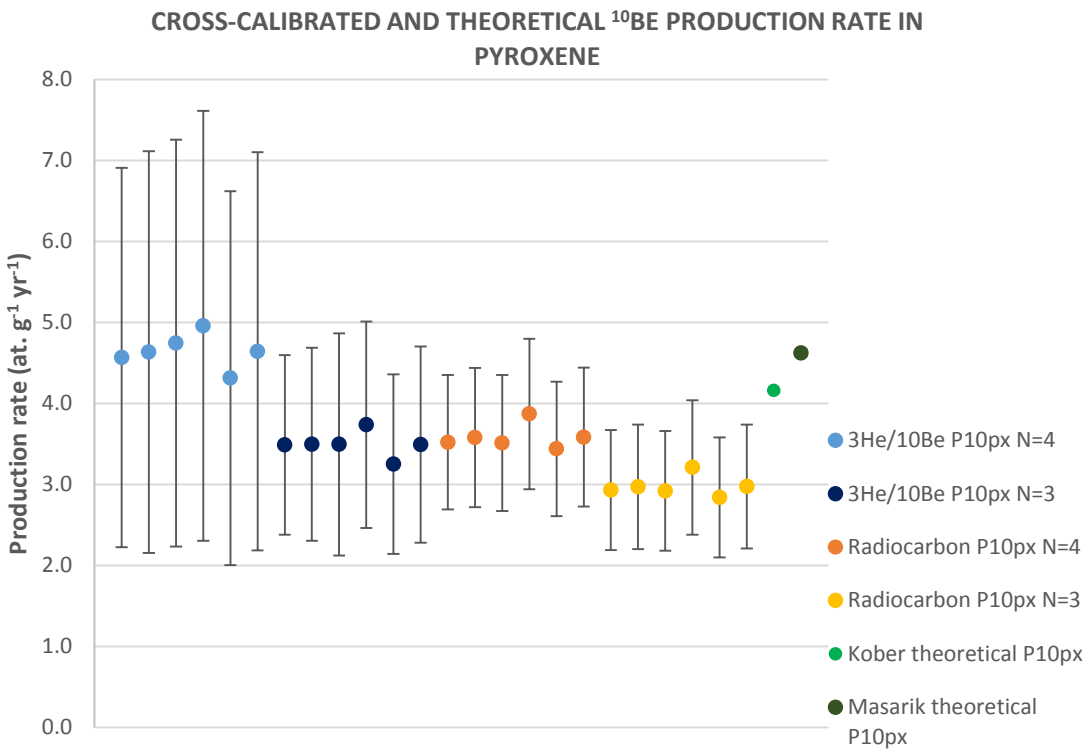

Figure 3.2: ^{10}Be production rates in pyroxene from cross calibration with ^{3}He concentration (^{3}He/^{10}Be P10px) and the radiocarbon age of the Murimotu debris avalanche (Radiocarbon P10px). The production rates are shown for the average of all four samples (N=4) and the average when sample MM-12-03 is excluded as an outlier (N=3). Each of the points represents an average production rate for each scaling scheme (St, De, Du, Li, and Lm respectively), and the sixth point represents an average of all scaling schemes. The average theoretical ^{10}Be production rates (± max/min) for pyroxene determined using the Kober, *et al.* (2005) elemental production rates and the Masarik (2002) values are presented here also.

3.2.5 P10px-radiocarbon internal consistancy test

In order to test internal consistency between the P10px-radiocarbon and the ^{3}He production rate determined by Eaves, *et al.*, (2015), the ^{10}Be concentration of the JC2 leach test samples were converted to exposure ages using the determined P10px-radiocarbon. Exposure ages were obtained for only the post HF samples (JC2 post HF2, post HF3, post HF4 and post HF7) as the two initial leaching steps in $NH_2OH{\cdot}HCl$ and HCl contained meteoric ^{10}Be. As the JC2 rock sample has been independently exposure dated by S. Eaves (pers. comm.) using cosmogenic ^{3}He, a comparison can be made. Both the ^{3}He production rate used by Eaves, *et al.* (2015) and the P10px were calibrated using the independent radiocarbon age of the Murimotu debris avalanche, and the Lm scaling scheme. The ^{10}Be exposure ages calculated (using the CRONUS-Earth online calculator using P10px-radiocarbon) for the four JC2 post HF samples and the ^{3}He exposure age for the sample are shown in *table 3.8* and *figure 3.3*. The ^{10}Be age of each JC2 post HF sample are within error of the ^{3}He exposure age determined for the sample. This means the production rates are internally consistent, as they were determined using the same independent radiocarbon age.

Table 3.8: Sample JC2 leach test exposure age determination.

Sample	Exposure age (yr)
JC2 – post HF2	7002 ± 2748
JC2 – post HF3	10032 ± 3080
JC2 – post HF4	7648 ± 2663
JC2 – post HF7	12201 ± 5289
JC2 arithmetic average	9221 ± 3445
^{3}He exposure age[a]	8804 ± 789

[a] Independent ^{3}He exposure age provided by S. Eaves

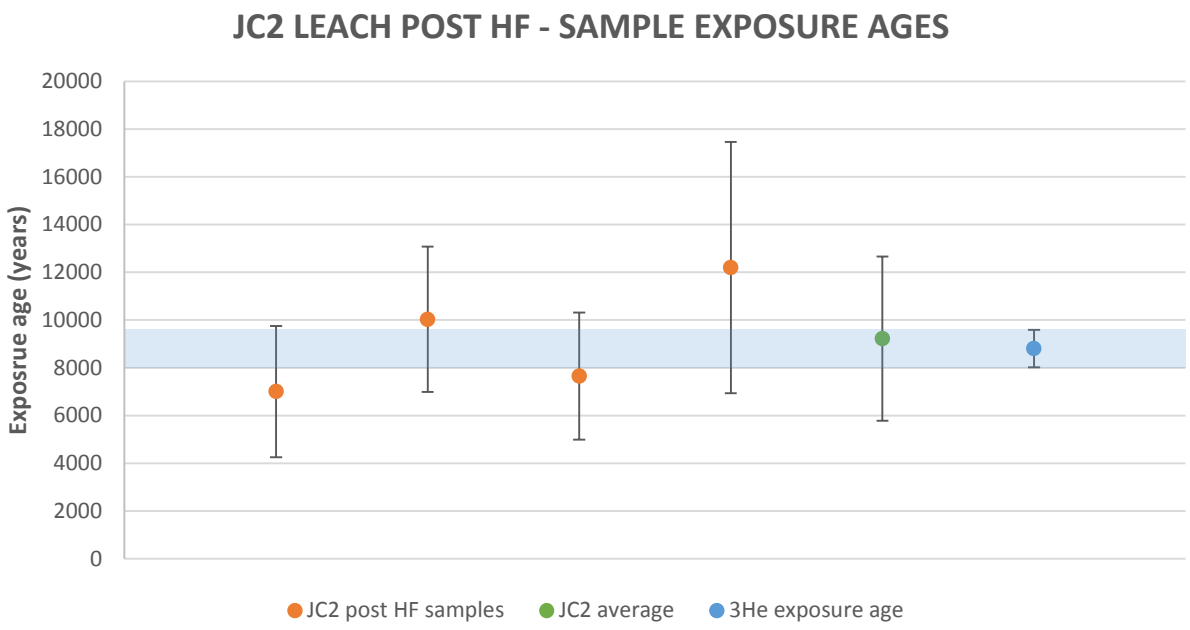

Figure 3.3: JC2 leach post HF sample ^{10}Be exposure ages. The production rates for both ^{10}Be and ^{3}He are calibrated using cross-calibration with the Murimotu radiocarbon age, and both are scaled with the Lm scaling scheme showing external uncertainties. All four of the JC2 post HF samples are within error of the ^{3}He age showing internal consistency between the production rates.

3.3 Exposure ages

The third aim of this thesis was to date glacial erratics and bedrock samples in Antarctica by applying both the improved decontamination procedure and ^{10}Be pyroxene production rate. The samples were collected from Mount Gran, adjacent to Mackay Glacier. The exposure ages obtained from these samples may allow the timing and rate of ice-surface lowering to be established for the upper Mackay Glacier. Eight cobble erratics and nine striated bedrock samples were collected, however only seven of these bedrock samples could be measured due to a high boron count during AMS measurement. The sample locations, descriptions and ^{10}Be concentrations are shown in *table 3.9.*

3.3.1 Mount Gran exposure ages

Exposure ages were calculated using the CRONUS-Earth online exposure age calculator using the P10px-radiocarbon determined at the Murimotu calibration site using all four samples (N=4), and for an Antarctica pressure field. The reason for the use of this production rate this is discussed in section 4.2.8. These production rates varied between 3.4 ± 0.8 and 3.9 ± 0.9 atoms g^{-1} yr^{-1}, dependant on the scaling scheme used. The calculated exposure ages are shown in *table 3.10* and are plotted against elevation above the ice surface in *figure 3.4*. The modern ice surface elevation is 928m a.s.l. at Mount Gran.

Both internal and external uncertainties are represented in the table; the external uncertainties are shown beside each calculated value after the ± and the internal uncertainties are in the parentheses beside the 'Lm' scaling scheme exposure ages. The external uncertainties are based on scaling scheme and production rate uncertainties so will differ depending on what scaling scheme is used. Whereas, the internal errors are purely analytical so will be the same irrespective of the scaling scheme used, hence are only shown in the table once. *Figure 3.4* uses the exposure ages produced using the Lm scaling scheme; which will be the scaling scheme used for the remainder of this work. The Lm scaling scheme determined by Nishiizumi, *et al.* (1989), Lal (1991), and Stone (2000), accommodates changes in the strength of Earth's paleomagnetic field over time, as well as changes in latitude and altitude for cosmogenic production rates at the surface.

Table 3.9: Mount Gran sample data and measured ^{10}Be concentration.

Sample name	Latitude (DD)	Longitude (DD)	Elevation (m a.s.l.)	Elevation above ice (m)	Sample type	Thickness (cm)	Density (g. cm^{-2})	Shielding correction	^{10}Be concentration ± 1σ (10^4 at. g^{-1})
MG01	-76.998945	161.042204	970	42	cobble on bedrock	1.5	3	0.975	8.72 ± 4.63
MG02-B	-76.998945	161.042204	970	42	bedrock	2.0	3	0.975	29.07 ± 6.62
MG07	-76.998116	161.039141	1022	94	cobble on bedrock	1.8	3	0.989	39.11 ± 9.48
MG08-B	-76.998116	161.039141	1022	94	bedrock	1.0	3	0.987	55.49 ± 1.07
MG12	-76.99846	161.037602	1013	85	cobble on bedrock	5.8	3	0.979	11.81 ± 4.79
MG13-B	-76.998493	161.037559	1013	85	bedrock	2.0	3	0.979	77.86 ± 2.44
MG15	-76.998644	161.040447	997	69	cobble on bedrock	3.8	3	0.985	22.35 ± 5.67
MG19	-76.999122	161.040565	981	53	cobble on bedrock	4.0	3	0.988	13.31 ± 6.05
MG22	-76.998669	161.042777	976	48	cobble on bedrock	4.6	3	0.985	12.47 ± 4.18
MG30	-76.997069	161.041588	1043	115	cobble on bedrock	2.0	3	0.986	17.73 ± 4.26
MG32	-76.997141	161.04084	1043	115	cobble on bedrock	3.5	3	0.986	16.67 ± 5.65
MGW01	-76.59912	161.02356	1000	72	weathered bedrock	2.0	3	0.985	54.05 ± 9.56
MGW03	-76.59912	161.02356	1000	72	weathered bedrock	2.0	3	0.985	34.55 ± 8.39
MGW04	-76.59855	161.02143	1039	111	weathered bedrock	2.0	3	0.982	32.78 ± 6.18
MGW05	-76.59847	161.02211	1035	107	weathered bedrock	2.0	3	0.989	38.90 ± 5.88

Table 3.10: Exposure ages for Mount Gran calculated using CRONUS-Earth calculator using P10px-radiocarbon.

Sample	Thickness scaling factor	Shielding factor	Elevation above ice (m)	Exposure age (yr)				
				St	De	Du	Li	Lm
Cobbles								
MG01	0.9861	0.975	42	7371 ± 4285	7605 ± 4438	7643 ± 4456	7357 ± 4294	7544 ± 4406 (3920)
MG22	0.9581	0.985	48	10685 ± 4388	11024 ± 4561	11078 ± 4574	10711 ± 4435	10936 ± 4532 (3598)
MG19	0.9634	0.988	53	11266 ± 5776	11622 ± 5988	11679 ± 6009	11293 ± 5821	11531 ± 5947 (5133)
MG15	0.9652	0.985	69	18735 ± 6376	19320 ± 6648	19413 ± 6660	18651 ± 6423	19176 ± 6613 (4601)
MG12	0.9475	0.978	85	9988 ± 4692	10296 ± 4865	10345 ± 4881	9988 ± 4722	10223 ± 4836 (4063)
MG07	0.9833	0.989	94	31472 ± 10696	32441 ± 11149	32592 ± 11167	31171 ± 10720	32217 ± 11097 (7687)
MG30	0.9815	0.999	115	13493 ± 4605	13899 ± 4796	13964 ± 4803	13462 ± 4649	13811 ± 4776 (3336)
MG32	0.9679	0.986	115	13350 ± 5521	13752 ± 5730	13816 ± 5745	13322 ± 5554	13665 ± 5702 (4541)
Bedrock								
MG02-B	0.9815	0.975	42	24791 ± 8154	25582 ± 8514	25707 ± 8529	24642 ± 8209	25376 ± 8466 (5681)
MGW01	0.9815	0.985	72	44717 ± 13280	46121 ± 13900	46339 ± 13911	44243 ± 13346	45777 ± 13838 (7995)
MGW03	0.9815	0.985	72	28468 ± 9679	29498 ± 10111	28237 ± 9715	28237 ± 9715	29140 ± 10041 (6963)
MG13-B	0.9815	0.979	85	64376 ± 25641	66386 ± 26670	66697 ± 26737	63573 ± 25542	65911 ± 26522 (20544)
MG08-B	0.9907	0.987	94	44559 ± 13670	45935 ± 14288	46147 ± 14301	44050 ± 13713	45616 ± 14228 (8672)
MGW05	0.9815	0.989	107	31006 ± 8719	31950 ± 9130	32098 ± 9132	30696 ± 8782	31740 ± 9100 (4724)
MGW04	0.9815	0.982	110	26187 ± 7933	26980 ± 8288	27105 ± 8295	25951 ± 7980	26806 ± 8257 (4972)

Both external and internal uncertainties are shown (internal uncertainties shown in parentheses for Lm scaling scheme only as internal uncertainties are the same irrespective of scaling scheme). Internal uncertainties are analytical uncertainties, and external uncertainties include scaling scheme and production rate errors.

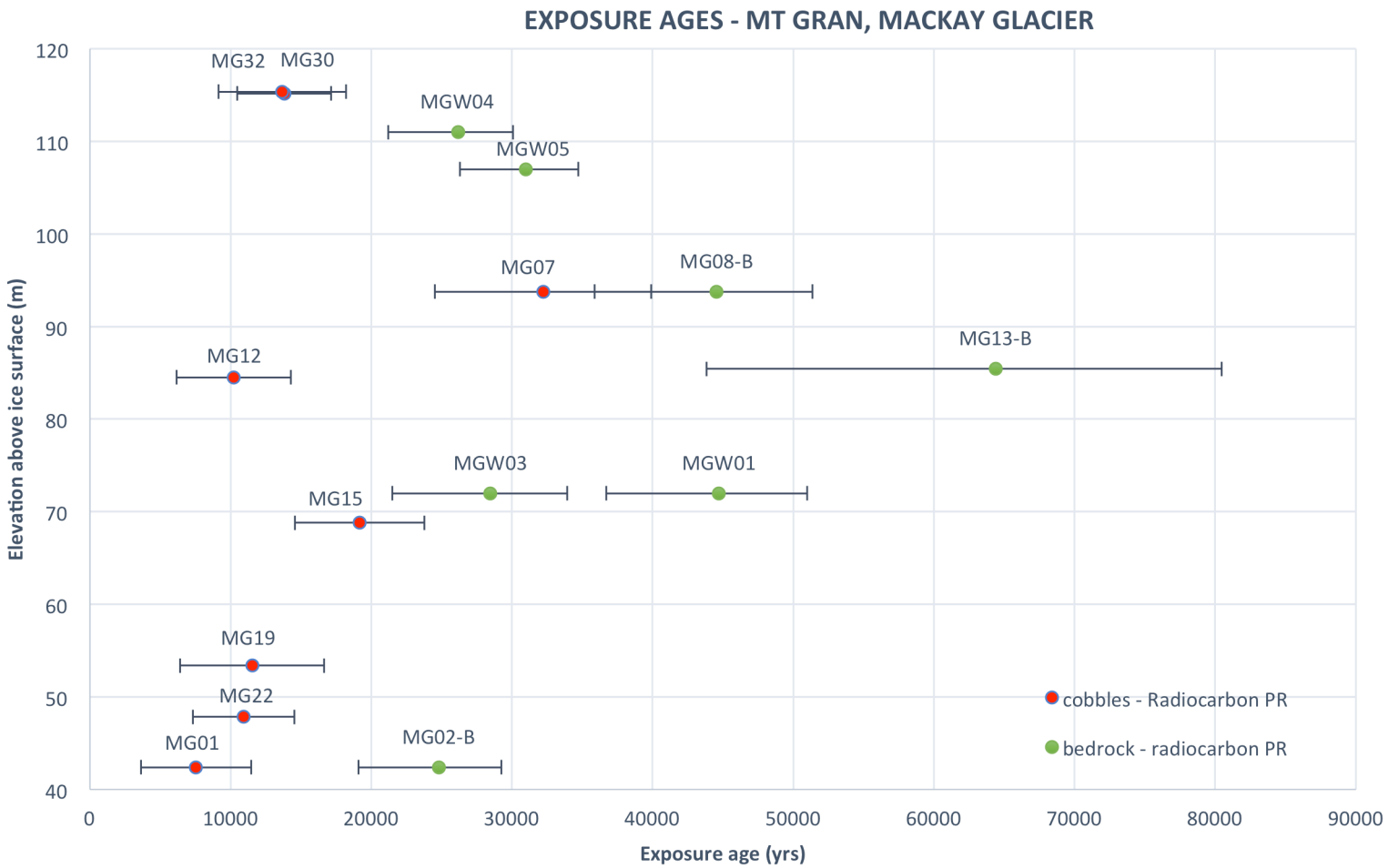

Figure 3.4: Mount Gran exposure ages plotted against elevation above the modern glacier ice surface. Exposure ages calculated using the radiocarbon calibrated P10px using the Lm scaling scheme. Internal errors are shown.

3.3.1.1 Bedrock samples

The bedrock samples provide older exposure ages than the cobbles, with the exception of cobble MG07. The bedrock exposure ages range between 25806 ± 4972 and 65911 ± 50544 yrs. At sites where both a bedrock sample and a cobble were collected, the exposure age of the bedrock is older than the cobble, throughout. These age offsets are reported in *table 3.11*.

Table 3.11: Age offset between cobbles MG01, MG07 and MG12 with their respective bedrock sample MG02-B, MG-08-B and MG13-B, collected at the same site. External uncertainties shown.

Samples	Cobble age (yr)	Bedrock age (yr)	Age offset (yr)
MG01 and MG02-B	7544 ± 3920	25376 ± 5681	~18
MG07 and MG08-B	32217 ± 7687	45616 ± 8672	~13
MG12 and MG13-B	10223 ± 4063	65911 ± 20544	~55

3.3.1.2 Cobble erratics

The cobble erratics have generally younger exposure ages than the bedrock samples. The age of the cobbles using the Lm scaling scheme range between 7544 ± 3920 (MG01) and 32217 ± 7687 (MG07) yrs. Assuming the glacier surface lowered between the LGM and Holocene, we would expect the older ages to correspond to the highest rocks, because as the ice surface lowered, the rocks at the highest elevations would be exposed to the cosmic ray flux first. The cobbles collected at the highest elevation (MG30 and MG32), 115 m above the modern ice surface, have exposure ages of 13811 ± 3336 and 13665 ± 4541 yrs respectively. These ages are indistinguishable within error, and provide a robust exposure age for the top of the

transect. However, below these samples, the remaining cobbles have variable exposure ages, both younger and older than the highest samples of the transect. The sample immediately below MG30 and MG32 is sample MG07 at 94 m above the ice surface, which with the age of 32217 ± 7687 yrs. This is older than both MG30 and MG32, outside of the internal uncertainty. This is stratigraphically illogical as no sample should be older than the sample above it, meaning either sample MG07 is an outlier with inherited cosmogenic ^{10}Be, or both MG30 and MG32 have experienced post depositional erosion or re-orientation and have an incorrect (young) age. However, it is more likely that MG07 contains inherited nuclides and is an outlier. Below MG07, the remaining samples become younger at lower elevations. The cobble at the lowest elevation above the ice surface (MG01), 42 m above the ice surface, corresponds to the youngest exposure age of 7544 ± 3920 yrs.

3.3.2 Mackay Glacier ice surface lowering

In order to compare the rates and timing of ice surface lowering at Mount Gran to the rest of Mackay Glacier, the exposure ages for the cobble erratics have been compared to exposure ages from Mt Suess, a nunatak further downstream, which has been exposure dated using cosmogenic ^{10}Be in quartz by Jones, *et al.* (submitted). Only the cobble erratics are used to represent this event at Mount Gran, as the bedrock is likely to contain inherited cosmogenic ^{10}Be and is unlikely to represent the true exposure age. The Mount Gran and Mount Suess exposure ages were both determined using ^{10}Be production rates calibrated in New Zealand sites. The Mount Gran exposure ages were calculated using the P10px-radiocarbon, determined in the central North Island; and the Mount Suess exposure ages were calculated using the Putnam,

et al. (2010) production rate for ^{10}Be in quartz, calibrated in the Southern Alps. Additionally both sets of ages are calculated using the Lm scaling scheme.

The exposure ages and elevations (in m) above sea level and above the modern ice surface at each site are shown in *table 3.12*, and are plotted in *figures 3.5A and 3.5B*, respectively. As cobbles MG30 and MG32 are at the same elevation, the age and 1σ external uncertainties have been averaged. The Mount Gran transect spans ~70 m, and the Mount Suess transect spans ~230 m elevation. The oldest two Mount Suess ages (at ~21 ka and 26 ka) are possible outliers, as suggested by Jones, *et al.* (submitted), thus are not included in *figure 3.5*, and are not further discussed in this thesis. The remaining Mount Suess samples all exhibit exposure ages of ~7 ka, with the exception of the lowest sample exhibiting the youngest exposure age of ~4.5 ka. The ice surface lowered ~180 m over a maximum of ~850 years at Mount Suess. This phase of rapid ice surface lowering is shaded blue in *figure 3.5.* The exposure ages for the Mount Gran erratics are generally older, but are within error of the exposure ages for the erratics sampled on Mount Suess. MG07 is included in *figure 3.5A*, but is excluded in *figure 3.5B* as an outlier. Both MG15 and MG30/MG32 also lie outside of uncertainties of the Mount Suess ages, however, they are much closer in age to the remaining Mount Gran exposure ages and are included in the plot. The ice surface lowered ~70 m over approximately 5.5 ka, however, this is hard to constrain because of the large uncertainties associated with the exposure ages. These plots are further discussed in section 4.3.3.

Table 3.12: Mackay Glacier ice surface lowering. Elevations above sea level and ice surface, and exposure ages ± external uncertainties for the upstream Mt Gran and downstream Mt Suess.

	Altitude (m a.s.l.)	elevation above ice (m)	Exposure age (yr)
Mt Gran			
MG32/30 [a]	1043	115	13738 ± 5239
MG07	1021	94	32217 ± 11097
MG12	1013	85	10223 ± 4836
MG15	997	69	19176 ± 6613
MG19	981	53	11531 ± 5947
MG22	976	48	10936 ± 4532
MG01	970	42	7544 ± 4406
Mt Suess [b]			
	824	261	26030 ± 1077
	823	260	21372 ± 3610
	794	231	7657 ± 286
	781	218	7555 ± 174
	710	147	7481 ± 139
	648	85	7416 ± 129
	629	66	7342 ± 141
	613	50	7265 ± 168
	587	24	4479 ± 712

[a] Samples MG30 and MG32 combined as they are at the same elevation.
[b] Data for Mt Suess provided by R. S. Jones.
Mt Gran ages calculated using CRONUS-Earth calculator with P10px-radiocarbon. Mt Suess ages determined using ^{10}Be in quartz using the production rate by Putnam, *et al.* (2010). Both sets of ages scaled using Lm (Lal/Stone d-t) scaling scheme.

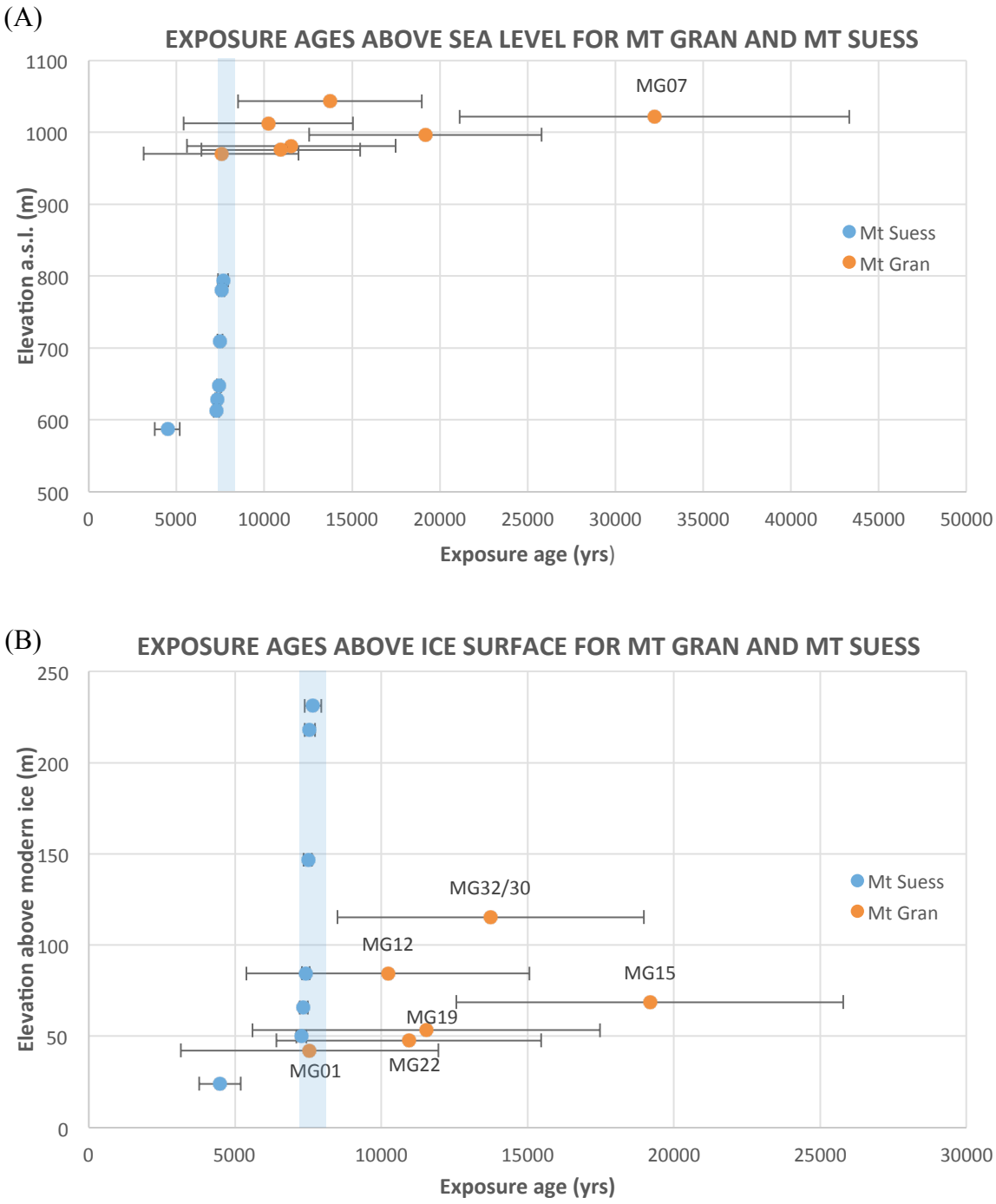

Figure 3.5: Exposure ages above sea level (A) and above the modern ice surface (B) at Mount Gran and Mount Suess adjacent to Mackay Glacier. The Mount Gran samples were exposure dating using the P10px-radiocarbon, and the Mount Suess samples were exposure dated using P10qtz from Putnam, *et al.* (2010) As both of these production rates are calibrated at sites in New Zealand, and are both scaled using the Lm scheme, they are comparable. External uncertainties represented. Sample MG07 has been excluded in plot (B) as it is an outlier and does not represent ice surface lowering. The shaded blue represents the episode of rapid ice surface lowering observed at Mount Suess.

3.4 Chapter summary

To summarise the results; the leaching procedure was successful in effectively removing meteoric ^{10}Be from pyroxene grains, allowing the *in situ* ^{10}Be concentration to be measured. Production rates for ^{10}Be in pyroxene were then determined empirically using direct cross-calibration with the ^{3}He concentration and independent radiocarbon age of the Murimotu debris avalanche, and theoretically using elemental ^{10}Be production rates and the pyroxene composition. The ^{10}Be production rates, both empirically and theoretically, are 8-27% lower than ^{10}Be production rates in quartz. Using the P10px-radiocarbon of 3.4 ± 0.8 atoms g^{-1} yr^{-1} (N=4, Lm scaling scheme), exposure ages were determined for cobble erratics and bedrock samples collected on Mount Gran in Antarctica. The exposure ages of the cobble erratics show a relatively rapid phase of ice surface lowering on the adjacent Mackay Glacier of ~60 m ice loss between 13.5 and 11 ka. The volume of ice loss is similar to what has been previously measured down-glacier, by Jones, *et al.* (submitted). However, the timing of the rapid thinning phase differs between the sites, with Mount Gran showing earlier rapid thinning than sites down-glacier.

Chapter Four: Discussion

This chapter is structured in a similar manner to Chapter Three; where the chemistry and ^{10}Be measurement is discussed in section 4.1; followed by analysis of the cross-calibrated, and theoretically calculated production rates in section 4.2. Lastly, section 4.3 discusses the application of the determined production rates for Mount Gran exposure ages and the implications these associated ages have on understanding thinning rates of Mackay Glacier.

4.1 Chemistry and ^{10}Be measurement

Using the JC2 leach sample, the decontamination procedure of Blard, *et al.* (2008) has proven to be effective at removing the meteoric component of ^{10}Be within the Ruapehu lava sample (section 2.4.1.4). The results from analysis of JC2 suggest that after ~20 % of the original mass was dissolved, the meteoric ^{10}Be component had been completely removed, leaving only the *in situ* ^{10}Be fraction remaining. Thus, the remainder of the samples underwent the two leaches in $NH_2OH{\cdot}HCl$ and HCl, followed by only one dissolution in 4M HF. However, as the mass of the pyroxene was decreased to ~4 grams for the Murimotu and Mount Gran samples, the mass removed during the leaches and the first HF dissolution was up to 80% of the original mass leaving as little as 0.73g pyroxene remaining to measure the *in situ* ^{10}Be concentration (in sample MGW01). While smaller dissolved amounts are better for

beryllium separation, the mass of pyroxene initially dissolved must be enough to effectively remove the meteoric ^{10}Be, while retaining enough material to gain high precision measurements. The amount of pyroxene dissolved during the HF dissolution step varied between samples, generally as a result of the weathering of the pyroxene in the samples. For example, in the Murimotu samples (MM) the pyroxenes are relatively young and un-weathered, resulting in 35-45% total mass loss after HF1. However, in the Mount Gran samples (MG and MGW) the total mass lost is 62-82%, as the more weathered pyroxenes are easily dissolved. The amount dissolved is variable and hard to control, and requires further improvement.

After the removal of meteoric ^{10}Be, as only small amounts of pyroxene were dissolved, (between 0.04 and 2.8 g for each sample), the measured ^{10}Be/^{9}Be ratio was very low (as low as 7.4 x10^{-15} in MG01). This has provided large analytical uncertainties (up to 33%) purely from the low measured ratio. However, regardless of small dissolved amounts, the ratios are still a minimum of 3x above the blank value (of 2.0 x 10^{-15}). Thus, despite the large analytical errors, the measurements are reliable. Although samples JC2- hydrox and JC2- HCl had only 0.04 g and 0.13 g of pyroxene dissolved, respectively, these leaches were enriched in meteoric ^{10}Be, resulting in significantly higher ^{10}Be/^{9}Be ratios, with low analytical errors.

In addition to the small amount of pyroxene dissolved in each sample, beryllium was lost during the chemistry, decreasing the total beryllium for measurement. It is not known in which step this beryllium was lost; however, based on experiments performed, it is unlikely that substantial beryllium was lost during precipitation, the water leach, or the cation columns. In order to understand what happened to the ‘lost

fraction' of beryllium, further investigation into the chemical procedure is required. This is especially important because the low yields exacerbate the poor precision of the AMS measurements due to short measuring times.

In order to decrease the analytical uncertainties for the ^{10}Be measurement in pyroxene, more material could initially be dissolved for each sample. However, this would require more resin in the cation columns and larger volumes of acid to be used for each sample to elute beryllium as there would be more major cations needing separation. Furthermore, the recovery of the 'lost fraction' of beryllium would increase the beryllium yield of the sample. In conclusion, further improvements to the chemical decontamination procedure would increase beryllium yield for each sample, and therefore decrease the analytical uncertainty in the ^{10}Be/^{9}Be ratios. These will be further discussed in the further improvements section in chapter 5.

4.2 Production rate calibration

4.2.1 ^{10}Be production rate from cross-calibrations at Murimotu site

As the Murimotu debris avalanche has been independently radiocarbon dated, and the cosmogenic ^{3}He concentration in the pyroxene measured by Eaves, *et al.* (2015), P10px were able to be determined via direct cross-calibration with these values using the ^{10}Be concentration measured in the four Murimotu samples. However, as sample MM-12-03 has a higher ^{10}Be concentration (~13 x 10^{6} atoms g^{-1}) than the remaining three samples (between ~5 – 9 x 10^{6} atoms g^{-1}), it could be considered an outlier (see

table 3.1). As it was considered a potential outlier by Eaves, *et al.* (2015), P10px have been determined for both N=4 and N=3.

As sample MM-12-03 was collected in three pieces (see *figure 3.1*) and different sections were processed for each nuclide, this could be the cause for the difference between the ^{3}He and ^{10}Be concentrations in the sample. It is possible that one section could have experienced greater weathering, erosion, or self-shielding, lowering the ^{3}He concentration. Additionally volcanic samples from subduction zone volcanism can have a higher ^{10}Be concentration as a result of the incorporation of magmatic ^{10}Be into the sample (Morris, *et al.*, 2002) as discussed below.

4.2.2 Magmatic component of ^{10}Be in island arc settings

When measuring *in situ* ^{10}Be concentrations in geologically young volcanic samples in rapid subduction zones, the presence of initial ^{10}Be incorporated into the magma through subduction must be considered (Brown, *et al.*, 1982; Monaghan, *et al.*, 1988). This ^{10}Be is unable to be separated during the leaching steps as it is located within the crystal lattice as inherited *in situ* ^{10}Be. As the half-life of ^{10}Be is 1.39 Myr (Chmeleff, *et al.*, 2010; Korschinek, *et al.*, 2010), this magmatic ^{10}Be should be minimal in geologically older samples. However, in recent volcanic deposits it can represent a significant proportion of the *in situ* concentration (Morris, *et al.*, 2002). Additionally, the subduction time must be rapid enough (less than 4-5 Myr) so the ^{10}Be does not completely decay away during subduction or transport through the mantle to the surface (Morris, *et al.*, 2002). This could potentially explain the inter-sample

variations in ^{10}Be concentration, as some lavas could be preferentially enriched in magmatic ^{10}Be. As the Murimotu debris avalanche was a gravitational sector collapse, the deposit consists of a range of lava flows (Palmer & Neall, 1989). Sample MM-12-03 could originate from a lava flow with a higher magmatic ^{10}Be signature, giving it a higher ^{10}Be concentration than the remaining Murimotu samples. Unfortunately, to date, no work has been done on the magmatic ^{10}Be component of the Taupo Volcanic Zone volcanoes.

4.2.3 ^{10}Be production rate from ^{3}He cross-calibration

Using the ^{3}He concentration of the Murimotu pyroxene and the Goehring, *et al.* (2010) ^{3}He production rate at sea-level high-latitude (SLHL), a P10px was established using equation 3.1. The SLHL production rate for the arithmetic mean of all four samples (N=4) is 4.3 ± 2.3 atoms g^{-1} yr^{-1} (Lm scaling), and 3.3 ± 1.1 atoms g^{-1} yr^{-1} excluding sample MM-12-03 (N=3) (*table 3.4*). The error on the N=4 production rate is ~53%, but drops to ~34% using the production rate if MM-12-03 is excluded (N=3). The errors on these production rates are large as the uncertainties include errors propagated from the normalised ^{10}Be concentration, the normalised ^{3}He concentration, and the reference Goehring, *et al.* (2010) ^{3}He production rate.

4.2.4 ^{3}He/^{10}Be ratios

The ratio of the $^{3}He/^{10}Be$ concentration in the Murimotu pyroxene varies between samples. As sample MM-12-03 had a higher ^{10}Be concentration and a lower ^{3}He concentration than the remaining Murimotu samples, the $^{3}He/^{10}Be$ ratio is lower, only 16.3 ± 2.9. The remaining three samples have ratios between 27.5 ± 6.5 and 51.0 ± 16.3. The average of these values (for N=4) is 34.5 ± 9.9, which is similar to previous estimates of $^{3}He/^{10}Be$ ratios measured in New Zealand; Eaves *et al.* (2015) calculated the ratio of production rates in New Zealand for ^{3}He in pyroxene to ^{10}Be in quartz (from Putnam, *et al.*, 2010), to be 32.5 ± 3.3. This is indistinguishable from the average $^{3}He/^{10}Be$ ratio measured from concentrations of both nuclides in the same pyroxene at the Murimotu site. This ratio determined for $^{3}He/^{10}Be$ in pyroxene is also comparable to global ^{3}He-pyroxene/^{10}Be-quartz ratios; such as that of Blard, *et al.* (2013) in the high Tropical Andes of 33.3 ± 0.9, and that of Amidon, *et al*. (2009) (also calculated by Blard, *et al.* 2013) of 32.3 ± 0.9. The similarity of $^{3}He/^{10}Be$ in pyroxene and $^{3}He/^{10}Be$ in quartz ratios are suggests that there is minimal difference between the production rates of ^{10}Be in pyroxene and quartz. However, the large variability in ratios precludes a definitive statement with this method.

4.2.5 ^{10}Be production rate from radiocarbon cross-calibration

In addition to the cross-calibration with ^{3}He, P10px were also determined using the independent radiocarbon age of 10.6 ± 0.1 ka, for the Murimotu debris avalanche (Eaves, *et al.*, 2015). Using this approach, the compound errors are reduced as the only errors are in the normalised ^{10}Be concentration and the radiocarbon age, eliminating any errors associated with ^{3}He. This cross-calibration provides P10px of 3.4 ± 0.8 atoms g^{-1} yr^{-1} for N=4 (Lm scaling, at SLHL) and 2.8 ± 0.7 atoms g^{-1} yr^{-1} if

MM-12-03 is excluded (N=3). The uncertainties produced are lower, only 24% for N=4, and 26% for N=3.

4.2.6 Theoretical ^{10}Be production rates in pyroxene

The theoretical ^{10}Be production rates in pyroxene vary depending on mineral composition and the elemental production rates used. The Kober, *et al.* (2005) elemental production rates yield an average production rate of 4.16 atoms g^{-1} yr^{-1}, based on the composition of the Murimotu samples (see *table 3.6*). The same pyroxene compositions yield production rates of 4.62 atoms g^{-1} yr^{-1} when using the elemental production rates of Masarik (2002). The difference between these production rates is likely a result of the neutron capture cross-sections used in the modelling (Kober, *et al.*, 2005). The Masarik (2002) elemental production rates are based on the assumption of equal cross-sections. However, physical modelling experiments performed by Kober, *et al.* (2005) discovered that the assumption of equal cross-sections is generally not valid, resulting in lower production rates. Thus, the elemental production rates produced by Kober, *et al.* (2005) have been adjusted to account for this. Uncertainties were not given by either author, but based on common production rate uncertainties of ~10% (Balco, *et al.* 2008), these are likely indistinguishable.

4.2.7 Comparison of ^{10}Be production rates in pyroxene and quartz

Estimates of the production rate for ^{10}Be in quartz have reduced by ~20% in ~10 years (Balco, *et al.*, 2009; Putnam, *et al.*, 2010; Young, *et al.*, 2013; Heyman, *et al.*, 2014). As the production rate is constantly being updated as more calibration sites are established, there is a possibility that the Kober, *et al.* (2005) elemental production rates are now an overestimate of the true production rate. However, regardless of the absolute values, the ratio of ^{10}Be production in quartz and pyroxene should remain constant. To test this, theoretical ^{10}Be production rates for quartz (P10qtz) were also determined using the elemental production rates proposed by Masarik (2002) and Kober, *et al.* (2005). The production rates for ^{10}Be in quartz using the Masarik values are 5.64 atoms g^{-1} yr^{-1} and 5.02 atoms g^{-1} yr^{-1} using the Kober values. Using these theoretical ^{10}Be production rates, the P10px is ~17% lower than quartz using the Kober values, and ~18% lower using the Masarik values.

In order to assess if ^{10}Be production rates in pyroxene are also empirically lower than in quartz, the ^{10}Be pyroxene production rates determined via radiocarbon (P10px-radiocarbon) and cross-calibration with the ^{3}He concentration, have been compared with the more recent estimates of the ^{10}Be production rate in quartz. These are summarised in table 4.1.

Table 4.1: Percent reduction between ^{10}Be production rates in quartz and pyroxene. Calculations using scaling scheme averaged production rates. Error calculated using equation 3.2 for error propagation.

^{10}Be production rate px	**^{10}Be production rate qtz**	**% reduction**
Kober *et al.* (2005) P10px	Kober *et al.* (2005) P10qtz	~17
Masarik *et al.* (2003) P10px	Masarik *et al.* (2002) P10qtz	~18
P10px-radiocarbon N=4	Heyman (2014) P10qtz	12 ± 3
P10px-radiocarbon N=4	Putnam *et al.* (2010) P10qtz	8 ± 2
P10px-radiocarbon N=3	Heyman (2014) P10qtz	27 ± 7
^{3}He/^{10}Be P10px N=3	Heyman (2014) P10qtz	14 ± 5

There is a clear offset between the production rates of ^{10}Be in quartz and pyroxene both empirically and theoretically. Depending on the production rates compared, the ^{10}Be production rates in pyroxene are between 8 ± 2% and 27 ± 7% lower than production rates in quartz. An exception is the P10px calculated from cross-calibration with ^{3}He, which was actually higher than the recent estimates of production rates in quartz, and is not included in the table. Using the best comparison between P10px-radiocarbon (N=4) and the globally compiled Heyman, *et al.* (2014) P10qtz, the empirical percent reduction is 12 ± 3%. This is similar to, but smaller than the theoretical percent reduction of 17%. With an 8-27% reduction, the empirical ^{10}Be pyroxene production rates calculated in this thesis are in agreement with the theoretical calculations and show that a lower production rate should be used for ^{10}Be in pyroxene compared to quartz.

4.2.8 ^{10}Be production rate in pyroxene comparison

As more production rate calibration sites are being established globally, different ^{10}Be production rate values are being reported (Heyman, *et al.*, 2014). The discrepancies between these likely arise from unrecognised shielding from snow or sediment cover, or uncertainties in the exposure age of the calibration site (Gosse & Phillips, 2001). One of the first commonly accepted production rates for ^{10}Be in quartz is that of Nishiizumi, *et al.* (1989), of 6.03 atoms g^{-1} yr^{-1} SLHL. However, this didn't include the effects of time variations in the Earth's geomagnetic field strength and was consequently too high. Stone, (2000) solved this dilemma by creating a new scaling

scheme that addressed this variation, thus rescaling the production rate of ^{10}Be in quartz at SLHL to 5.1 ± 0.3 atoms g^{-1} yr^{-1}.

More recently, Balco, *et al.* (2008) established a SLHL production rate of 4.8 ± 0.4 atoms g^{-1} yr^{-1} (Lm scaling) based on a compilation of available calibrated ^{10}Be production rates in quartz. This is still the production rate value being used for the majority of exposure age calculations in CRONUS-Earth ver.2.2. However, Heyman, *et al.* (2014) have proposed that the Balco, *et al.* (2008) production rate is too high, based on a compilation of ^{10}Be production rates in quartz from 24 new global calibration sites. They have proposed a SLHL production rate of 4.0 ± 0.3 atoms g^{-1} yr^{-1} (Lm scaling), which can be used to calculate exposure ages using an alternative version within the CRONUS-Earth calculator. The Heyman, *et al.* (2014) production rate compilation includes the P10qtz calibrated in New Zealand by Putnam, *et al.* (2010) of 3.7 ± 0.08 atoms g^{-1} yr^{-1} (Lm scaling).

The P10px determined by this study, and the recent commonly accepted production rates for ^{10}Be in quartz are shown in *figure 4.1* for comparison. The associated production rates are shown in *table 4.2.*

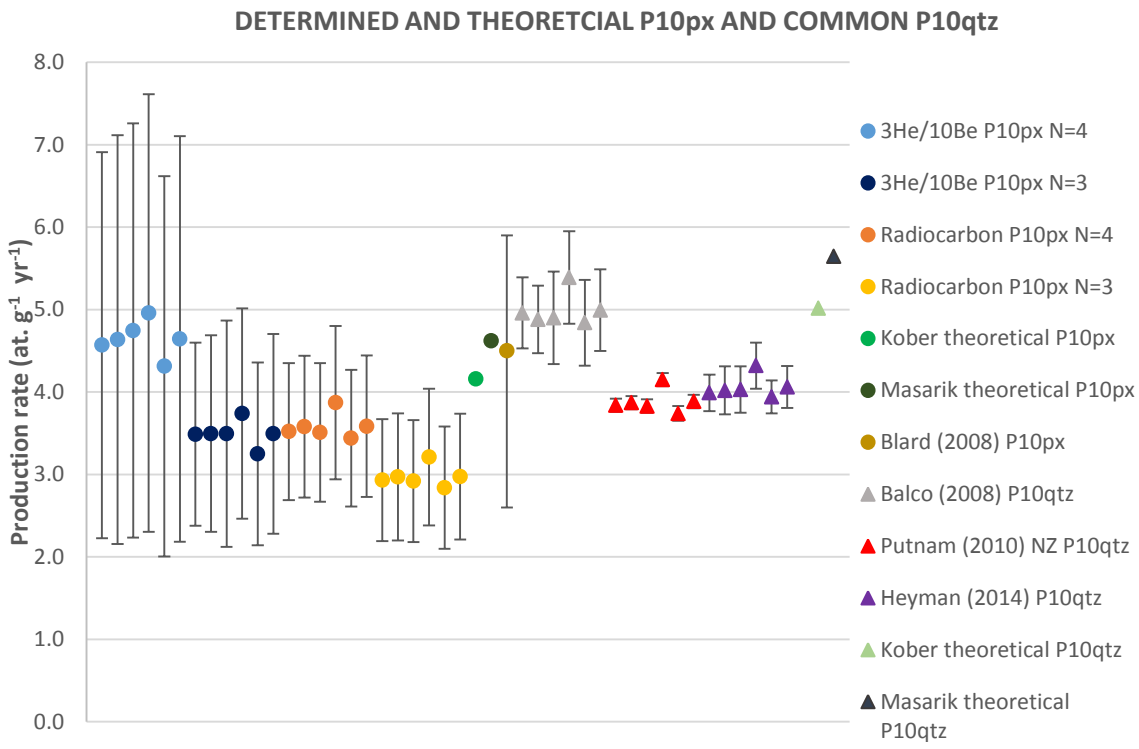

Figure 4.3: Determined and theoretical ^{10}Be production rates in pyroxene (circles), and commonly used ^{10}Be production rates in quartz for comparison (triangles). The production rates for ^{10}Be in pyroxene determined by cross-calibration with ^{3}He (^{3}He/^{10}Be P10px) using eq. 3.1, and radiocarbon (Radiocarbon P10px) of the Murimotu debris avalanche are shown for the average of all 4 samples, (N=4) and the average excluding sample MM-12-03 (N=3). The six points represent the average production rate using each scaling scheme (St, De, Du, Li, and Lm, respectively) and an average of all scaling schemes. Theoretical P10px and P10qtz (± max/min) calculated using eq. 3.3 with Kober, *et al*. (2005) and Masarik (2002) elemental production rate values are included. The Blard, *et al*. (2008) ^{10}Be pyroxene production rate (± max/min) is also included. Commonly used production rates for ^{10}Be in quartz also represented for comparison: the Balco, *et al*. (2008) values; the Putman, *et al*. (2010) values calibrated in New Zealand; and the updated Heyman (2014) values.

Table 4.2: Production rates for ^{10}Be in pyroxene determined from this study, and commonly accepted production rates for ^{10}Be in quartz for comparison. The Blard, *et al.* (2008) calculated ^{10}Be production rate for pyroxene from cross-calibration with ^{3}He is also included.

	Scaling scheme					
This study	St	De	Du	Li	Lm	Average
^{3}He/^{10}Be P10px N=4	4.6 ± 2.3	4.6 ± 2.3	4.7 ± 2.5	5.0 ± 2.7	4.3 ± 2.3	4.6 ± 2.5
^{3}He/^{10}Be P10px N=3	3.5 ± 1.1	3.5 ± 1.2	3.5 ± 1.4	3.7± 1.3	3.3 ± 1.1	3.5 ± 1.2
Radiocarbon P10px N=4	3.5 ± 0.8	3.6 ± 0.9	3.5 ± 0.8	3.9 ± 0.9	3.4 ± 0.8	3.6 ± 0.9
Radiocarbon P10px N=3	2.9 ± 0.7	3.0 ± 0.8	2.9 ± 0.7	3.2± 0.8	2.8 ± 0.7	3.0 ± 0.8
	Minimum	Maximum				Average
Kober theoretical P10px	4.13	4.18				4.16
Masarik theoretical P10px	4.58	4.67				4.62
Commonly used values	St	De	Du	Li	Lm	Average
Balco *et al.* (2008) P10qtz	5.0 ± 0.4	4.9 ± 0.6	4.9 ± 0.6	5.4 ± 0.5	4.8 ± 0.4	5.0 ± 0.5
Putman *et al.* (2010) P10qtz	3.8 ± 0.1	3.9 ± 0.1	3.8 ± 0.1	4.15 ± 0.1	3.7 ± 0.1	3.9 ± 0.1
Heyman (2014) P10qtz	4.0 ± 0.2	4.0 ± 0.3	4.3 ± 0.3	3.9 ± 0.2	4.0 ± 0.3	4.1 ± 0.3
	Minimum	Maximum				Average
Blard *et al.* (2008) P10px	3.4 ± 0.8	5.0 ± 0.9				4.5 ± 0.4

The P10px determined using cross-calibration with ^{3}He and radiocarbon at the Murimotu calibration site all overlap within the 1 standard deviation uncertainties. The theoretical P10px, determined using the Kober, *et al.* (2005) elemental production rates, are the same within error of the P10px-radiocarbon. However, the Masarik (2002) theoretical production rates are higher, and are outside of the error of P10px-radiocarbon, meaning that they are likely an overestimation of the true ^{10}Be production rates in pyroxene. Additionally, the P10px-radiocarbon value overlaps within error of the Heyman, *et al.* (2014) production rates for quartz, however the uncertainty associated with the P10px-radiocarbon values are large. Furthermore, the P10px-radiocarbon values fall within the range of P10px values produced by Blard, *et al.* (2008). In comparing our P10px-radiocarbon to the values produced by Blard, *et al.* (2008), I suggest that a lower production rate for ^{10}Be in pyroxene is valid.

As the production rate for ^{10}Be in pyroxene is shown to be both theoretically and empirically lower than production rates in quartz, the radiocarbon derived P10px for all four Murimotu samples (N=4, Lm scaled), of 3.4 ± 0.8 atoms g^{-1} yr^{-1}, is the best estimate with the lowest uncertainties. Therefore, this is the production rate used to determine exposure ages of the Mount Gran samples. However, while this P10px is lower than P10qtz (Putnam, *et al.,* 2010), they still overlap within error.

4.3 Mount Gran exposure ages

Using the radiocarbon derived ^{10}Be pyroxene production rate of 3.4 ± 0.8 atoms g^{-1} yr^{-1}, exposure ages have been established for the eight cobble erratics, and seven bedrock samples collected on Mount Gran (see *figure 3.3*). The uncertainties are relatively large as a result of the low measured ^{10}Be/^{9}Be ratios and low beryllium yields. Calculating exposure ages using Balco, *et al.* (2008) and Heyman, *et al.* (2014) P10qtz values result in ages that are ~10-20% lower than ages calculated using the P10px-radiocarbon, as higher production rates result in younger exposure ages. However, as a result of the large uncertainties these ages are indistinguishable from those calculated using P10px-radiocarbon. As the cobble and bedrock ages are offset, it suggests the bedrock samples are likely to contain inherited cosmogenic nuclides from previous exposure that have experienced insufficient erosion. The cobble erratics and bedrock samples will be discussed separately.

4.3.1 Bedrock samples

The bedrock exposure ages are older than the cobble erratics suggesting they contain inherited cosmogenic nuclides from a previous episode of exposure. This implies there has been insufficient erosion of the bedrock by glacial ice since prior exposure. However, these samples only exhibit minor inheritance, as the exposure age for the oldest sample is ~65 ka. When compared to exposure ages from other bedrock samples in Antarctica, these exposure ages are very young. For example, Hein, *et al.* (2011) report a ^{10}Be bedrock age of ~1.5 Ma from the Weddell Sea, and Di Nicola, *et*

al. (2009), a ^{10}Be bedrock age of ~1.9 Ma from Terra Nova Bay. This implies either: the bedrock has been deeply-eroded, removing the majority of nuclides from previous exposure; the bedrock experienced minimal recent exposure; or it underwent prolonged burial, allowing for almost complete decay of the previously accumulated ^{10}Be.

The bedrock sampled was polished and striated, with some striations preserved in multiple directions. This suggests there has been minimal erosion during repeated advances beneath the cold-based ice (Naslund, 1998; Atkins, 2013). As cold-based ice deforms internally, rather than sliding along the ice-bed interface, minimal erosion occurs. Thus, we would expect negligible removal of inherited ^{10}Be, resulting in a high exposure age. As there is minimal erosion (based on the preservation of multiple striae directions), this implies that the bedrock must have experienced a short recent exposure, or the bedrock surface has been covered by ice for a long period of time, allowing the majority of inherited cosmogenic ^{10}Be to decay away, leaving few inherited ^{10}Be nuclides in the sample after ice retreat and re-exposure. As the half-life of ^{10}Be is 1.39 Myr (Chmeleff, *et al.*, 2010; Korschinek, *et al.*, 2010), this second scenario would imply long-term burial.

The apparent antiquity of the highly weathered bedrock surface supports the idea that these surfaces have been covered for a long period of time, allowing decay of previously accumulated ^{10}Be (see sample photos in *figure 1.8*). Samples MGW01-05 were collected with the purpose to assess any potential age gradient between minimally and extremely weathered bedrock. Minimally-weathered MGW01 and

MGW02 were collected at a lower elevations in the transect, while extremely weathered MGW04 and MGW05 were collected at a higher elevation. Despite their appearance (*figure 4.2*), the highly weathered bedrock samples have exposure ages similar to, or younger than the minimally weathered samples. For example, MGW04 and MGW05 have exposure ages of less than ~35 ka; while much less weathered surfaces MGW01 and MGW03, have older or similar exposure ages, of ~45 ka and ~30 ka, respectively. Thus, despite the relative differences in weathering, they display similar exposure ages (see *figure 3.3).* This suggests that relative exposure ages cannot be estimated based on weathering characteristics.

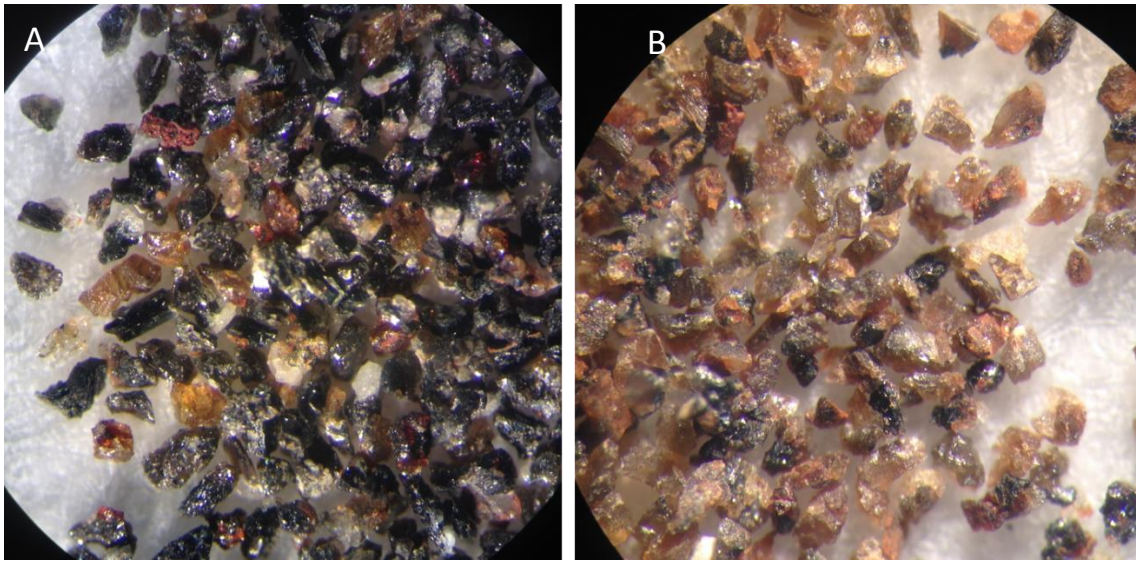

Figure 4.2: Pyroxene viewed down a binocular microscope from MGW01 (A) and MGW05 (B). The pyroxenes in MGW05 are more weathered than the pyroxenes in sample MGW01. However, MGW01 exhibits an older apparent exposure age (of ~45 ka) than MGW05 (of ~31 ka).

4.3.2 Cobble erratics

Plotted against elevation, the exposure ages of the cobble erratics demonstrate the recent thinning of the Mackay Glacier. As the bedrock contains inheritance, it is possible that the cobbles may also have been previously exposed and not sufficiently eroded since last exposure, thus containing inherited ^{10}Be. Based on the 'dipstick' method (Stone, *et al.,* 2003; Mackintosh, *et al.,* 2007; White, *et al.*, 2011), assuming simple glacial thinning, we expect the oldest exposure age to correspond to the rocks at the highest elevation, and vice versa, with the youngest rocks expected at the lowest elevations. Thus, we assume stratigraphic consistency with no exposure age being older than the sample above it. However, as sample MG07 is older, outside of error, than the samples at higher elevations, it is considered an outlier. It is interpreted to contain inherited ^{10}Be from prior-exposure and is therefore excluded from interpretation of the thinning history of Mackay Glacier. Excluding sample MG07, there is a phase of relatively rapid thinning represented at Mount Gran over ~60 m of elevation, with an apparent slowing down (over ~10 m elevation) of thinning rates towards the bottom of the profile. Based on these exposure ages, the rapid thinning occurs ~13.5 - 11 ka, at a rate of approximately 25 m/ka (see figure 3.4).

4.3.3 Mackay Glacier ice surface lowering

As discussed previously, Jones, *et al.* (submitted) recorded ice surface lowering at two nunataks exposed downstream on Mackay Glacier using cosmogenic ^{10}Be in quartz, and propose an onset of rapid thinning at ~8 ka, based on the NZ-based

production rate (Putnam, *et al.,* 2010) and a time-dependant Antarctic scaling scheme (Lm; Stone, *et al.,* 2002). The record obtained at Mount Suess (~15-25 km from the current glacier terminus) was the most complete, and closest record to Mount Gran, thus, this is the site used for comparison. The absence of quartz in the cobble erratics at Mount Gran, had so far prevented a record of ice surface lowering to be obtained at this site (~35 km from the terminus). Now that a record of ice surface lowering has been obtained for the upper Mackay Glacier at Mount Gran (~35 km from the terminus), a comparison can be made for the timing and rates of thinning at this site, with Mount Suess further down-glacier.

The Mackay Glacier started to thin following an advance to its Last Glacial Maximum (LGM) configuration. The most rapid phase of thinning occurred during the early/mid Holocene (~7.8-7.0 ka) when >80% of the LGM-to-present ice loss occurred (Jones, *et al.* submitted). Greater than 180 m of thinning was recorded on the nunataks down-glacier, with rates up to 60 cm/yr, occurring over <800 years. As the climatic conditions were fairly stable by this time, it is most likely that this accelerated ice thinning was not directly associated with external climatic forcing. Sea level rise reduced after 8 ka (Lambeck, *et al.,* 2014), the air temperature was at near present values by ~10 ka (Jouzel, *et al.,* 2007), and there was no significant change in sea-surface temperature (Pahnke & Sachs, 2006). Therefore, it is suggested that the rapid thinning at this time is a result of the grounding line retreating into an over-deepened trough on the inner shelf. The bathymetry of the bed can make the glacier subject to marine-ice-sheet instability (Joughin & Alley, 2011; Mengel & Levermann, 2014). The marine-ice-sheet instability hypothesis is that a glacier cannot have a stable grounding line on a reverse slope bed that becomes deeper inland

(Schoof, 2007). When a grounding line retreats onto a reverse slope, the ice at the grounding line thickens as it is in deeper water, increasing the amount of ice flux, and therefore providing a positive feedback that makes the glacier vulnerable to external forcing, such as basal melting (Pritchard, *et al*., 2012). Thus, a stable grounding line cannot be located on reverse slope bed (Schoof, 2007). The grounding line will continue to retreat until it stabilises on a forward sloping bed. In many locations in Antarctica, the bed steadily deepens towards the centre of the ice sheet, meaning once retreat has begun, there are no forward facing slopes to re-stabilise the grounding line, allowing runaway and potentially irreversible retreat of the glacier (Joughin & Alley, 2011).

As the thinning of the Mackay Glacier occurred from perturbations at the grounding line, it is expected that thinning occurred earlier downstream, and that the upstream sites would record less thinning (Nick, *et al.*, 2009). One of these expectations might be observed at Mount Gran, where ~65 m of rapid thinning is recorded compared to ~180 m recorded at sites downstream (*figure 3.4*), but the onset is not recorded at Mount Gran. However, the rapid thinning at Mount Gran occurs between ~13.5 and 11 ka, which is earlier than the thinning recorded downstream at Mount Suess at ~8-7 ka. At Mount Gran, ~65 m of thinning occurs over ~3.5 ka, producing thinning rates of ~18.5 cm/yr. These thinning rates are much lower than the rates of ~60 cm/yr recorded at Mount Suess (Jones, *et al*. submitted). As the external uncertainties on the Mount Gran samples are relatively large, they overlap within error of the exposure ages for rapid thinning at Mount Suess; thus, thinning could have occurred at the same time at both sites. However, the exposure ages of the top two samples at Mount Gran (MG30 and MG32 – combined to MG32/30) are older, outside of uncertainties,

than the maximum age representing the thinning at Mount Suess. As such, the top two samples at Mount Gran could provide an age estimate of the onset of thinning as it is not recorded at downstream sites. Jones *et al.* (submitted) were not able to confidently determine when the episode of rapid thinning started in most transects; thus, this could provide an important age constraint for the onset of accelerated thinning at Mackay Glacier. However, this needs to be further examined and modelled in order to test if it is statistically significant. These models are discussed in the following two sections.

4.3.4 Mackay Glacier modelling scenarios

R. Jones (pers. comm.) modelled changes in surface elevation over time for two ocean forcing scenarios (1.80 ºC and 1.65 ºC change in temperate) at both Mount Gran and Mount Suess (*figure 4.3*). These simulations predict: 1) only one episode of thinning occurred at both sites; 2) thinning at Mount Gran is more subdued than thinning at Mount Suess; and 3) that accelerated thinning occurred at approximately the same time at Mount Suess and Mt Gran, and possibly delayed by several decades at Mount Gran. These predictions are consistent with the current understanding of outlet glacier dynamics (Howat, *et al*, 2007; Vieli & Nick, 2011; Wouters, *et al.*, 2015). However, these modelled scenarios do not explain why the Mount Gran samples record rapid thinning many hundreds of years prior to Mount Suess. The simplest solution is that the age difference between the two sites reflects the production rate used to determine the exposure ages at Mount Gran. It is possible that the ^{10}Be production rate in pyroxene determined using cross-calibration with the Murimotu radiocarbon age in New Zealand may not be applicable to Antarctica. If

this is the case, then it may indicate that the New Zealand production rates are anomalously low. Alternatively, rapid thinning at Mount Suess could have commenced prior to thinning at Mount Gran, but it may not have been recorded on the nunatak. This scenario is discussed in the following section.

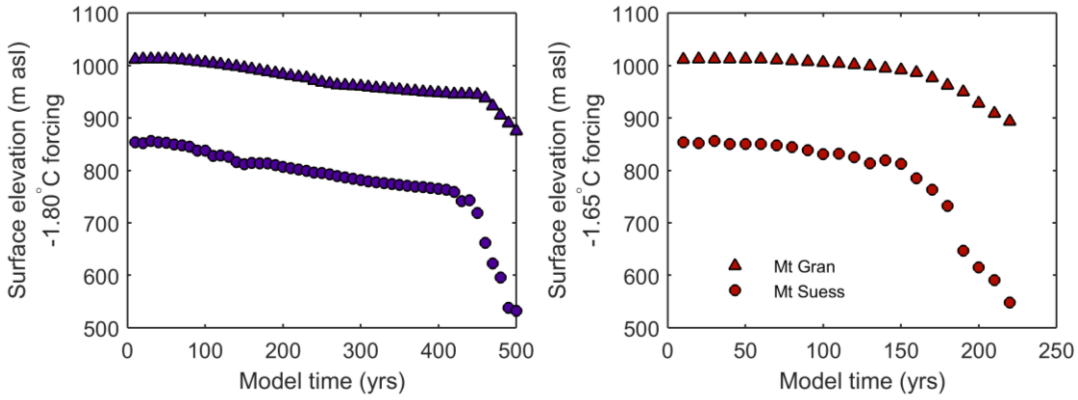

Figure 4.3: Modelled scenarios for ice surface lowering over time at Mount Gran (triangles) and Mount Suess (circles), in response to two oceanic forcing scenarios of 1.80 ºC and 1.65 ºC changes in temperature, on the left and right plots, respectively. Irrespective of the forcing applied, a single phase of accelerated thinning is simulated at both nunataks, which occurs at approximately the same time. Modelling and plots supplied by R. Jones.

4.3.5 OxCal age-elevation modelling

In order to determine the most statistically likely chronology based on stratigraphic position and uncertainties, Bayesian age-elevation modelling using Monte Carlo techniques was carried out on exposure ages from the Mount Gran exposure age transect. A single sequence was run on the OxCal program version 4.2. This program is predominantly used to provide radiocarbon calibration in sediment cores where a

stratigraphic succession is being examined; however it can also be applied for age-elevation modelling of a transect of cosmogenic exposure ages, under the assumption that the higher samples are older as they were exposed to cosmic ray flux from thinning before the lower samples. Cobble erratic MG07 was excluded from the input dataset. The modelled age-elevation output is shown in *table 4.3*, and plotted values are shown in *figure 4.4*. Based on this modelling, using 1 sigma error, the minimum age that thinning began is 11,471 yrs. Thus, it is possible that Mount Gran records an earlier part of the rapid thinning phase that is not recorded at the downstream sites. Because thinning should have occurred first downstream, this minimum age of the top sample exposed at Mount Gran then provides a minimum age constraint for the timing of the earliest rapid thinning of the Mackay Glacier. If this is the case, we can calculate the duration of thinning using the minimum age of the highest sample exposed at Mount Gran, and the maximum age of the lowest sample exposed at the furthest downstream site (Low Ridge). The youngest sample that records the rapid thinning phase at Low Ridge has a modelled age of 7,047 ± 239 yrs (1 sigma error) (R. Jones, pers. comm.). Therefore, the maximum age for the latest thinning occurring is 7,286 yrs. This means that the minimum duration of rapid thinning is 4,185 years. It is unlikely that the rate of thinning remained constant over this duration. As a result of this, a maximum thickness for ice lost during this rapid thinning phase is not appropriate to calculate as a duration and constant thinning rate are needed to determine this.

Table 4.3: OxCal modelled age output for Mount Gran.

	Modelled age (years BP)					
Sample	**1 sigma**		**2 sigma**		**Mean**	**1 stdev**
	from	to	from	to		
MG32	17250	11471	20688	9131	14702	2861
MG30	16003	11042	18740	8875	13719	2447
MG12	14962	10465	17332	8337	12789	2190
MG15	14084	9852	16266	7669	11981	2117
MG19	13256	8855	15278	6714	11025	2147
MG22	12568	7764	14607	5316	10041	2335
MG01	11994	6531	14373	3094	8921	2814

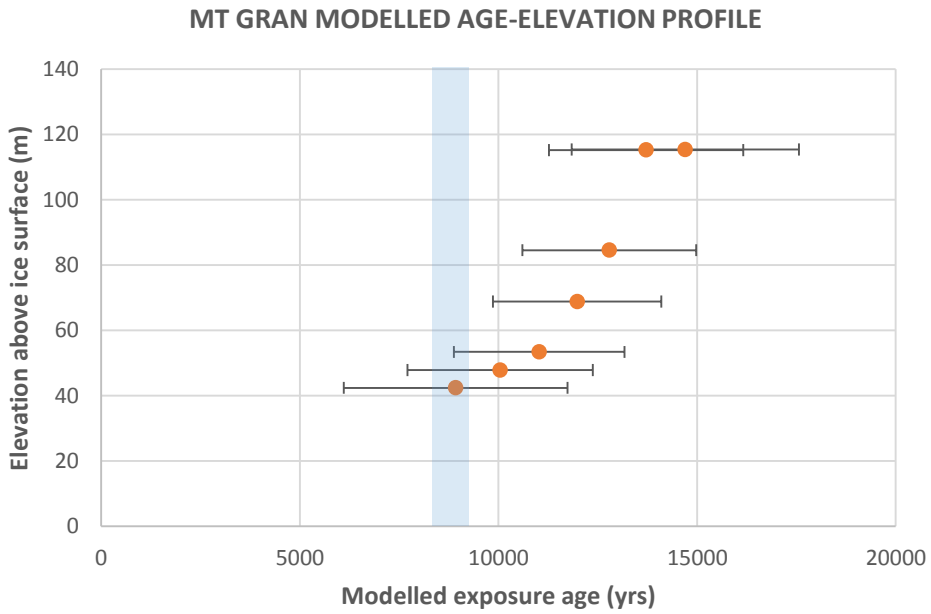

Figure 4.4: Oxcal age-elevation modelled exposure ages for Mount Gran. Mean age and 1 standard deviation errors shown. The shaded blue box represents the timing of the rapid thinning phase at Mount Suess.

4.3.6 Summary of possible scenarios for thinning record at Mount Gran

There are discrepancies between the timing of thinning at Mount Gran compared with sites further down-glacier. Below are some possibilities to explain this.

1. One possible explanation for the older ages at Mount Gran when compared to Mount Suess, are the different production rates used to determine exposure ages at each site. Ages at Mount Gran were calculated using P10px-radiocarbon for New Zealand, while the Mount Suess ages were determined using the NZ P10qtz (Putnam, *et al.*, 2010). However, both of these production rates were consistent within uncertainties in New Zealand. Therefore, any difference in Antarctica may suggest different spatial scaling schemes are required for quartz and pyroxene.

2. If the P10px acceptable to use and the exposure ages are correct, since the Mount Suess sample exposure ages fall within the larger uncertainties of the Mount Gran samples, this may represent the same thinning event. If so, the top samples (MG30 and MG32) of Mount Gran may represent an age prior to rapid thinning as the errors on the age are outside of the maximum timing for the rapid thinning phase (*figure 3.4*).

3. There is a possibility all of the cobble erratics contain inherited cosmogenic ^{10}Be as a result of insufficient erosion via cold-based ice since previous exposure. As the pattern of thinning is the same as in the downstream sites, all samples at Mount Gran would had to have experienced the same duration of

exposure and amount of erosion to contain similar amounts of inherited nuclides, shifting the age of the entire transect to display older exposure ages. While this is possible, it is not likely as ice would tend to cover lower samples and expose upper samples preferentially, and erosion is unlikely to have been uniform over all eight clasts.

4. Based on the OxCal age-elevation modelling, Mount Gran has recorded an earlier part of the rapid thinning phase that has not been recorded in the downstream sites (*figure 4.4*). As thinning would have been occurring downstream first, the minimum age the thinning began is ~11.5ka, recorded in samples MG32/MG30 at the top of the Mount Gran transect. Based on this age, the minimum duration of the rapid thinning phase is ~4 ka. This either implies that the ice was much thicker, or there was possibly ice retreat and advance during this time, with earlier retreat recorded at Mount Gran, followed by advance not captured in the samples, then another phase of rapid thinning recorded at down-glacier sites. However, the modelling of ice surface lowering over time in response to changes in oceanic forcing predicts only one phase of thinning occurred at both sites (*figure 4.3*).

4.4 Chapter summary

To summarise this chapter, further improvements to the leaching and beryllium separation chemistry would decrease the uncertainty in the measured $^{10}Be/^{9}Be$ ratios. Production rates for ^{10}Be in pyroxene are both theoretically and empirically 8-27%

lower than ^{10}Be production rates in quartz, suggesting a lower production rate is valid. The exposure ages for the bedrock samples and cobbles at Mount Gran were calculated using the production rate determined via cross-calibration with the radiocarbon age of the Murimotu debris avalanche, of 3.4 ± 0.8 atoms g^{-1} yr^{-1} (Lm scaled, N=4). The bedrock samples at Mount Gran contain a small amount of inherited nuclides, suggesting the bedrock has been covered by ice for a long duration, allowing the inherited ^{10}Be from prior exposure to almost completely decay away. The exposure ages of the cobble erratics collected at Mount Gran provide a chronology for ice surface lowering of the Mackay Glacier. A period of relatively rapid thinning is recorded from ~13.5 to ~11 ka at this site. This occurs earlier than the rapid thinning recorded at a nunatak down-glacier. Multiple scenarios could explain this age offset; however, I suggest the most appropriate scenario is that Mackay Glacier began rapidly thinning around ~11.5 ka (recorded at Mount Gran), and continued to thin until ~7.2 ka (recorded at Low Ridge down-glacier), based on OxCal age-elevation modelling.

Chapter Five: Conclusion

5.1 Decontamination procedure and separation chemistry

A significant result of this research was the success of the decontamination procedure in removing the meteoric component of ^{10}Be from pyroxene grains. The original decontamination method proposed by Blard, *et al.* (2008), consisted of initially crushing the pyroxene grains to <90 microns to expose the weathering pits, followed by the two leaches in $NH_2OH{\cdot}HCl$ and HCl, and sequential dissolution in 4M HF. This procedure was effective at releasing the grain adsorbed meteoric ^{10}Be into an aqueous phase allowing it to be removed from the mineral, while leaving the *in situ* ^{10}Be remaining in the crystal lattice. Based on the leach test applied to sample JC2, the meteoric ^{10}Be is completely removed after the two leaches and no more than 20% sample dissolution in HF. The samples were then bulk dissolved in concentrated HF and the beryllium separated using cation exchange columns. As pyroxenes have more major cations than quartz, standard separation techniques had to be modified in order to be applied. Column calibration experiments were performed to optimise the cation chemistry for pyroxenes to achieve the best separation of beryllium. Clean separation of beryllium was achieved, and ^{10}Be/^{9}Be ratios were measured by AMS.

As a result of the low beryllium yield produced during chemistry, and the low measured $^{10}Be/^{9}Be$ ratio, large analytical uncertainties (up to 33%) were experienced. Regardless of the small dissolved amounts, the ratios are still a minimum of 3x above the blank value, ensuring the measurements are reliable. The low beryllium yield was a result of the small amount of pyroxene dissolved for *in situ* ^{10}Be measurement, and also a consequence of the beryllium lost during chemistry. As ~4 grams of pyroxene was initially dissolved for the Murimotu and Mount Gran samples, the first dissolution in 4M HF resulted in a total mass loss of 35-82%, leaving as little as 0.73 g of pyroxene remaining to measure the *in situ* ^{10}Be concentration. Additionally, beryllium was lost at an unknown step during chemistry, decreasing the total beryllium for measurement.

Further improvements could be made to the chemistry procedure for meteoric ^{10}Be removal and beryllium isolation. These are suggested below.

- In order to retain more pyroxene after the first HF dissolution step, the volume or molarity of the HF acid used could be decreased as to only dissolve ~20% of each sample.
- Shorter HF rounds could control total mass loss, allowing dissolution of only 20% of each sample during HF1.
- The mass of pyroxene initially dissolved could be increased; however, this would also increase the number of major element cations in the same to remove during chemistry. Initial composition of the pyroxene could be measured by ICP-MS to optimise mass.

- In order to discover which step the beryllium was lost during chemistry, aliquots of each supernate could be measured after each step to find the step at which it was lost.
- To insure beryllium was not lost during the cation exchange columns, larger columns containing larger volumes of resin and acid could be utilized to ensure the resin is not becoming oversaturated with cations, eluting the Be with other elements; however, this will be expensive and time consuming.

5.2 Production rate calibration

A New Zealand production rate calibration site for ^{10}Be in pyroxene has been established using the Murimotu debris avalanche site in the central North Island. The deposit has been previously established as a production rate calibration site for ^{3}He in pyroxene, as the deposit has a well-constrained radiocarbon age (Eaves, *et al.* 2015). Using direct cross-calibration with both the ^{3}He concentration and the radiocarbon age, production rates for ^{10}Be in pyroxene were established. The cross-calibration with the ^{3}He concentration gave P10px of 4.3 ± 2.3 atoms g^{-1} yr^{-1} (Lm scaling), and 3.3 ± 1.1 atoms g^{-1} yr^{-1} excluding sample MM-12-03 (N=3). The production rates determined via cross-calibration with radiocarbon are comparable or lower, with a P10px of 3.4 ± 0.8 atoms g^{-1} yr^{-1} for N=4 (Lm scaled) and 2.8 ± 0.7 atoms g^{-1} yr^{-1} (N=3). The average ^{3}He/^{10}Be ratio was also determined because the ^{3}He/^{10}Be ratios should stay a constant value, even if the absolute production rates for the nuclides change. For the Murimotu pyroxene, the average ^{3}He/^{10}Be ratio is 34.5 ± 9.9. This is

indistinguishable from global estimates of ^{3}He-pyroxene/^{10}Be-quartz, suggesting that the ^{10}Be concentration measured in the pyroxene is reliable.

Additionally, theoretical production rates were determined based on the composition of the Murimotu pyroxene. The theoretical P10px were calculated using elemental production rates determined by Kober, *et al.* (2005) and Masarik (2002), which gave average ^{10}Be production rates of 4.16 atoms g^{-1} yr^{-1}, and 4.62 atoms g^{-1} yr^{-1}, respectively. As the absolute precision of elemental production rates are unknown, theoretical production rates for ^{10}Be in quartz were also determined using these elemental production rates. Regardless of the absolute values, the ratio of ^{10}Be production in quartz and pyroxene should remain constant. The theoretical ^{10}Be production rate in the Ruapehu pyroxene is ~17-18% lower than the ^{10}Be production rate in quartz. Comparing the empirical ^{10}Be production rates in pyroxene determined using the Murimotu debris avalanche to production rates of ^{10}Be in quartz, there is an 8-27% reduction. This is in agreement with the theoretical calculations suggesting that a lower production rate should be used for ^{10}Be in pyroxene. As the P10px is shown to be both theoretically and empirically lower than production rates in quartz, the radiocarbon-derived P10px (for N=4, Lm scaled), of 3.4 ± 0.8 atoms g^{-1} yr^{-1}, is the best estimate with the lowest uncertainties.

5.3 Mount Gran exposure ages

The decontamination procedure and determined P10px-radiocarbon were then applied to exposure date polished and striated bedrock samples and cobble erratics collected

on a vertical transect on Mount Gran, adjacent to the upper Mackay Glacier in Southern Victoria Land, Antarctica. Based on the cobble erratics, a chronology for ice surface lowering could be determined using the 'dipstick' method. Assuming simple glacial thinning, the samples exposed at higher elevations should have higher ^{10}Be concentrations and subsequently older exposure ages. The bedrock samples exhibit ages older than the cobble erratics collected at the same elevation suggesting the bedrock contains inherited nuclides from previous exposure to cosmic rays. The cobble erratics are more likely to represent ice surface lowering, and show a phase of relatively rapid thinning of ~60 m between ~13.5 and 11 ka.

These ages are somewhat older when comparing the timing of this phase of rapid thinning to an ice surface lowering chronology established at a nunatak (Mount Suess) down-glacier by Jones, *et al.* (submitted). At Mount Suess, ~180 m of ice surface lowering occurred over <800 years during an episode of rapid thinning from ~7.8-7 ka. The thinning of the glacier was synchronous with the retreat of the grounding-line into an over-deepened trough. Based on glacial dynamics, a perturbation at the grounding line would result in thinning occurring down-glacier earlier than the response further inland. I have suggested multiple scenarios that could cause this result, these are:

- The production rate used to calculate the exposure ages may not be applicable to Antarctica.

- The uncertainties on the Mount Gran samples overlap with the phase of rapid thinning occurring at Mount Suess; thus, the Mount Gran ages could represent the same thinning event.
- All cobble erratics collected at Mount Gran could contain inherited ^{10}Be from insufficient erosion since prior exposure. However, this is unlikely.
- Based on the OxCal modelling, Mount Gran could record an earlier part of the rapid thinning phase that was not recorded at Mount Suess. This would mean Mackay Glacier has been thinning since ~11.5 ka, over a minimum duration of ~4 ka.

Currently there is no definitive answer to explain the offset in the timing of thinning occurring at Mount Gran and down-glacier at Mount Suess. Further sampling and modelling would be required to complete the understanding of the timing and rates of thinning occurring on Mackay Glacier.

To conclude, the success of the meteoric ^{10}Be decontamination procedure, and the establishment of a calibration site for ^{10}Be in pyroxene, provide promising results for the future of the chronometer. With further developments in enhancing the dissolution and separation chemistry, ^{10}Be could become a routinely measured nuclide alongside ^{3}He in pyroxene to allow complex exposure histories to be determined. The application of the ^{10}Be production rate in pyroxene determined via cross calibration with radiocarbon at the Murimotu debris avalanche site needs further testing to ensure it is applicable to Antarctica. Nonetheless, this study was successful in proving that meteoric ^{10}Be can be effectively removed from pyroxene, allowing an *in situ* ^{10}Be concentration to be measured. Additionally, productions rates were able

to be determined for ^{10}Be in pyroxene in New Zealand, which are both theoretically and empirically ~8-27% lower than production rates in quartz. The application of the determined ^{10}Be pyroxene production rate to samples collected on Mount Gran, produces a sensible ice surface lowering chronology for Mackay Glacier, similar to what has been observed downstream.

References

Ackert, R., Barclay, D., Borns Jr, H., Calkin, P., Kurtz, M., Fastook, J., & Steig, E. (1999). Measurements of past ice sheet elevations in interior West Antarctica. *Science, 286*, 276-280.

Anderson, J. B., Conway, H., Bart, P. J., Witus, A. E., Greenwood, S. L., McKay, R. M., Hall, B. L., Ackert, R. P., Licht, K., Jakobsson, M., and Stone, J. O. (2014). Ross Sea paleo-ice drainage and deglacial history during and since the LGM. *Quaternary Science Reviews*, 1-24.

Amidon, W., Rood, D., & Farley, K. (2009). Cosmogenic ^{3}He and ^{21}Ne production rates calibrated against ^{10}Be in minerals from the Coso volcanic field. *Earth and Planetary Science Letters, 280*, 194-204.

Atkins, C. (2013). Geomorphological evidence of cold-based glacier activity in South Victoria Land, Antarctica. *The Geological Society of London*, 299-318.

Balco, G. (2011). Contributions and unrealized potential contributions of cosmogenic-nuclide exposure dating to glacier chronology, 1990-2010. *Quatermary Science Reviews, 30*, 3-27.

Balco, G., J.M., S., & group, L. (2013). Exposure-age record of Holocene ice sheet and ice shelf change in the northeast Antarctic Peninsula. *Quaternary Science Reviews, 59*, 101-111.

Balco, G., Stone, J., Lifton, N., & Dunai, T. (2008). A complete and easily accessible means of calculating surface exposure ages or erosion rates from ^{10}Be and ^{26}Al measurements . *Quaternary Geochronology, 3*, 174-195.

Bard, E. (1998). Geochemical and geophysical implications of the radiocarbon calibration. *GEOCHIMICA ET COSMOCHIMICA ACTA, 62*, 2025-2038.

Benedetti, L. F., Papanastassiou, D., King, G., Amijo, R., Ryerson, F., Farber, D., & Flerit, F. (2002). Post-glacial slip history of the Sparta fault (Greece) determined by ^{36}Cl cosmogenic dating: Evidence for non-periodic earthquakes. *Gephysical Reseach Letters, 29*, 1-4.

Bentley, M. (1999). Volume of Antarctic Ice at the Last Glacial Maximum, and its impact on global sea level change. *Quaternary Science Reviews, 18*, 1569-1595.

Bentley, M., The RAISED Consortium, O Cofaigh, C., Anderson, J., Conway, H., Davies, B., Graham, A.G.C., Hillenbrand, C.D. Hodgeson, D.A., Jamieson, S.S.R., Larter, R.D., Mackintosh, A., Smith, J.A., Verleyen, E., Ackert, R.P., Bart, P.J., Berg, S., *et al* (2014). A community-based geological reconstruction of Antarctic Ice Sheet deglaciation since the Last Glacial Maximum. *Quaternary Science Reviews, 100*, 1-9.

Bentley, M., Fogwill, C., Kubik, P., & Sugden, D. (2006). Geomorphological evidence and cosmogenic ^{10}Be/^{26}Al exposure ages for the Last Glacial Maximum and deglaciation of the Antarctic Peninsula Ice Sheet. *Geological Society of America*, 1149-1159.

Bentley, M., Fogwill, C., Le Brocq, A., Hubbard, A., Sugden, D., Dunai, T., & Freeman, S. (2010). Deglacial history of the West Antarctic Ice Sheet in the

Weddell Sea embayment: Constraints on past ice volume change. *Geology, 38*, 411-414.

Bierman, P. (1994). Using in siti produced cosmogenic isotopes to estimate rates of landscape evolution: A review from the geomorphic perspective. *Journal of Geophysical Research, 99*, 13,885- 13,896.

Blard, P., Bourles, D., Pik, R., & Lave, J. (2008). In situ cosmogenic ^{10}Be in olivines and pyroxenes. *Quaternary Geochronology*, 196-205.

Blard, P., Braucher, R., Lave, J., & Bourles, D. (2013). Cosmogenic ^{10}Be production rate calibrated against ^{3}He in the high Tropical Andes (3800-4900 m, 20-22 ° S). *Earth and Planetary Science Letters, 382*, 140-149.

Braucher, R., Merchel, S., Borgomano, J., Bourles, D. (2011). Production of cosmogenic radionuclides at great depth: A multi element approach. *Earth and Planetary Science Letters, 309*, 1-9.

Brook, E., Kurtz, M., Ackert, R., Rasibeck, G., & Yiou, F. (1995). Cosmogenic nuclide exposure ages and glacial history of late Quaternary Ross Sea drift in McMurdo Sound, Antarctica. *Earth and Planetary Science Letters, 131*, 41-56.

Brown, E., Edmond, J., Raisbeck, G., Yiou, F., Kurtz, M., & Brook, E. (1991). Examination of surface exposure ages of Antarctic moraines using in situ produced ^{10}Be and ^{26}Al. *Geochemica et Cosmochemica Acta, 55*, 2269-2283.

Brown, L., Klein, J., Middleton, R., Sachs, I., & Tera, F. (1982). ^{10}Be in island-arc volcanoes and implications for subduction. *Nature, 299*, 718-720.

Cerling, T., & Craig, H. (1994). Geomorphology and in situ cosmogenic isotopes. *Annual Reviews Earth Planetary Science*, 273-317.

Chmeleff, J., von Blankenburg, F., Kossert, K., & Jakob, D. (2010). Determination of the ^{10}Be half-life by multicollector ICP-MS and liquid scintillation counting. *Nuclear Instruments and Methods in Physics Research B*, 192-199.

Clark, P., & Mix, A. (2002). Ice sheets and sea level of the Last Glacial Maximum. *Quaternary Science Reviews, 21*, 1-7.

Clark, P., Dyke, A., Shakun, J., Carlson, A., Clark, J., Wohlfarth, B., Mitrovica, J., Hostetler, S., & McCabe, A. (2009). The Last Glacial Maximum. *Science, 325*, 710-714.

Conway, H., Hall, B., Denton, G., Gades, A., & Waddington, E. (1999). Past and Future Grounding-Line Retreat of the West Antarctic Ice Sheet. *Science, 286*, 280-283.

Cuffey, K., Conway, H., Gades, A., Halley, B., Lorrain, R., Severinghaus, J., Steig, E., Vaughn, B., & White, J. (2000). Entrainment at cold glacier beds. *Geology, 28*, 351-354.

Darvill, C. (2013). Cosmogenic nuclide analysis. *British Society for Geomorphology*, 1-25.

Denton, G. (2011). East Antarctic retreat. *Nature Geoscience, 4*, 135-136.

Denton, G., & Hughes, T. (2002). Reconstructing the Antarctic Ice Sheet at the Last Glacial Maximum. *Quaternary Science Reviews, 21*, 193-202.

Desilets, D., Zreda, M., & Prabu, T. (2006). Extended scaling factors for in situ cosmogenic nuclides: New measurements at low latitude. *Earth and Planetary Science Letters, 246*, 265-276.

Di Nicola, L., Strasky, S., Schlucter, C., Salvatore, M., Akcar, N., Kubik, P., Christl, M., Kasper, H., Wieler, R., & Baroni, C. (2009). Multiple cosmogenic nuclides document complex Pleistocene exposure history of glacial drifts in Terra Nova Bay (northern Victoria Land, Antarctica). *Quaternary Research, 71*, 83-92.

Douglass, D., Singer, B., Kaplan, M., Mickelson, D., & Caffee, M. (2006). Cosmogenic nuclide surface exposure dating of boulders on last-glacial and late-glacial moraines, Lago Buenos Aires, Argentina: Interpretive strategies and paleoclimate implications. *Quaternary Geochronology, 1*, 43-58.

Dunai, T. (2001). Influence of secular variation of the magnetic field on production rates of in situ produced cosmogenic nuclides. *Earth and Planetary Science Letters, 193*, 197-212.

Dunai, T. (2010). *Cosmogenic Nuclides : Principles, Concepts and Applications in the Earth Surface Sciences.* Cambridge: Cambridge University Press.

Dunai, T., & Lifton, N. (2014). The nuts and bolts of cosmogenic nuclide production. *Elements, 10*, 347-350.

Dunne, J., Elmore, D., & Muzikar, P. (1999). Scaling factors for the rates of production of cosmogenic nuclides for geometric shielding and attenuation at depth on sloped surfaces. *Geomorphology, 27*, 3-11.

Eaves, S., Winckler, G., Schaefer, J., Vandgergoes, M., Alloway, B., Mackintosh, A.N., Townsend, D.B., Ryan, M.T., & Li, X. (2015). A test of the cosmogenic ^{3}He production rate in the south-west Pacific (39°S) . *Journal of Quaternary Science , 30*, 79-87.

Fabel, D., Stroeven, A., Harbor, J., Kleman, J., Elmore, D., & Fink, D. (2002). Landscape preservation under Fennoscandian ice sheets determined from in situ produced ^{10}Be and ^{26}Al. *Earth and Planetary Science Letters, 201*, 397-406.

Fenton, C., Niedermann, S., Goethals, M., Schneider, B., & Wijbrans, J. (2009). Evaluation of cosmogenic ^{3}He and ^{21}Ne production rates in olivine and pyroxene from two Pleistocene basalt flows, western Grand Canyon, AZ, USA. *Quaternary Geochronology, 4*, 475-462.

Fitfield, L. (2000). Advances in accelerator mass spectrometry. *Nuclear Instruments and Methods in Physics Research Section B: Beam Interactions with Materials and Atoms, 172,* 134-143.

Fretwell, P., Pritchard, H. D., Vaughan, D. G., Bamber, J.L., Barrand, N. E., Bell, R., Bianchi, C., Bingham, R. G., Blankenship, D. D., Casassa, G., Catania, G., Callens, D., Conway, H., Cook, A. J., Corr, H. F. J., Damaske, D., Damm, V., Ferraccioli, F., Forsberg, R., Fujita, S., Gim, Y., Gogineni, P., Griggs, J.A., Hindmarsh, R.C.A., Holmlund, P., Holt, J.W., Holmlund, P., Holt, J. W., Jacobel, R. W., Jenkins, A., Jokat, W., Jordan, T., King, E. C., Kohler, J., Krabill, W., Riger-Kusk, M., Langley, K. A., Leitchenkov, G., Leuschen, C., Luyendyk, B. P., Matsuoka, K., Mouginot, J., Nitsche, F. O., Nogi, Y., Nost, O. A., Popov, S. V., Rignot, E., Rippin, D. M., Rivera, A., Roberts, J., Ross, N., Siegert, M. J., Smith, A. M., Steinhage, D., Studinger, M., Sun, B., Tinto, B. K., Welch, B. C., Wilson, D., Young, D. A., Xiangbin, C., & Zirizzotti, A. (2013). Bedmap2: improved ice bed, surface and thickness datasets for Antarctica. *The Crysosphere, 7*, 375-393.

Gamble, J., Price, R., Smith, I., McIntosh, W., & Dunbar, N. (2003). $^{40}Ar/^{39}Ar$ geochronology of magmatic activity, magma flux and hazards at Ruapehu volcano, Taupo Volcanic Zone, New Zealand. *Journal of Volcanology and Geothermal Research, 120*, 271-287.

Goehring, B., Kurz, M., G., B., Shaefer, J., Licciardi, J., & Lifton, N. (2010). A reevaluation of in situ cosmogenic ^{3}He production rates. *Quaternary Geochronolohgy, 5*, 410-418.

Golledge, N., Fogwill, C., Mackintosh, A., & Buckley, K. (2012). Dynamics of the last glacial maximum Antarctic ice-sheet and its response to ocean forcing. *PNAS, 109*, 16052–16056.

Golledge, N., Levy, R., Mackay, R., Fogwill, C., White, D., Graham, A., Smith, J.A., Hillenbrand, C.D., Licht, K.J., Denton, G.H., Ackert, R.P., Maas, S.M., & Hall, B.L. (2013). Glaciology and geological signature of the Last Glacial Maximum Antarctic ice sheet. *Quaternary Science Reviews, 78*, 225-247.

Gosse, J., & Phillips, F. (2001). Terrestrial in situ cosmogenic nuclides: theory and application . *Quaternary Science Reviews , 20*, 1475-1560.

Granger, D., & Muzikar, P. (2001). Dating sediment burial with in situ-produced cosmogenic nuclides: theory, techniques, and limitations. *Earth and Planetary Science Letters, 188*, 269-281.

Granger, D., Kirchner, J., & Finkel, R. (1996). Spatially Averaged Long-Term Erosion Rates Measured from in Situ-Produced Cosmogenic Nuclides in Alluvial Sediment. *The Journal of Geology, 104*, 249-257.

Hackett, W. (1985). Geology and Petrology of Ruapehu Volcano and Related Vents. Wellington: *P.h.D Thesis: Victoria University of Wellington* .

Hackett, W., & Houghton, B. (1989). A facies model for a Quaternary andesitic composite volcano:. *Bulletin of Volcanology*, 51-68.

Hein, A., Fogwill, C., Sugden, D., & Xu, S. (2011). Glacial/interglacial ice-stream stability in the Weddell Sea embayment, Antarctica. *Earth and Planetary Science Letters, 307*, 211-221.

Heyman, J. (2014). Paleoglaciation of the Tibetan Plateau and surrounding mountains based on exposure ages and ELA depression estimates. *Quaternary Science Reviews, 91*, 30-41.

Howat, I., Joughin, I., & Scambos, T. (2007). Rapid Changes in Ice Discharge from Greenland Outlet Glaciers. *Science, 315*, 1559-1561.

Ivy-Ochs, S., Kerschner, H., & Schluchter, C. (2007). Cosmogenic nuclides and the dating of Lateglacial and Early Holocene glacier variations: The Alpine perspective. *Quaternary International* , 53-63.

Ivy-Ochs, S., Kubik, P., Masarik, J., Wieler, R., Bruno, L., & Schluchter, C. (1998). Preliminary results on the use of pyroxene for ^{10}Be surface exposure dating . *Paul Scherrer Institut: Scientific Report 1998 - Particles and Matter, 1*, 169.

Ivy-Ochs, S., Poschinger, A., Synal, H., & Maisch, M. (2009). Surface exposure dating of the Flims landslide, Graubünden, Switzerland. *Geomorphology, 103*, 104-112.

Ivy-Ochs, S., Schluchter, C., Kubik, P., & Denton, G. (1999). Moraine Exposure Dates Imply Synchronous Younger Dryas Glacier Advances in the European Alps and in the Southern Alps of New Zealand. *Geografiska Annaler, 81*, 313-323.

Jamieson, S., Sugden, D., & Hulton, N. (2010). The evolution of the subglacial landscape of Antarctica. *Earth and Planetary Science Letters, 293*, 1-27.

Jamieson, S., Vieli, A., Livingstone, S., O'Cofaigh, C., Stokes, C., Hillenbrand, C., & J.A., D. (2012). Ice-stream stability on a reverse bed slope. *Nature Geoscience*, 799-802.

Johnson, J., Bentley, M., & Gohl, K. (2010). First exposure ages from the Amundsen Sea Embayment, West Antarctica: The Late Quaternary context for recent thinning of Pine Island, Smith, and Pope Glaciers. *Geology, 36*, 223-226.

Johnson, J., Bently, M., Smith, J., Finkel, R., Hood, D., Gohl, K., Balco, G., Larter, R., & Scaefer, J. (2014). Rapid Thinning of Pine Island Glacier in the Early Holocene. *Science, 343*, 999-1001.

Jones, R., Mackintosh, A., Norton, K., Golledge, N., Fogwill, J., & Kubik, P. (submitted). Rapid thinning of an East Antarctic outlet glacier during stable Holocene climate.

Joughin, I., & Alley, R. (2011). Stability of the West Antarctic ice sheet in a warming world. *Nature Geosciences, 4*, 506-513.

Jouzel, J., Masson-Delmotte, M., Cattani, O., Deyfus, O., Falourd, S., Hoffmann, G., Minster, B., Nouet, J., Barnola, M., Chappellaz, J., Fischer, H., Gallet, J., Johnsen, S., Leuenberger, M., Loulergue, L., Luethi, D., Oerter, H., Parrenin, F., Raisbeck, G., Raynaud, D., Schilt, A., Schwander, S., Selmo, E., Souchez, R., Spahni, R., Stauffer, B., Steffensen, J., Stenni, B., Stocker, T., Tison, J., Werner, M., & Wolff, E. (2007). Orbital and Millennial Antarctic Climate Variability over the Past 800,000 Years. *Science, 317*, 793-796.

Kober, F., Ivy-Ochs, S., Leya, I., Baur, H., Magna, T., Wieler, R., & Kubik, P. (2005). In situ cosmogenic ^{10}Be and ^{21}Ne in sanidine and in situ cosmogenic ^{3}He in Fe–Ti-oxide minerals. *Earth and Planetary Science Letters, 236*, 404-418.

Kohl, C., & Nishiizumi, K. (1992). Chemical isolation of quartz for measurement of in-situ -produced cosmogenic nuclides. *Geochemica et Cosmochemica Acta, 56*, 3583-3587.

Korschinek, G., Bergmaier, A., Faestermann, T., Gerstmann, U., Knie, K., Rugel, G., Wallner, A., Dillmann, I., Dollinger, G., Lierse von Gostomski, C., Kossert, K., Poutivtsev, M. & Remmert, A. (2010). A new value for the half-life of ^{10}Be by Heavy-Ion Elastic Recoil Detection. *Nuclear Instruments and Methods in Physics Research B, 268*, 187-191.

Kubik, P., & Ivy-Ochs, S. (2004). A re-evaluation of the 0–10 ka ^{10}Be production rate for exposure dating obtained from the Köfels (Austria) landslide. *Nuclear Instruments and Methods in Physics Research Section B, 223*, 618-622.

Kurtz, M. D. (1986). Cosmogenic helium in a terrestrial igneous rock. *Nature, 320*, 435-439.

Lal, D. (1988). In situ-produced cosmogenic isotopes in terrestrial rocks. *Annual Reviews Earth Planetary Science, 16*, 355-388.

Lal, D. (1991). Cosmic ray labeling of erosion surfaces: in situ nuclide production rates and erosion models. *Earth and Planetary Science Letters, 104*, 424-439.

Lambeck, K., Rouby, H., Purcell, A., Sun, Y., & Sambridge, M. (2014). Sea level and global ice volumes from the Last Glacial aximum to the Holocene. *PNAS, 111*, 15296-15303.

Leya, I., Lange, H., Neumann, S., Wieler, R., & Michel, R. (2000). The production of cosmogenic nuclides in stony meteoroids by galactic cosmic-ray particles. *Meteorites and Planetary Science, 35*, 259-286.

Lifton, N., Bieber, J., Clem, J., Duldig, M., Evenson, P., Humble, J., & Pyle, R. (2005). Addressing solar modulation and long-term uncertainties in scaling secondary cosmic rays for in situ cosmogenic nuclide applications. *Earth and Planetary Science Letters, 239*, 140-161.

Lilly, K., Fink, D., Fabel, D., & Lambeck, K. (2010). Pleistocene dynamics of the interior East Antarctic ice sheet. *The Geological Society of America, 38*, 703-706.

Lloyd Davies, M., Atkins, C., van der Meer, J., Barrett, P., & Hicock, S. (2009). Evidence for cold-based glacial activity in the Allan Hills, Antarctica. *Quaternary Science Reviews, 28*, 3124-3137.

Mackintosh, A., Golledge, N., Domack, E., Dunbar, R., Leventer, A., White, D. Pollard, D., DeConto, R., Fink, D., Zwartz, D., Gore, D., & Lavoire, C. (2011). Retreat of the East Antarctic ice sheet during the last glacial termination. *Nature Geoscience, 4*, 195-205.

Mackintosh, A., Verleyen, E., O'Brien, P., White, D., Jones, R., Mackay, R., McKay, R., Dunbar, R., Gore, D. B., Fink, D., Post, A. L., Miura, H., Leventer, A., Goodwin, I., Hodgson, D. A., Lilly, K., Crosta, X., Golledge, N. R., Wagner, B., Berg, S., van Ommen, T., Zwartz, D., Roberts, S. J., Vyverman, W., & Masse, G. (2014). Retreat history of the East Antarctic Ice Sheet since the Last Glacial Maximum. *Quaternary Science Reviews*, 10-30.

Mackintosh, A., White, D., Fink, D., Gore, D., Pickard, J., & Fanning, P. (2007). Exposure ages from mountain dipsticks in Mac. Robertson Land East Antarctica, indicate little change in ice-sheet thickness since the Last Glacial Maximum. *The Geological Society of America, 35*, 551-554.

Mackintosh, A., White, D., Fink, D., Gore, D., Pickard, J., & Fanning, P. (2007). Exposure ages from mountain dipsticks in Mac. Robertson Land, East Antarctica, indicate little change in ice-sheet thickness since the Last Glacial Maximum. *The Geological Society of America*, 551-554.

Masarik, J. (2002). Numerical simulation of in situ production of cosmogenic nuclides. *Geochemica Cosmochemica Acta*.

Masarik, J., & Beer, J. (1999). Simulation of particle fluxes and cosmogenic nuclide production in the Earth's atmosphere. *Journal of Geophysical Reseach, 104*, 12099-12111.

Masarik, J., & Beer, J. (2009). An updated simulation of particle fluxes and cosmogenic nuclide production in the Earth's atmosphere. *Journal of Geophysical Research, 114*, 1-9.

Masarik, J., & Reedy, R. (1995). Terrestrial cosmogenic-nuclide production systematics calculated from numerical simulations. *Earth and Planetary Science Letters , 136*, 381-395.

McArthur, J., & Shepherd, M. (1990). Late Quaternary glaciation of Mt Ruapheu, North Island, New Zealand. *Journal of the Royal Society of New Zealand*, 287-296.

Mecer, J. (1978). West Antarctic ice sheet and CO2 greenhouse effect: a threat of disaster. *Nature*(271), 321-324.

Mengel, M., & Levermann, A. (2014). Ice plug prevents irreversible discharge from East Antarctica. *Nature Climate Change, 4*, 451-455.

Milne, G., Mitrovica, J., & Schrag, D. (2002). Estimating past continental ice volume from sea-level data. *Quaternary Science Reviews, 21*, 361-376.

Mirksy, A., Treves, S., & Calkin, P. (1965). *Stratigraphy and Petrography, Mount Gran Area, Southern Victoria Land, Antarctica.* . American Geophysical Union.

Monaghan, M., Klein, J., & Measures, C. (1988). The origin of ^{10}Be in island-arc volcanic rocks. *Earth and Planetary Science Letters, 89*, 288-298.

Morris, J., Gosse, J., Brachfeld, S., & Tera, F. (2002). Cosmogenic Be-10 and the Solid Earth: Studies in Geomagnetism, Subduction Zone Processes, and Active Tectonics. *Reviews in Mineralogy and Geochemistry*, 207-270.

Nakada, M., & Lambeck, K. (1989). The melting history of the late Pleisticene Antarctic ice sheet. *Nature, 333*, 36-40.

Naslund, J. (1998). Subglacial Preservation of Valley Morphology at Amundsenisen, Western Dronning Maud Land, Antarctica. *Earth Surface Processes and Landforms, 22*, 441-455.

Nick, F., Vieli, A., Howat, I., & Joughin, I. (2009). Large-scale changes in Greenland outlet glacier dynamics triggered at the terminus. *Nature Geoscience, 2*, 110-113.

Nishiizumi, K., Imamura, M., Caffee, M., Southon, J., & Finkel, R. M. (2007). Absolute calibration of 10Be AMS standards. *Nuclear Instruments and Methods in Physics Research B, 258*, 403-413.

Nishiizumi, K., Klein, J., Middleton, R., & Craig, H. (1990). Cosmogenic ^{10}Be, ^{26}Al,and ^{3}He in olivine from Maui lavas . *Earth and Planetary Science Letters*, 263-266.

Nishiizumi, K., Kohl, C., Arnold, J., Klein, J., Fink, D., & Middleton, R. (1991). Cosmic ray produced ^{10}Be and ^{26}Al in Antarctic rocks exposure and erosion history. *Earth and Planetary Science Letters, 104*, 440-454.

Nishiizumi, K., Lal, D., Klein, J. M., & Arnold, J. (1986). Production of ^{10}Be and ^{26}Al by cosmic rays in terrestrial quartz in situ and implications for erosion rates. *Nature, 319*, 134-136.

Nishiizumi, K., Winterer, E., Kohl, C., Klein, J., Middleton, R., Lal, D., & Arnold, J. (1989). Cosmic ray production rates of ^{10}Be and ^{26}Al in quartz from glacially polished rocks. *Journal of Geophysical Research, 98*, 17909-17915.

Norton, K., von Blanckenburg, F., Schlunegger, F., Schwab, M., & Kubik, P. (2008). Cosmogenic nuclide-based investigation of spatial erosion and hillslope channel coupling in the transient foreland of the Swiss Alps. *Geomorphology, 95*, 474-786.

Pahnke, K., & Sachs, J. (2006). Sea surface temperatures of southern midlatitudes 0–160 kyr BP. *Paleoceanography, 21*, 1-17.

Palmer, B., & Neall, V. (1989). The Murimotu Formation-9500 year old deposits of a debris avalanche and associated lahars, Mount Ruapehu, North Island, New Zealand. *New Zealand Journal of Geology and Geophysics, 32*, 477-486.

Palumbo, L., Benedetti, L., Bourles, D., Cinque, A., & Finkel, R. (2004). Slip history of the Magnola fault (Apennines, Central Italy) from ^{36}Cl surface exposure

dating: evidence for strong earthquakes over the Holocene. *Earth and Planetary Science Letters, 30*, 163–176.

Peltier, W. (2002). On eustatic sea level history: Last Glacial Maximum to Holocene. *Quaternary Science Reviews, 21*, 377-396.

Phillips, F., Zreda, M., & Flinsch, M. (1996). A reevaluation of cosmogenic ^{36}Cl production rates in terrestrial rocks. *Geophysical research letters, 23*, 949-952.

Pollard, D., & DeConto, R. (2009). Modelling West Antarctic ice sheet growth and collapse through the past five million years. *Nature, 458*, 329-323.

Price, R., Gamble, J., Smith, I., Maas, R., Waight, T., Stewart, R., & Woodhead, J. (2012). The Anatomy of an AndesiteVolcano: a Time Stratigraphic Study of Andesite Petrogenesis and Crustal Evolution at RuapehuVolcano, New Zealand. *Journal of Petrology, 0*, 1-51.

Pritchard, H., Lightenberg, S., Frinker, H., Vaughan, D., van den Broeke, M., & Padman, L. (2012). Antarctic ice-sheet loss driven by basal melting of ice shelves. *Nature, 484*, 502-505.

Putkonen, J., & Swanson, T. (2003). Accuracy of cosmogenic ages for moraines. *Quaternary Research, 59*, 255-261.

Putnam, A. E., Schaefer, J., Barrel, D., Vandergoes, M., Denton, G., Kaplan, M., Finkel, R.C, Schwartz, R., Goering, B.M., & Kelley, S. (2010). In situ cosmogenic ^{10}Be production-rate calibration from the Southern Alps, New Zealand. *Quaternary Geochronolgy*, 392-409.

Rinterknecht, V., Clark, P., Raisbeck, G., Yiou, F., Bitinas, A., Brook, E., Marks, L., Zelcs, V., Lunkka, J.P., Pavloskaya, I.E., Piotrowski, J.A., & Raukas, A.

(2006). The Last Deglaciation of the Southeastern Sector of the Scandinavian Ice Sheet. *Science, 311*, 1449-1452.

Schaefer, J., & Lifton, N. (2007). Cosmogenic Nuclide Dating: Methods. *Encyclopedia of Quaternary Science* , 412-419.

Schaller, M., von Blanckenburg, F., Veldkamp, A., Tebbens, L., Hovius, N., & Kubik, P. (2002). A 30 000 yr record of erosion rates from cosmogenic ^{10}Be in Middle European river terraces. *Earth and Planetary Science Letters, 204*, 307-320.

Schaller, M., von Blankenburg, F., Hovius, N., & Kubik, P. (2001). Large-scale erosion rates from in situ-produced cosmogenic nuclides in European river sediments. *Earth and Planetary Science Letters, 188*(3-4), 441-458.

Schildgen, T., Phillips, W., & Purves, R. (2005). Simulation of snow shielding corrections for cosmogenic nuclide surface exposure studies. *Geomorphology, 64*, 67-85.

Schlagenhauf, A., Manighetti, I., Benedetti, L., Gaudemer, Y., Finkel, R., Malavielle, J., & Pou, K. (2011). Earthquake supercycles in Central Italy, inferred from ^{36}Cl exposure dating. *Earth and Planetary Science Letters, 307*, 487-500.

Schoof, C. (2007). Ice sheet grounding line dynamics: Steady states, stability, and hysteresis. *Journal of Geophysical Research, 112*, 1-19.

Staiger, J., Gosse, J., Little, E., Utting, D., Finkel, R., Johnson, J., & Fastook, J. (2006). Glacial erosion and sediment dispersion from detrital cosmogenic nuclide analyses of till. *Quaternary Geochronology, 1*, 29-42.

Stone, J. (1998). A Rapid Fusion Method for Separation of Beryllium-10 From Soils and Silicates. *Geochemica et Cosmochemica Acta, 62*, 551-561.

Stone, J. O. (2000). Air pressure and cosmogenic isotope production. *Journal of Geophysical Research 105*, 23,753-23,759.

Stone, J., Balco, G., Sugden, D., Caffee, M., Sass III, L., Cowdery, S., & Siddoway, C. (2003). Holocene Deglaciation of Marie Byrd Land, West Antarctica. *Science, 299*, 99-102.

Todd, C., Stone, J., Conway, H., Hall, B., & Bromley, G. (2010). Late Quaternary evolution of Reedy Glacier, Antarctica. *Quaternary Science Reviews, 29*, 1328-1341.

Tuniz, N., & Norton, G. (2008). Accelerator mass spectrometry: New trends and applications. *Nuclear Instruments and Methods in Physics Research B, 266*, 1837–1845.

van der Woerd, J., Klinger, Y., Sieh, K. T., Ryerson, F., & Meriaux, A.-S. (2006). Long-term slip rate of the southern San Andreas Fault from ^{10}Be-^{26}Al surface exposure dating of an offset alluvial fan. *Journal of Geophysical Research, 111*, 1-17.

Vieli, A., & Nick, F. (2011). Understanding and Modelling Rapid Dynamic Changes of Tidewater Outlet Glaciers: Issues and Implications. *Surveys in Geophysics, 32*, 437-458.

Webber, W., & Higbie, P. (2003). Production of cosmogenic Be nuclei in the Earth's atmosphere by cosmic rays: Its dependence on solar modulation and the interstellar cosmic ray spectrum. *Journal of Geophysical Research - Space Physics, 108*.

White, D., Fink, D., & Gore, D. (2011). Cosmogenic nuclide evidence for enhanced sensitivity of an East Antarctic ice stream to change during the last deglaciation. *Geology, 39*, 23-26.

Whitehouse, P., Bentley, M., & Le Brocq, A. (2012). A deglacial model for Antarctica: geological constraints and glaciological modelling as a basis for a new model of Antarctic glacial isostatic adjustment. *Quaternary Science Reviews, 32*, 1-24.

Willenbring, J., & von Blanckenburg, F. (2010). Meteoric cosmogenic Beryllium-10 adsorbed to river sediment and soil: Applications for Earth-surface dynamics. *Earth Science Reviews*, 105-122.

Wouters, B., Martin-Espanol, A., Helm, V., Flament, T., van Wessem, J., Ligtenberg, S., van den Broeke, R., Bamber, J. (2015). Dynamic thinning of glaciers on the Southern Antarctic Peninsula. *Science, 348*, 899-903.

Young, N., Schaefer, J., Briner, J., & Goehring, B. (2013). A ^{10}Be production-rate calibration for the Arctic. *Journal of Quaternary Science, 28*, 515-526.

Appendix A

Pyroxene preparation and beryllium separation chemistry

Original method by Blard, *et al.* (2008)

Modified by Julia Collins, Feb 2013

Initial pyroxene separation

Sample crushed and sieved to appropriate size fractions (125-250 µm and 250-500 µm).

Sample washed with RO deionised water.

Heavy liquid separation to extract pyroxene using Methylene Iodide density 3.1.

Inspect under binocular microscope to identify cleanest size fraction of pyroxene.

Run >3.1g/cm^3 chosen size fraction on Frantz magnetic separator to separate non-magnetic grains.

Separation of the strongly magnetic minerals using hand magnet.

Cleaning procedure for pyroxene

Crush pyroxenes in agate ringmill for 90 seconds per sample and sieve to <90 µm.

Re-crush material for another 30-60 seconds depending on amount of >90 µm material and sieve again.

Small amount of remaining material >90 µm collected in separate container and hand crushed using agate mortar and pestle to <90 µm.

Leach 1 in Hydroxylammonium-chloride

Weigh empty 180 ml savillex beaker

Then weigh in ~4 g of each sample into the beaker

Leaching in 20 ml 0.04M $NH_2OH.HCl$ in 25% acetic acid overnight for 10 hr at 95±5℃.

Remove from hotplate and let cool for 15 min.

Transfer sample into 50 ml centrifuge tube using additional 5 ml 0.04M $NH_2OH.HCl$ to wash all sample into centrifuge tube.

Centrifuge for 5 min at 3000 rpm.

Decant liquid into acid waste.

Add 5ml 0.04M $NH_2OH.HCl$ to solid sample left in centrifuge tube and shake to rinse sample

Centrifuge again for 5 min at 3000 rpm.

Repeat above rinsing step 1x more.

After final rinse, transfer solid sample back into original savillex beaker using milliQ water.

Dry solid sample on hotplate.

Weigh sample.

Leach 2 in HCl

Sample washed into 50 ml centrifuge tube using 1M HCl and topped up to 25 ml of 1M HCl. Placed on rollers for 24 hours at 20℃.

Samples centrifuged for 5 min at 3000rpm.

Sample rinsed 3x with milliQ water - being centrifuged between each rinse.

Solid sample washed from centrifuge tube back into original savillex beaker using milliQ.

Solid sample dried on hotplate for ~3 hours, or until dry.

Solid sample weighed.

Dissolution

Wash sample into 50 ml tube using milliQ, then add conc HF to get 4M HF.

Dissolution in 35 ml 4M HF during 24h at 20℃ on rollers.

Add 10 ml of 15M HNO_3, shake and leave for 20min.

Centrifuge samples for 5 min @ 3000 rpm.

Decant supernate into acid waste.

Rinse with milliQ.

Centrifuge for 5 min at 3000 rpm.

Decant supernate into acid waste.

Repeat rise 2x more.

Solid sample washed from centrifuge tube back into original savillex beaker using milliQ.

Solid sample dried on hotplate.

Solid sample weighed.

Carrier addition

Put ^{9}Be carrier on scale and tare.

Pipette 750 µl out and add to sample.

Precisely weigh how much mass removed and record weight – weight more accurate than volume measured in pipette.

Tare scales and repeat for each sample.

Bulk dissolution

Add 20 ml conc HF to each sample, shake and then reflux on hotplate overnight at 120℃.

Remove from hotplate and let cool.

Add 2ml conc HNO_3, swirl and dry down on hotplate.

Once dry add 20 ml conc HF and reflux overnight at 120℃.

Open up to dry down.

Once dry add 5 ml conc HF and dry down again.

H_2O leach

Add 10 ml of MQ to each sample.

Heat for 20 min at 60℃.

Cool for 15 min.

Pipette solution out into 50 ml centrifuge tube leaving solids in beaker.

Repeat above steps 2x more.

Rinse remaining solids into another centrifuge tube using MQ.

Wipe out beakers using kimwipe to remove all solids.

Put solution back into original savillex beakers and dry down on hotplate.

Add 8 ml 6M HCl to each beaker and heat on hotplate at 60℃ for ~2 hours or until dissolved.
Let sample cool completely before moving to 15 ml centrifuge tube.
Centrifuge for 5 min @ 3500 rpm – do not add solids to Fe columns.

Fe columns

2 ml Biorad 1x8 100-200 mesh in 15 ml Eichron Column stored in H_2O.

1. open column and let water drop out
2. 5ml + 5ml 0.3M HCl to clean resin
3. 2ml + 2ml + 2ml 6M HCl to condition resin
4. load sample (for darker samples spread across 2-3 columns) **Collect in beaker**
5. 2ml +2ml + 2ml 6M HCl to remove all sample **Collect in beaker**

NB: If sample comes out still containing iron (i.e. it's still yellow) then repeat steps 2-5

6. 5ml + 5ml 0.3M HCl to clean resin
7. cap column and store in milliQ H_2O

Dry down samples on hotplate.
Add 40 ml 0.4M oxalic acid to each put on hotplate at 60℃ until dissolved.
Transfer samples into 50 ml centrifuge tubes once dissolved.
Centrifuge for 5 min @ 3000 rpm.

25ml Be columns

20ml Biorad AG50-X8 100-200 mesh resin in 25ml Eichrom columns stored in H_2O

1. Open column and let water drip out (drain to waste)
2. Add 20ml + 40ml ~5M HNO_3 to clean resin (drain to waste)
3. Add 20ml + 20ml milliQ H_2O to remove HNO_3 from the resin (drain to waste)
4. Add 20ml + 40ml 0.4M oxalic acid to condition resin (drain to waste)
5. Add sample (in 40 ml 0.4M oxalic acid) (drain to waste)
6. Add 20ml + 20ml 0.4M oxalic to wash sample down (drain to waste)
7. Add 200ml 0.4M oxalic acid to elude Fe, Al, Ti, etc. (drain to waste)

8. Add 20ml + 40ml milliQ H_2O to remove oxalic acid (drain to waste)
9. Add 40ml + 60ml 0.5M HNO_3 to elude Na (drain to waste)
10. Add 20ml 1M HNO_3 wash (collect in 50 ml tube)
11. Add 80ml + 80ml 1M HNO_3 to elude Be **Collect Be in original beaker**
12. Add 160ml 5M HNO_3 to clean resin (drain to waste)
13. Add 20ml + 20ml H_2O to remove HNO_3 (drain to waste)
14. Add milliQ and seal the columns for storage

Dry down samples at 120 °C to evaporate solution.

Be Precipitation

Add 10 ml 1M HNO_3 to each and transfer to 15 ml centrifuge tube.
Add 1 ml of conc ammonia (or more) until it is pH~9.
Shake and hold up to light to see if BeOH precipitated.
Centrifuge for 5 min @ 3500 rpm.

Be precipitate wash

Decant supernate of each sample into new centrifuge tube.
Add 3ml MQ to each BeOH precipitate.
Shake/tap to loosen precipitate and suspend in MQ.
Centrifuge for 5min @ 3500 rpm.
Decant supernate into same centrifuge tube.
Repeat rinse x2.
Leave sample in 3 ml MQ.

Transfer Be to quartz crucible

Decant MQ into waste.
Add 0.3 ml 5M HNO_3 to each sample to dissolve BeOH.
Transfer to quartz crucible in stand.
Put crucibles in stand on hotplate overnight or until dried.
Hold each crucible over Bunsen burner flame until hydroxide and nitrate is boiled off and Be is oxidised.

Measurement of $^{10}Be/^{9}Be$ ratios

Send to ANU to be measured by AMS